

For Reference

NOT TO BE TAKEN FROM THIS ROOM

For Reference

NOT TO BE TAKEN FROM THIS ROOM

Ex libris
UNIVERSITATIS
ALBERTAENSIS



6

Introduction

The purpose of this study is to investigate the effects of the proposed system on the performance of the system. The study is divided into two main parts: a theoretical analysis and an experimental evaluation.

The theoretical analysis is based on the following assumptions:

1. The system is assumed to be in a steady state.

2. The system is assumed to be linear and time-invariant.

3. The system is assumed to be stable.

Methodology

The methodology used in this study is based on the following steps:

1. The system is modeled using a block diagram.

THE UNIVERSITY OF ALBERTA

ELECTRICAL CHARGING AND DETECTION
OF MICROPARTICLES FOR THE SIMULATION
OF MICROMETEORIDS

BY

FREDERICK VERMEULEN

A THESIS

SUBMITTED TO THE FACULTY OF GRADUATE STUDIES
IN PARTIAL FULFILMENT OF THE REQUIREMENTS FOR THE DEGREE
OF DOCTOR OF PHILOSOPHY

DEPARTMENT OF ELECTRICAL ENGINEERING

EDMONTON, ALBERTA

DATE

UNIVERSITY OF ALBERTA
FACULTY OF GRADUATE STUDIES

The undersigned certify that they have read, and recommend to the Faculty of Graduate Studies, a thesis entitled "Electrical Charging and Detection of Microparticles for the Simulation of Micrometeoroids" submitted by Frederick Vermeulen in partial fulfilment of the requirements for the degree of Doctor of Philosophy.

ABSTRACT

Electrical charging and detection of microparticles for the simulation of micrometeoroids is studied. A contact charging process is investigated in detail. It is found that field intensification during the charging process can be minimized and that the transfer of charge can be increased, as the size of the charging sphere decreases and approaches that of the microparticle. A charge sensitive detection technique is used to measure microparticle charge and velocity. An optical detection technique, which employs a 100 watt zirconium concentrated arc lamp and a Philips 150 AVP 02 photomultiplier, has been developed. Particles with radii of 1.5 to 2 microns and velocities of 0.15 Km/sec have been reliably detected. Methods are suggested to extend the usefulness of the optical detection scheme to particle velocities of several Km/sec. The general behaviour of particles with differing charge to mass ratios in electromagnetic fields has been studied, and methods for their acceleration have been suggested.

ACKNOWLEDGEMENTS

The author wishes to express his gratitude to Dr. G.B. Walker, the supervisor of this project, for his invaluable encouragement and guidance throughout the course of this study.

The interest shown and many suggestions made by members of faculty, graduate students and the technical staff of the Electrical Engineering Departments at the University of British Columbia and University of Alberta, are gratefully acknowledged. Particular thanks are due to Dr. C.G. Englefield, Dr. C.R. James and Mr. E. Buck. Thanks are also due to Mrs. S. Walker for typing the manuscript.

The author is indebted to the National Research Council for the award of Studentships during 1963 and 1964, and to the Electrical Engineering Department at the University of Alberta for a Research Assistantship for the remainder of this study.

TABLE OF CONTENTS

	Page
1. INTRODUCTION	1
1.1 The Importance of Interplanetary Particles to the Space Sciences	1
1.2 The Evidence for the Existence of Interplanetary Particles	2
1.2.1 The Solar F-Corona and the Zodiacal Light	2
1.2.2 Meteors	3
1.2.3 Terrestrial Accretion	4
1.2.4 Satellite, Rocket and Space Probe Measurements	4
1.3 The Simulation of Interplanetary Particles . . .	7
1.3.1 The Role of Laboratory Experiments	7
1.3.2 Techniques for Accelerating Projectiles to Hypervelocities	8
1.3.3 The Subjects that are Investigated in this Thesis	12
2. THE ELECTRICAL CHARGING OF MICROPARTICLES	14
2.1 Theoretical Considerations	14
2.1.1 A Mathematical Model for the Charging Process	14
2.1.2 The Transfer of Charge from the Charging Electrode to the Microparticle	15
2.1.3 Field Intensification during the Charging Process	22
2.1.4 Electrical Breakdown	30

2.2	Experimental Work	33
2.2.1	High Vacuum Apparatus	33
2.2.2	Particle Charging Mechanism	33
2.2.3	Observations and Experiments	37
	A. Particle Emission	37
	B. Breakdown Phenomena	43
	C. Charge to Mass Ratios	45
	D. Cratering Phenomena	50
2.2.4	The Manufacture of Charging Electrodes . .	54
3.	DETECTION OF MICROPARTICLES	57
3.1	Charge Detection	57
3.2	Optical Detection	70
3.2.1	Theoretical Considerations	70
3.2.1.1	Scattering by Small Particles	71
3.2.1.2	Radiation Pressure upon Small Particles	80
3.2.2	Experimental Work	83
3.2.2.1	Description of Experimental Equipment	83
3.2.2.2	An Estimate of the Photomultiplier Signal	92
3.2.2.3	Experimental Results	96
3.2.2.4	Threshold Sensitivity of the Optical Detection System	103
4.	CONSIDERATIONS WITH REGARD TO THE ACCELERATION OF MICROPARTICLES	107
4.1	The Relationship between Accelerating Voltage and Particle Velocity	107
4.2	The Relative Magnitudes of Electric and Magnetic Forces	110
4.3	Some Useful Properties of the Electrostatic Field	111

4.4	Particle Motion in a Time Varying Field	113
4.5	A Brief Proposal for Accelerating Particles with Differing Charge to Mass Ratios	118
5.	THE DETECTION OF UNCHARGED PARTICLES	126
6.	CONCLUSION	131
	APPENDIX	133
	BIBLIOGRAPHY AND REFERENCES	136

LIST OF ILLUSTRATIONS

Figure	Page
2.1 Two Conducting Spheres	17
2.2 F_a/F_b versus a/b	17
2.3 Diagram Relevant to Computation of F_{max}	24
2.4 F_{max}/F_b versus a/b	24
2.5 F_a/F_{ult} versus a/b	29
2.6 High Vacuum System	34
2.7 Particle Charging Mechanism	35
2.8 Exploded Views of the Charging Mechanism	38
2.9 Charging Mechanism and Associated Experimental Equipment	39
2.10 Charge to Mass Ratio versus Radius for Carbonyl Iron Microparticles	47
2.11 Charge to Mass Ratio versus Radius for Carbonyl Iron Microparticles	48
2.12 Cratering Phenomena (Approx. 750x)	51
2.13 Cratering Phenomena (Approx. 750x)	51
2.14 Cratering Phenomena (Approx. 750x)	52
2.15 Photomicrograph of a Charging Sphere with a Radius of 62 microns	52
2.16 Mechanism for Forming Charging Spheres. Shown is the Needle Adjustment Mechanism, a Discharge and the Observation Microscope	56
3.1 Drift Tube Particle Detector and Detector Charge versus Time	58
3.2 Collection Plate Particle Detector and Detector Charge versus Time	59
3.3 Charge Sensitive Amplifier	61
3.4 Charge Sensitive Amplifier, Particle Detector and Calibrating Circuit	61

3.5	Sketch of Detector Combination and Amplifier Output . .	64
3.6	Photograph of Oscilloscope Trace of Particle that has been Intercepted by Screen of 4 th Detector	68
3.7	Photograph of Oscilloscope Trace of Particle that has Traversed all Detectors	68
3.8	Photograph of Particle Detectors, Alignment Rods and Charging Mechanism	69
3.9	Diagram for the Definition of the Scattering Angle . . .	72
3.10	Scattering Diagrams for Totally Reflecting Spheres . . .	76
3.11	Definition of τ and τ'	79
3.12	Absolute Values of the Reflection Coefficients for $m = 1.27 - j1.37$	79
3.13	Diagram of the Essential Components of the Optical Detection Scheme (View 1).	84
3.14	Diagram of the Essential Components of the Optical Detection Scheme (View 2).	86
3.15	Schematic Diagram of Photomultiplier and Output Circuit.	89
3.16	A.C. Equivalent Circuit	91
3.17	Sketch of Output from Photomultiplier (Top Trace), and Charge Sensitive Amplifier (Bottom Trace).	91
3.18	Experimental System for Optical Detection of Micro- particles Upper Photograph: Front View Lower Photograph: Top View	93
3.19	Experimental System for Optical Detection of Micro- particles (Rear View)	94
3.20, 3.21	Photomultiplier and Charge Sensitive Detector Signals	97
3.22, 3.23	Photomultiplier and Charge Sensitive Detector Signals	98
3.24	Comparison of Experimental and Estimated Photomultiplier Signals	99
3.25	A.C. Equivalent Circuit for Measuring Photomultiplier Anode Current due to Mean Background Light Intensity . .	102

3.26	The Effects of Dark Current and of Fluctuations in the Level of the Background Light Intensity	104
4.1	Relationship Between Accelerating Voltage, Particle Radius and Particle Velocity for Iron Spheres with a Surface Field Intensity of $2 \cdot 10^9$ Volts/Meter	109
4.2	A Sequence of Drift Tubes and Accelerating Gaps . . .	119
4.3	Sketch of Microparticle Accelerator Proposal	122
5.1	Anomalous Photomultiplier Signal	129
5.2	Blocking of Particle Aperture by Small Plastic Sheet .	129
5.3	Charge Sensitive Detector Response to Induced Polarization on Small Plastic Sheet	129
A.1	High Voltage Pulsing Circuit	134
A.2	Charge Sensitive Amplifier	135

1. INTRODUCTION

This investigation deals with the development of techniques that are necessary for the acceleration of micron sized particles to hyper-velocities. These are essential to the simulation of the environment to which man-made vehicles are exposed in outer space. This chapter contains a brief review of the present knowledge of particles in outer space, of how this knowledge is obtained, and of the efforts which have been made to simulate these particles.

1.1 The Importance of Interplanetary Particles to the Space Sciences

The prospect of prolonged travel in outer space has led to an intensive study of the external environment to which spacecraft and their inhabitants will be exposed while on their missions in space. Particular attention has been given to the study of the solid particles which travel in interplanetary space and have larger than atomic and molecular dimensions.

These particles pose a hazard to space travel because of the extensive damage which they may inflict to spacecraft upon collision. The bombardment by high velocity particles may cause puncture of pressurized cabins, fuel tanks and spacesuits, or failure of heat shields during atmospheric re-entry because of deep pitting. Absorption of the kinetic energy of an impinging particle may lead to local vapourization of interior surfaces, and oxidation of this vapour by the space vehicle atmosphere could result in explosions. Solar panels, viewing ports, optical lenses and heat exchangers may be eroded with a resultant decrease in their efficiency^{(1),(2)}.

Besides being of interest to designers of space craft, particles in interplanetary space have long been studied by astronomers and astrophysicists. Their most fundamental question pertains to the source of interplanetary particles. It has been hypothesized that the major sources are ejected material from comets and the products of the grinding and fragmentation of the asteroids^{(3),(4),(5)}. Other possible sources are ejected material from the surface of the moon⁽⁶⁾, interstellar capture⁽⁷⁾ and condensation of interplanetary gas⁽⁸⁾.

1.2 The Evidence for the Existence of Interplanetary Particles

1.2.1 The Solar F-Corona and the Zodiacal Light

Various phenomena support the existence of particles in interplanetary space. The solar F-corona, also referred to as the inner zodiacal light, is attributed to sunlight which has been diffracted by dust particles that are located between the earth and the sun. On the basis of photometric observations, the diameter of these particles has been calculated to range from 0.2 microns to 300 microns^{(9),(10),(11),(12)}.

A related phenomenon, the zodiacal light^{(13),(14),(15)}, is a continuation of the solar F-corona in the plane of the ecliptic. The zodiacal light extends to a region opposite the sun, where a slight enhancement, or "gegenschein"⁽¹⁶⁾, occurs. The location of the zodiacal light in the plane of the ecliptic suggests that the latter is a region of concentration of dust particles.

1.2.2 Meteors

On its journey around the sun, the earth continually encounters innumerable small, solid particles. These meteoroids approach the earth at velocities of 11 Km/sec to 72 Km/sec, and, upon interaction with the earth's atmosphere, dissipate their kinetic energy in the form of heat, light and ionization. The phenomena thus produced are called meteors. It is of interest to note that 11 Km/sec is the velocity which particles would attain if they started from rest at a great distance from the earth and fell towards it under the influence of its gravitational field. 72 Km/sec is the maximum possible velocity of collision between the earth and particles in retrograde orbit around the sun⁽¹⁷⁾.

Meteors have been studied extensively with photoelectric and photographic devices, through visual observation, and with sensitive television cameras, image intensifiers and radar. The sensitivity of the methods of observation increases in the order in which they are listed. The smallest meteors which are detected are produced by meteoroids with masses of the order of 10^{-6} gms^{(18), (19)}.

A meteoroid is usually completely transformed into dust and vapour during its passage through the atmosphere. Occasionally, a portion or fragment survives and lands on the earth as a meteorite. Particles with a diameter of less than a few microns radiate energy so rapidly upon being retarded by the atmosphere that their temperature remains below their melting point and they drift to earth without undergoing physical changes⁽²⁰⁾.

1.2.3 Terrestrial Accretion

Particles of extraterrestrial origin ranging in size from 3 microns to 850 microns⁽²¹⁾ have been recovered from the atmosphere⁽²²⁾, from polar ice deposits^{(23),(24)}, from deep sea sediments^{(25),(26),(27)}, and from geological sediments⁽²⁸⁾. These particles are distinguished from terrestrial and industrial dust by their chemical composition⁽²⁹⁾, which usually includes iron, nickel and silicon, by their predominantly magnetic nature, by their usually spherular shape and by the remote location and the very old age of the sediments from which they have been recovered.

1.2.4 Satellite, Rocket and Space Probe Measurements

The most recent and most direct evidence for the existence of very small particles in the earth's upper atmosphere and in space has been obtained by the use of rockets, satellites and space probes. The particles which have been sensed have masses between approximately 10^{-7} gms and 10^{-13} gms and are designated as micrometeoroids. Several types of micrometeoroid detectors are carried. They include:

1. Acoustic systems. These consist of a sensing area and an attached piezoelectric transducer which detects the pressure waves that originate at the point of particle impact. They are used more often than any of the other detectors^{(30),(31)}.

2. Systems employing photomultipliers that are located at the apex of a lucite cone. The surface of the cone is completely aluminized except for an exit window at the apex. When a particle strikes the base of the cone, the aluminum coating is penetrated and a flash of

visible light is produced. This light is captured within the cone and reflected into the photomultiplier⁽³²⁾.

3. Cadmium sulphide cells which are shielded from sunlight by a very thin opaque cover. If the cover is punctured by a particle, sunlight enters and activates the cadmium sulphide cell behind it⁽³³⁾.

4. Pressurized, extremely thin walled beryllium copper and stainless steel semi-cylinders. These systems are sensitive to the pressure drop in the cylinder after it has been punctured⁽³⁴⁾.

5. Very thin stainless steel plates backed with fine gold wire, and cards wound with thin enamelled copper wire. Either device indicates the loss of electrical continuity when an impinging particle penetrates the stainless steel plate and breaks the gold wire, or when a particle breaks the copper wire⁽³⁵⁾.

6. Capacitor discharge type detectors. These detectors incorporate a sheet of metal whose penetrations are to be sensed and counted. The metal is backed by a sheet of very thin dielectric, which in turn is covered with an electrically conducting metallic vapour deposit. The capacitor thus formed is electrically charged by applying a potential difference between the sheet of metal and the metallic vapour deposit. Penetration of this detector by a particle provides a temporary conduction path through which the capacitor can discharge, thereby generating a voltage pulse which may be monitored.

Capacitor discharge type detectors with a total sensing area of 200 meter² were carried by the recent series of Pegasus satellites⁽³⁶⁾.

7. Particle collecting surfaces. These surfaces have been used by the Venus Flytrap rocket probe⁽³⁷⁾ and by other probes which have

sampled the noctilucent clouds⁽³⁸⁾. The surfaces have trapped and brought back to earth submicron sized particles.

It should be noted that particle detectors can provide an approximate measure of particle momentum or energy, but do not measure the particle velocity. Therefore, they give no direct indication of particle mass. The computation of an approximate particle mass is made possible by ascribing an average particle velocity to the detector data^{(39),(40)}.

The data collected from numerous rockets, satellites and space probes, which carried piezoelectric transducers and light flash detection systems, indicates that the micrometeoroid flux in space increases with decreasing particle mass. The measured average cumulative flux rate near the earth ranges from approximately

$$\begin{array}{l} 10^{-5} \text{ particles/meter}^2\text{sec for particles with masses } \geq 10^{-7} \text{ gms} \\ \text{to} \\ 3 \times 10^2 \text{ particles/meter}^2\text{sec for particles with masses } \geq 10^{-13} \text{ gms} \end{array} \quad (41).$$

Estimates based on American and Russian satellite flux measurements place the daily deposit of these particles on earth at 10^4 tons⁽⁴²⁾.

The micrometeoroid distribution to an altitude of about 200 Km has also been investigated in a series of Canadian rocket experiments⁽⁴³⁾. Impact detecting surfaces with attached piezoelectric transducers were carried and measured an average flux rate of approximately

$$1.4 \text{ particles/meter}^2\text{sec for particles with masses } \geq 10^{-11} \text{ gms.}$$

The distribution of dust particles at very large distances from the earth, as deduced from photometric studies of the zodiacal light and the solar F-corona, is generally expressed in terms of particle radius and spatial density of particles of a given radius.

The results of the direct rocket and satellite measurements near the earth are expressed in terms of particle mass and particle flux rates. Conversion from particle radii to masses and from spatial densities to flux rates requires that the particle mass densities and velocities be known. The densities may range from less than 1 gm/cc for extremely porous particles to about 7 gms/cc for dense metallic particles. In view of this wide range of possible values, comparison of the two types of dust particle data is difficult. However, it has been suggested⁽⁴⁴⁾ that the spatial density of dust particles near the earth is about 3 orders of magnitude greater than in interplanetary space. This view is supported by space probe measurements at very large distances from the earth⁽⁴⁵⁾.

1.3 The Simulation of Interplanetary Particles

1.3.1 The Role of Laboratory Experiments

At present, accurate knowledge in the field of hypervelocity impact is completely absent in the high and medium meteoroid velocity ranges and sparse in the lower meteoroid velocity range. The interpretation of the data that is received from particle detectors flown in space is based on the extrapolation of results that have been obtained from impact experiments at low or sub meteoroid velocities⁽⁴⁶⁾. The interpretation can be in error because the character of hypervelocity impacts, besides being highly dependent on the projectile and target materials and their construction, is marked by phenomena which are peculiar to particular velocity ranges. These phenomena are difficult or impossible to predict without appropriate laboratory

experiments.

Some satellite experiments, such as those employing capacitor discharge type detectors, are designed to measure the resistance of different materials to particle penetration directly. These experiments, although signalling penetration of the given structural material, do not provide further information about the exact extent of the damage or about the residual destructive capability of the projectile. Consequently, the space experiments are not as well suited for the development of protective structures to withstand meteoroid bombardment, as are controlled laboratory experiments.

1.3.2 Techniques for Accelerating Projectiles to Hypervelocities

The most widely used laboratory devices for hypervelocity research on meteoroid damage are guns that use the energy of an explosive charge to accelerate the projectile. Guns have a velocity limitation because the projectile cannot travel faster than the shockwave created by the explosion. Since the shockwave velocity in light gases, such as hydrogen or helium, is higher than in the gases created by the explosion, one of the former light gases is often introduced between the explosive and the projectile. Light gas guns of this type have accelerated projectiles with diameters of several millimeters to velocities of approximately 10 Km/sec^{(47), (48)}.

Other methods of producing hypervelocity particles based on an explosion principle (e.g. the micro particle spray produced when a projectile strikes a target) have been used but will not be discussed here.

A promising method for the acceleration of particles that are suited for the simulation of micrometeoroids, consists of electrically charging micron sized particles and introducing them into a strong electric field. This method is closely related to the subject of this thesis.

The velocity which a particle can acquire while moving in an electric field, is a function of the ratio of the charge on its surface to its mass, and of the potential through which it travels. The charge density which can be established on the surface of a given particle is limited to a theoretical maximum value; if this value is exceeded, electrical breakdown occurs. If particles that differ in size but are otherwise similar, are charged to the same surface charge density, then the smaller particles, having a larger surface area per unit of mass than the larger ones, will have a higher charge to mass ratio. In view of this, the velocity to which a particle can be accelerated generally increases with decreasing particle size.

The most reliable presently known charging technique charges particles by impact on an electrode that has a very high electric field intensity at its surface^{(49), (50)}. Upon making contact, all particles, independent of size, acquire a nearly equal surface charge density which is determined by the fields and geometry of the charging electrodes, and, due to inherent and practical limitations, is approximately one order of magnitude less than the theoretical maximum. Since presently available samples of microparticles exhibit a large variation in size, they will exhibit an equally large variation in charge to mass ratio if charged by the foregoing method.

An alternate charging technique consists of electrodynamically

confining a particle to a region in space and bombarding it with an ion beam⁽⁵¹⁾. This method is capable of producing particles with a charge to mass ratio that is very near the theoretical maximum. Unfortunately, the method is complicated and may require a period of several hours to charge a single particle. For these reasons it is not used in the work described in this thesis.

If the field that accelerates the particles is electrostatic, the potential through which the particles can travel is limited by the maximum voltage that can be established by an electrostatic generator. This limitation may be removed by applying the principle of the linac. The particle is accelerated by a succession of drift tubes connected to an oscillatory voltage source. This device is selective in that synchronism can only occur for a particular charge to mass ratio. Since the charge to mass ratio of a particle is not known in advance, the phase and frequency must be changed by some form of signal that is generated by the particle itself as it passes through a system of detectors prior to entering the time varying field of the linac.

Up to the present, particles in flight have been analysed as they pass through a series of detectors which are sensitive to the charge that is carried by the particles. In this way the charge on the particle, the instant in time at which it passes a given point in space, its velocity, and its position in a direction perpendicular to its line of motion can be determined.

This method of detecting the particle's parameters is adequate if the change in velocity of the particle in the linac is not great. For example, if the particle is injected into the linac after falling through a very high DC voltage, synchronism may be obtained more easily

than if the particle is injected at low velocity. In future accelerators, designed for higher velocities, it may be desirable to detect the particle at a number of positions in its flight in order to correct for errors in phase synchronism. This introduces difficulties because the detectors, which are sensitive to the charge induced on them by passing particles, are also sensitive to the charge that is induced on them by the accelerating electric fields. The detectors can be screened from unwanted fields, but if a large number of detectors are used the many separate screens that are required will constitute a physical obstacle in the path of the particles and intercept a large fraction of them. Further, since each detector has an appreciable length, the sum of the lengths of all the detectors will add significantly to that of the accelerator. This requires more exact focussing of individual particles and increases the overall cost of the accelerator, particularly that of the high vacuum system in which it must be enclosed.

In concluding this section it may be relevant to note that of the few microparticle accelerators which are presently in operation, none has succeeded in accelerating particles with diameters greater than one micron to velocities that are significantly larger than those of the slowest micrometeoroids. Smaller particles, with diameters of 0.1 microns have been accelerated to about 30 Km/sec⁽⁵²⁾. These particles were charged by contact and were accelerated in a modified 2 million volt Van de Graaff positive ion accelerator.

More recently, a maximum velocity of 10.8 Km/sec was reported for micron sized particles that were accelerated by a sequential method⁽⁵³⁾. The particles were charged by contact and were

pre-accelerated by a 0.5 million volt Van de Graaff generator. They then entered the sequential accelerator which operates at a fixed phase and frequency. The accelerator selects those particles that have the correct charge to mass ratio for acceleration and rejects the remainder.

1.3.3 The Subjects that are Investigated in this Thesis

It is evident from the preceding discussions that the performance of a microparticle accelerator is very dependent upon the efficiency of the particle charging technique and the methods which are used to detect the particles in flight. In view of this, the present study, which is intended to lay the groundwork for a large microparticle accelerator, is focussed on these two subjects. Evidently, the degree of perfection of a large number of other techniques affects the accelerator performance as well, but many of these have been well known for a long time and can be directly adapted from similar techniques used in atomic particle accelerators.

The work of this thesis is described in the chapters which follow. They deal in turn with:

1. The construction and operation of a system that charges microparticles by contact, and considerations which may increase the contact charging efficiency.
2. The development and operation of a system that analyzes particles in flight by the charge which they carry. The system is more versatile than others that have been reported.
3. The development and operation of a unique optical particle detection scheme.

The optical detection scheme has none of the disadvantages that render the charge detecting scheme unsuitable for repeated use in a very long accelerator. In principle, it can perform all the functions of the charge detection scheme, with the exception that it cannot measure the particle's charge. On the other hand, since it can measure the parameters of a particle that has been stripped of its charge it may be indispensable in a certain class of experiments.

The optical detection technique can be of value in satellite experiments by measuring the velocities of micrometeoroids prior to their collisions with an impact sensitive detector. This would permit the correlation of two independent measurements, and, in addition to the velocities and masses of the micrometeoroids, could provide some knowledge about their mass densities or surface reflectivities.

4. A brief discussion of the behaviour of particles with variable charge to mass ratios in electromagnetic fields with a view towards their acceleration.

2. THE ELECTRICAL CHARGING OF MICROPARTICLES

2.1 Theoretical Considerations

2.1.1 A Mathematical Model for the Charging Process

The actual operation of the contact charging mechanism that has been constructed will be described in a later section. As a basis for the theoretical treatment of this section it is sufficient to state that microparticles are charged by striking a spherical electrode that is supported by a thin shaft and held at a very high potential. Subsequently, having acquired charge of the same sign as that of the electrode, the microparticles are repelled and leave the charging mechanism through an aperture at ground potential.

A model of the charging mechanism that is suitable for mathematical analysis consists of two conducting spheres that are in contact, held at some given potential and surrounded by free space. The problem that must then be solved consists of finding the charge that has been transferred to and is subsequently carried away by the sphere which represents the microparticle. A second problem consists of computing the surface field intensities which occur during contact of the two spheres and, due to breakdown considerations, ultimately limit the efficiency of the charging process.

It must be realized that the foregoing model is not an exact representation of the actual charging process. The shaft that supports the charging electrode and the proximity of interior surfaces of the charging chamber are not accounted for in the idealized model and modify the electric fields that would exist if these were not present. Further,

the surfaces of the electrode and of the microparticle may be non-spherical and either of them may be deformed during the charging process. . Lastly, the model that is analyzed is a static model, whereas the actual charging process is dynamic. For instance, it will be assumed that the microparticle and charging sphere make contact for a sufficient length of time so that all oscillation of charge between them has ceased and electrostatic equilibrium has been established. If this is not the case, i.e., the duration of contact is small compared to the time constant of the charging process, then the microparticle could leave the charging sphere at an instant at which it has either more or less charge than it would have if equilibrium had been reached.

2.1.2 The Transfer of Charge from the Charging Electrode to the Microparticle

The charge on a conductor in terms of its own potential and the potentials of neighbouring conductors can be expressed as⁽⁵⁴⁾

$$q_i = \sum_j c_{ij} V_j \quad \dots(2.1)$$

where

q_i = charge on the i^{th} conductor

V_j = voltage on the j^{th} conductor

c_{ii} = coefficient of capacitance

c_{ij} = coefficient of inductance ($i \neq j$)

Of interest to the present study is the system of two conducting spheres shown in Fig. 2.1. Using the method of image charges one can derive the coefficients c for this system. They are⁽⁵⁵⁾

$$c_{11} = 4\pi\epsilon_0 ab \sinh \alpha \sum_{n=1}^{\infty} (b \sinh n\alpha + a \sinh(n-1)\alpha)^{-1} \quad \dots(2.2)$$

$$c_{12} = c_{21} = -\frac{4\pi\epsilon_0 ab}{c} \sinh \alpha \sum_{n=1}^{\infty} \operatorname{csch} n\alpha \quad \dots(2.3)$$

$$c_{22} = 4\pi\epsilon_0 ab \sinh \alpha \sum_{n=1}^{\infty} (a \sinh n\alpha + b \sinh(n-1)\alpha)^{-1} \quad \dots(2.4)$$

where

$$\alpha = \cosh^{-1} \left(\frac{c^2 - b^2 - a^2}{2ab} \right)$$

and $\epsilon_0 = \frac{10^{-9}}{36\pi}$ farads/meter, the permittivity of free space.

We will now make use of the coefficients c to find q_a , the total charge that is transferred to sphere a , which represents the microparticle, while it is in contact with sphere b , which represents the charging electrode. It will be assumed that throughout the charging process both spheres are at potential V_b . Further

$$c = a + b$$

$$\text{i.e.} \quad \alpha = 0.$$

From equations (2.1), (2.2), (2.3) and from the above we obtain

$$q_a = \lim_{\alpha \rightarrow 0} \left\{ 4\pi\epsilon_0 ab \sum_{n=1}^{\infty} \left(\frac{\sinh \alpha}{b \sinh n\alpha + a \sinh(n-1)\alpha} - \frac{\sinh \alpha}{(a+b) \sinh n\alpha} \right) \right\} V_b \quad \dots(2.5)$$

By making use of the expression

$$\sinh \theta = \theta + \frac{\theta^3}{3!} + \dots$$

and by rearranging terms, equation (2.5) can be rewritten as

$$q_a = 4\pi\epsilon_0 \frac{a^2 b}{(a+b)^2} V_b \sum_{n=1}^{\infty} \left(\frac{1}{n^2} \right) \left(1 - \frac{a}{n(a+b)} \right)^{-1}$$

Conductor 1
or sphere a

Conductor 2
or sphere b

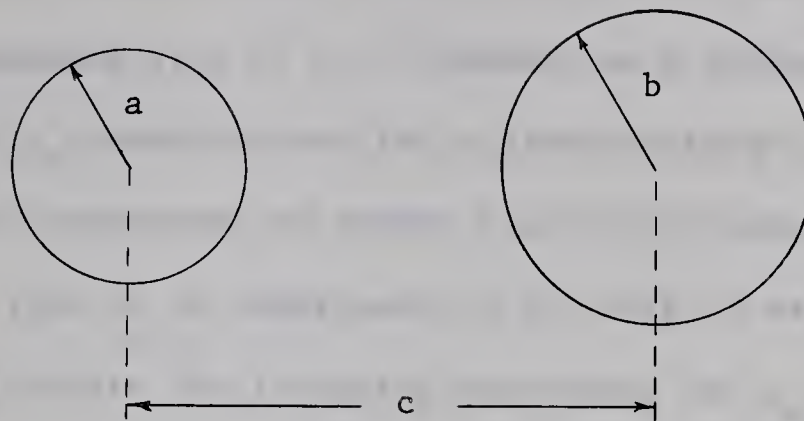


Fig. 2.1 Two Conducting Spheres

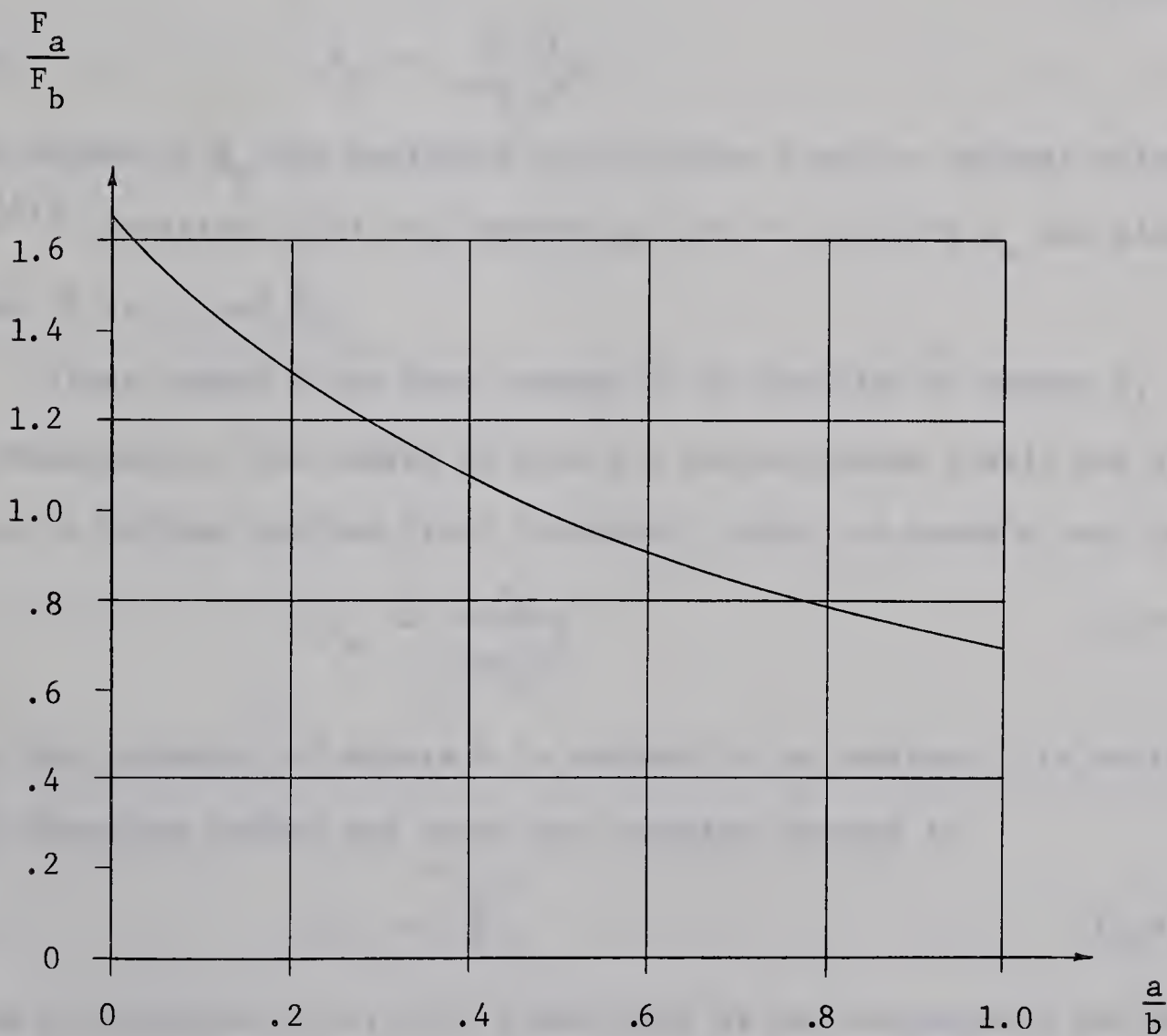


Fig. 2.2 F_a/F_b versus a/b

An expression for q_a similar to the above, but not containing the last factor under the summation sign, has been used by other workers⁽⁵⁶⁾. The disagreement between their expression and the above expression is of small consequence if $a \ll b$. However, as a approaches b , our expression for q_a predicts that for a given voltage V_b nearly twice as much charge is transferred to sphere a as is predicted by the other expression. This is of importance to the work of section 2.1.3.

We can rewrite the foregoing expression for q_a in more compact form, i.e.,

$$q_a = 4\pi\epsilon_0 b V_b \sum_{n=1}^{\infty} \left(\frac{1}{n^2} \left(\frac{a}{a+b} \right)^2 + \frac{1}{n^3} \left(\frac{a}{a+b} \right)^3 + \dots \right) = 4\pi\epsilon_0 b V_b \sum_{m=2}^{\infty} \left(\xi_m \left(\frac{a}{a+b} \right)^m \right) \dots (2.6)$$

where
$$\xi_m = \sum_{n=1}^{\infty} \left(\frac{1}{n^m} \right) .$$

Since values of ξ_m are available in tabulated form for integer values of m ⁽⁵⁷⁾, equation (2.6) can readily be used to evaluate q_a for given values of a , b , and V_b .

After sphere a has been charged it is repelled by sphere b , and, subsequently, the charge on sphere a redistributes itself and gives rise to a uniform surface field intensity, which, by Gauss's Law, is

$$F_a = \frac{q_a}{4\pi\epsilon_0 a^2} \dots (2.7)$$

Since the potential of sphere b is assumed to be constant, its surface field intensity before and after the charging process is

$$F_b = \frac{V_b}{b} \dots (2.8)$$

By use of equations (2.6), (2.7) and (2.8) we can now express the surface field intensity that has been established on sphere a (the micro-particle) in terms of the field intensity on sphere b (the charging

electrode), i.e.,

$$F_a = \left(\frac{b}{a}\right)^2 F_b \sum_{m=2}^{\infty} \left(\xi_m \left(\frac{a}{a+b}\right)^m\right) \quad \dots(2.9)$$

We can express F_a in closed form for two cases. The first case is of particular interest because it most closely corresponds to the situation that is present during the actual charging process.

Case 1: $\lim \frac{a}{b} \rightarrow 0$

$$F_a = F_b \xi_2 \quad \dots(2.10)$$

or, since $\xi_2 = \frac{\pi^2}{6}$ (58)

$$F_a = F_b \frac{\pi^2}{6}$$

Consequently, from the above and from equation (2.7), the charge that is transferred to the microparticle is

$$q_a = \left(\frac{\pi^2}{6} \epsilon_o F_b\right) (4\pi a^2)$$

Since the particle's mass is

$$m_a = \frac{4}{3} \pi a^3 \rho$$

where ρ = mass density,

the particle's charge to mass ratio is

$$\left(\frac{q}{m}\right)_a = \frac{\pi^2 \epsilon_o}{2\rho} \frac{F_b}{a} \quad \dots(2.11)$$

Thus, the charge to mass ratio of a particle that has been charged by contact, and whose radius is negligibly small compared to that of the charging sphere, varies inversely as the particle's radius. This functional dependence is responsible for the spread in charge to mass ratios of contact charged particles of different radii. This, in turn, as mentioned in the introduction, leads to the difficulties that are

encountered when it is attempted to apply the principle of the linac to the acceleration of microparticles.

In concluding the discussion of Case 1, we will establish first order approximations for F_a and $(q/m)_a$ which will indicate to what extent these quantities depart from those predicted by equations (2.10) and (2.11) when $a/b \neq 0$, but $a \ll b$. Let us rewrite equation (2.9) as

$$\begin{aligned} F_a &= F_b \left(\xi_2 \frac{b^2}{(a+b)^2} + \xi_3 \frac{ab^2}{(a+b)^3} + \xi_4 \frac{a^2 b^2}{(a+b)^4} + \dots \right) \\ &= F_b \left(\xi_2 \left(1 + \frac{a}{b}\right)^{-2} + \xi_3 \left(\frac{a}{b}\right) \left(1 + \frac{a}{b}\right)^{-3} + \xi_4 \left(\frac{a}{b}\right)^2 \left(1 + \frac{a}{b}\right)^{-4} + \dots \right) \end{aligned}$$

Upon differentiating the above with respect to a/b and evaluating the resulting expression at $a/b = 0$, we obtain

$$\left. \frac{dF_a}{d\left(\frac{a}{b}\right)} \right|_{\left(\frac{a}{b}\right)=0} = F_b (-2\xi_2 + \xi_3)$$

Use of the foregoing result and of equation (2.10) yields

$$\begin{aligned} \left. \frac{dF_a}{F_a} \right|_{\left(\frac{a}{b}\right)=0} &= \frac{-2\xi_2 + \xi_3}{\xi_2} d\left(\frac{a}{b}\right) \\ &= -1.27 d\left(\frac{a}{b}\right) \end{aligned}$$

$$\text{Or, } F_a = \left\{ F_a \right\}_{\left(\frac{a}{b}\right)=0} \left(1 - 1.27 d\left(\frac{a}{b}\right) \right)$$

Thus, for $a \ll b$

$$F_a = F_b \frac{\pi^2}{6} \left(1 - 1.27 \left(\frac{a}{b}\right) \right) \dots (2.12)$$

Also, since by virtue of equation (2.7), q_a varies directly as F_a , we

obtain from the above and from equation (2.11), that, for $a \ll b$,

$$\left(\frac{q}{m}\right)_a = \frac{\pi^2 \epsilon_0}{2\rho} \frac{F_b}{a} \left(1 - 1.27 \left(\frac{a}{b}\right)\right) \dots (2.13)$$

Case 2: $a = b$

In this case

$$\begin{aligned} F_a &= F_b \sum_{m=2}^{\infty} \left(\frac{1}{2}\right)^m \\ &= F_b \sum_{n=1}^{\infty} \left(\frac{1}{2n}\right)^2 \left(1 + \frac{1}{2n} + \left(\frac{1}{2n}\right)^2 + \dots\right) \\ &= F_b \sum_{n=1}^{\infty} \left(\frac{1}{2n}\right)^2 \left(1 - \frac{1}{2n}\right)^{-1} \\ &= F_b \sum_{n=1}^{\infty} \left(\frac{1}{2n-1} - \frac{1}{2n}\right) \\ &= F_b \left(1 - \frac{1}{2} + \frac{1}{3} - \frac{1}{4} + \dots\right) \end{aligned}$$

or, since

$$1 - \frac{1}{2} + \frac{1}{3} - \frac{1}{4} + \dots = \ln 2 \quad (59)$$

$$F_a = F_b \ln 2 .$$

A graph, Fig. 2.2, has been constructed to show the variation of F_a/F_b as a function of a/b . It is apparent that the contact charging process becomes less efficient as the size of the micro-particle increases. However, the above analysis does not take into account a local field intensification which occurs while sphere a and sphere b are in contact and which ultimately, due to breakdown considerations, limits the amount of charge that can be transferred to sphere a. The work of section 2.1.3, which is an analysis based on the idealized model of Fig. 2.1, shows that field intensification is most severe when $a \ll b$, and that, in view of this, the charging process

can actually be made more effective as the size of the microparticle increases relative to the size of the charging sphere.

2.1.3 Field Intensification during the Charging Process

While in contact with the charging sphere, the microparticle constitutes a protuberance on the latter's otherwise smooth and relatively flat surface. It is reasonable to assume, therefore, that during the charging process, the maximum field intensification occurs on that part of the microparticle's surface that is farthest removed from the charging sphere. The problem to be solved, therefore, consists of finding the field intensity designated as F_{\max} on Fig. 2.3.

One begins by computing $F_{\max 1}$, which is the contribution to F_{\max} due to all the image charges on spheres a and b while sphere a is at potential V_b and sphere b is grounded. One then computes $F_{\max 2}$, the contribution to F_{\max} due to all the image charges while sphere a is grounded and sphere b is at potential V_b . $F_{\max 1}$ and $F_{\max 2}$ are then added to yield F_{\max} .

For the first part of the problem each one of the image charges, q_n , on sphere a, is one term in the infinite series on the R.H.S. of the appropriate form of equation (2.1), i.e.,

$$q_n = n^{\text{th}} \text{ term of } c_{11} V_b \quad \dots(2.14)$$

Each one of the image charges, p_n , on sphere b is

$$p_n = n^{\text{th}} \text{ term of } c_{21} V_b \quad \dots(2.15)$$

The relative positions of the image charges q_n and p_n are s_n and r_n respectively, as indicated on Fig. 2.3. Smythe⁽⁶⁰⁾ has arrived at

expressions involving s_n and r_n , which, when appropriately rearranged, yield

$$s_n = a + b \left(1 + \frac{q_n}{p_n}\right) \quad \dots(2.16)$$

and

$$r_n = -b \frac{p_n}{q_n} \quad \dots(2.17)$$

With reference to Fig. 2.3 we now write

$$F_{\max 1} = \sum_{n=1}^{\infty} \frac{q_n}{4\pi\epsilon_0 (s_n + a)^2} + \frac{p_n}{4\pi\epsilon_0 (2a + b - r_n)^2}$$

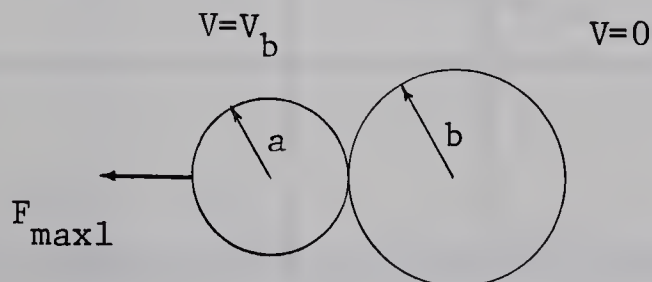
which, by use of equation (2.16) and (2.17) becomes

$$F_{\max 1} = \sum_{n=1}^{\infty} \frac{q_n}{4\pi\epsilon_0 \left(2a + b \left(1 + \frac{q_n}{p_n}\right)\right)^2} + \frac{p_n}{4\pi\epsilon_0 \left(2a + b \left(1 + \frac{p_n}{q_n}\right)\right)^2}$$

Finally, by use of equations (2.14), (2.15), (2.2), (2.3), and, upon taking the limit as $\alpha \rightarrow 0$, the above equation yields

$$F_{\max 1} = V_b \sum_{n=1}^{\infty} \frac{ab(bn + a(n-1))}{(2a^2(n-1) + ab(2n-1))^2} - \frac{ab(n(a+b))}{(2a^2n + ab(2n+1))^2} \quad \dots(2.18)$$

The foregoing solution applies to the following configuration.



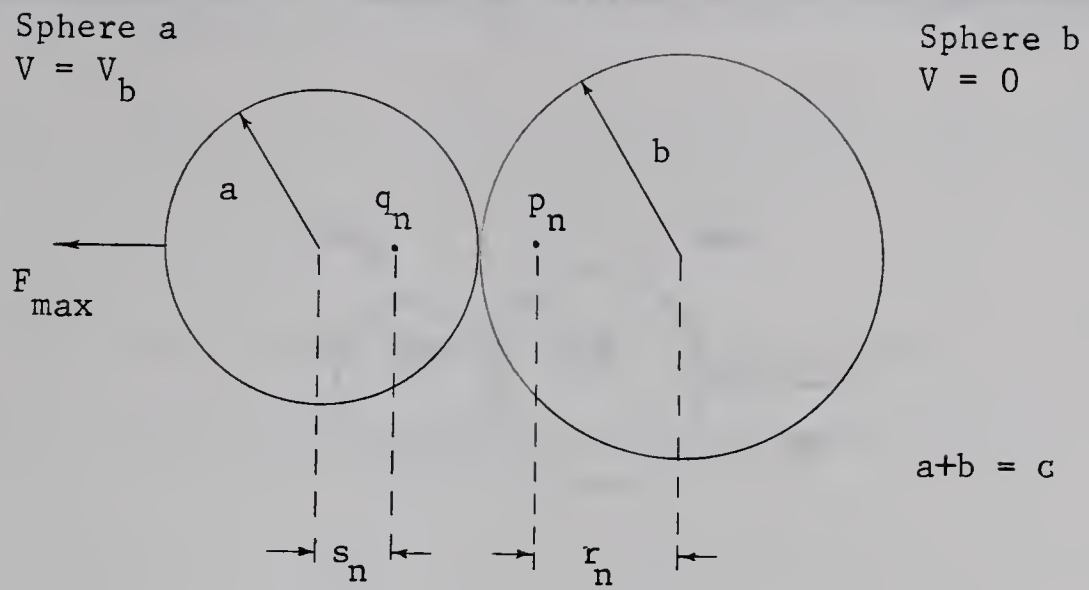


Fig. 2.3 Diagram Relevant to Computation of F_{\max}

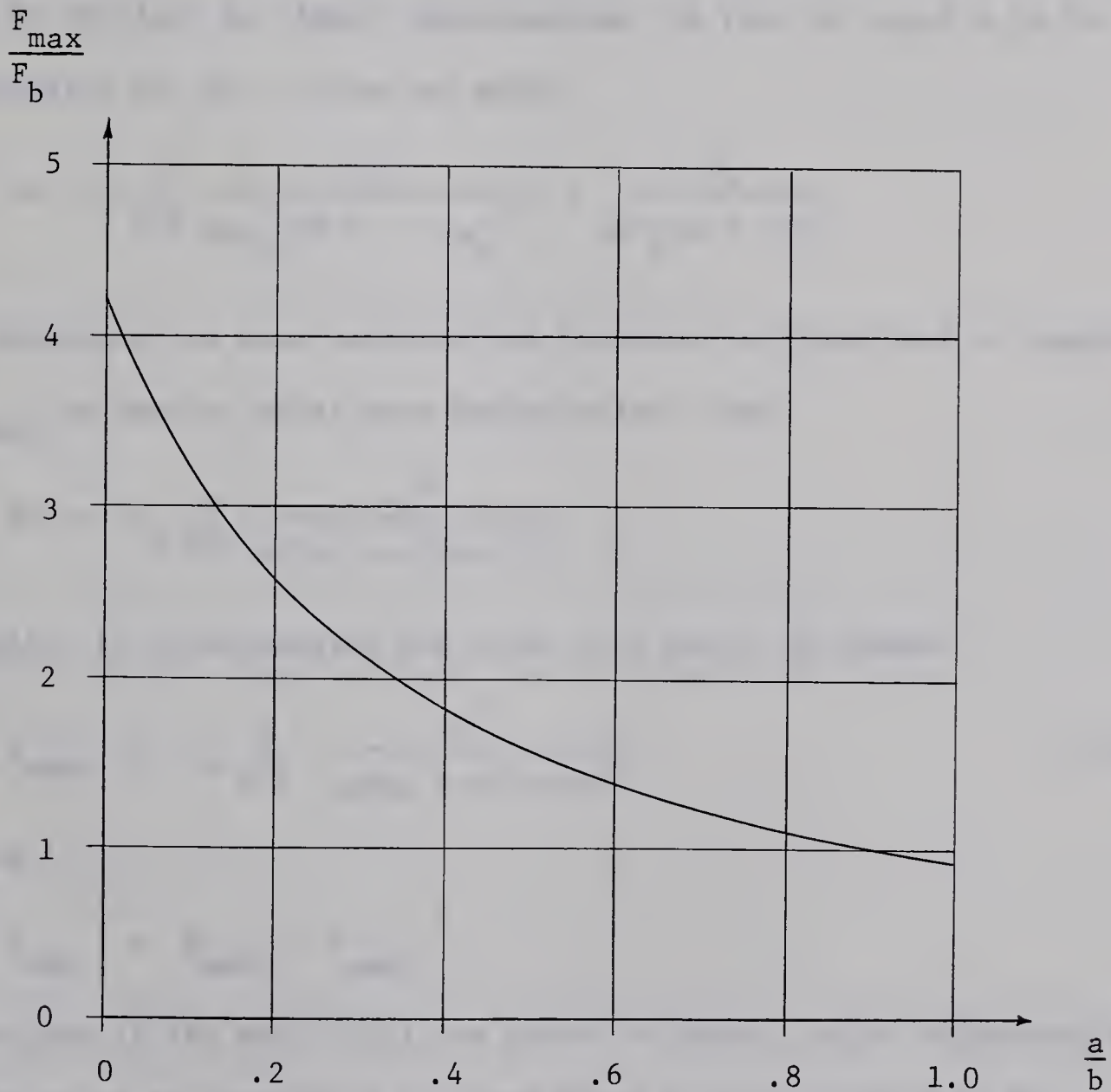
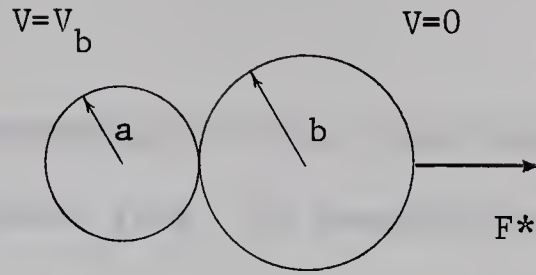


Fig. 2.4 F_{\max}/F_b versus a/b

Let us now solve for F^* , which is defined by the configuration below



It is evident that once an expression for F^* has been derived, $F_{\max 2}$ can be obtained by simply interchanging the role of a and b in the expression for F^* . Thus, we write

$$F^* = \sum_{n=1}^{\infty} \frac{q_n}{4\pi\epsilon_0 (2b + a - s_n)^2} + \frac{p_n}{4\pi\epsilon_0 (b + r_n)^2}$$

By employing the same mathematical procedure as that used to compute $F_{\max 1}$, we obtain, after some manipulation, that

$$F^* = V_b \sum_{n=1}^{\infty} \frac{-a^2}{b(2bn + a(2n-1))^2}$$

Finally, by interchanging the roles of a and b , we obtain

$$F_{\max 2} = V_b \sum_{n=1}^{\infty} \frac{-b^2}{a(2an + b(2n-1))^2} \quad \dots (2.19)$$

Since

$$F_{\max} = F_{\max 1} + F_{\max 2}$$

equations (2.18) and (2.19) are added to obtain, after regrouping the terms under the summation sign and after use of equation (2.8),

$$F_{\max} = \frac{b}{a} F_b + \frac{b^3}{a} F_b \sum_{n=1}^{\infty} \frac{1}{(2an + b(2n+1))^2} - \frac{1}{(2an + b(2n-1))^2} \dots (2.20)$$

After some further regrouping of terms, this expression can be changed to a more suitable form for computational purposes, i.e.,

$$F_{\max} = \frac{4(1 + \frac{a}{b})}{(1 + 2\frac{a}{b})^2} F_b + \frac{4b^3}{a^3} F_b \sum_{n=1}^{\infty} \frac{(2n+1)(\frac{b}{a} + 1)}{\{(2n+1)^2(\frac{b}{a} + 1)^2 - 1\}^2} \dots (2.21)$$

We can readily calculate F_{\max} for two cases, the first case again being of particular interest since it closely corresponds to the situation that is present during the actual charging process.

$$\text{Case 1: } \lim_{\frac{a}{b} \rightarrow 0}$$

For this case we obtain from equation (2.21)

$$F_{\max} = 4F_b \left(1 + \sum_{n=1}^{\infty} \frac{1}{(2n+1)^3}\right) \dots (2.22)$$

Although the sum of the infinite series on the R.H.S. of the above equation does not seem to be listed in mathematical tables, it can readily be expressed in closed form in terms of the known functions ζ_m . We write

$$\sum_{n=1}^{\infty} \frac{1}{n^m} = \zeta_m$$

and

$$\sum_{n=1}^{\infty} \frac{1}{(2n)^m} = \frac{1}{2^m} \zeta_m$$

By subtracting the second from the first of the two above equations, we obtain

$$1 + \sum_{n=1}^{\infty} \frac{1}{(2n+1)^m} = \phi_m - \frac{1}{2^m} \phi_m$$

Thus, equation (2.22) becomes

$$\begin{aligned} F_{\max} &= 4F_b (\phi_3 - \frac{1}{2^3} \phi_3) \\ &= 4.207 F_b \end{aligned}$$

Case 2: $a = b$

From equation (2.20), using $a = b$, we obtain

$$\begin{aligned} F_{\max} &= F_b + F_b \sum_{n=1}^{\infty} \frac{1}{(4n+1)^2} - \frac{1}{(4n-1)^2} \\ &= F_b (1 - \frac{1}{3^2} + \frac{1}{5^2} - \frac{1}{7^2} + \dots) \end{aligned}$$

The sum of the above series is known⁽⁶¹⁾ and yields

$$F_{\max} = 0.9160 F_b$$

To show the variation of F_{\max}/F_b as a function of a/b , a graph, Fig. 2.4, has been constructed. It is evident from Fig. 2.4 that the field intensification becomes less severe as the size of the micro-particle increases relative to the size of the charging sphere.

It has been mentioned previously that breakdown considerations ultimately limit the amount of charge that can be transferred to a microparticle. In the present case breakdown will occur as F_{\max} exceeds a particular value, F_{ult} , which is a function of the micro-particle material, the conditions at its surface, and of the vacuum

present during the charging process. If F_{ult} is exceeded, a discharge may ensue and may cause the destruction of the microparticle and charging sphere, unless the current that is supplied to the latter by the external high voltage source is limited to a safe value. The microparticle may still be destroyed or the amount of charge that is retained may be diminished.

With the above considerations in mind, let us assume that, for various values of a/b , the potential of the charging electrode is raised to such a value that $F_{max} = F_{ult}$. We can then compute F_a , the field intensity on the microparticle after its charge has become uniformly distributed, and compare it to F_{ult} . We proceed by substituting F_{ult} for F_{max} in equation (2.21) to obtain the appropriate value of F_b (which, in turn, determines V_b). This value of F_b is then used in equation (2.9) to obtain the ratio F_a/F_{ult} , i.e.,

$$\frac{F_a}{F_{ult}} = \frac{\left(\frac{b}{a}\right)^2 \sum_{m=2}^{\infty} \left(\frac{a}{a+b}\right)^m}{\frac{4(1+\frac{a}{b})}{(1+2\frac{a}{b})^2} + 4 \frac{b^3}{a^3} \sum_{n=1}^{\infty} \frac{(2n+1)(\frac{b}{a} + 1)}{\{(2n+1)^2(\frac{b}{a} + 1)^2 - 1\}^2}} \quad \dots (2.23)$$

The numerator of the above expression has already been plotted in Fig. 2.2, and the denominator in Fig. 2.4. Values of F_a/F_{ult} can thus be readily calculated. They are plotted in Fig. 2.5 to compare the field intensities that can be established on microparticles by contact charging for various values of a/b , with the ultimate field

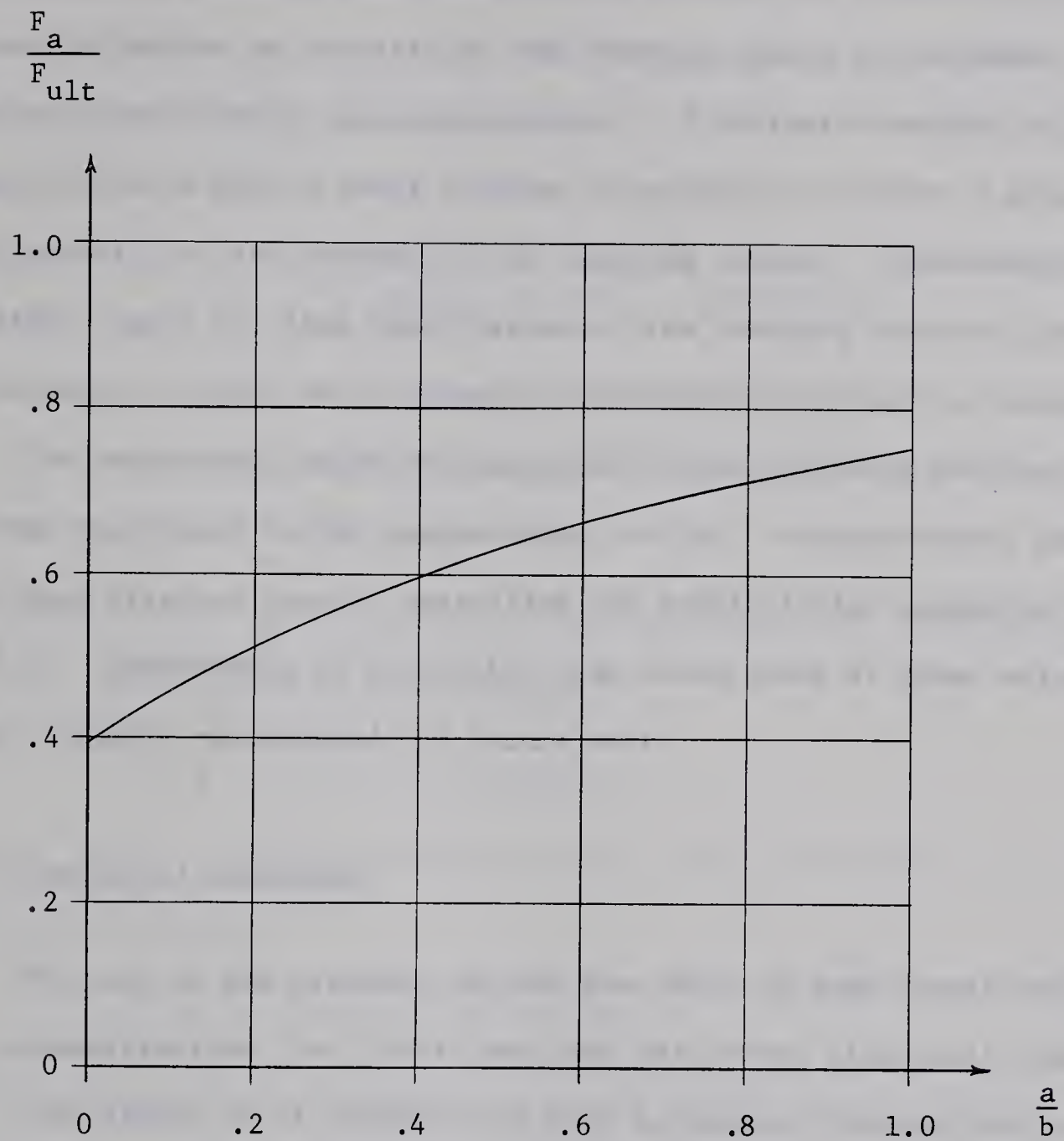


Fig. 2.5 F_a/F_{ult} versus a/b

intensity that can be supported by the microparticle material.

Fig. 2.5 suggests that the charging process can inherently be made more effective as the size of the charging sphere is decreased relative to the size of the microparticle. A further advantage to be gained by this is that a lower voltage is required to produce a given field intensity at the surface of the charging sphere. Disadvantages that might result are that the lifetime of the charging electrode and the frequency at which it is struck by microparticles would be decreased.

The experiments which are described in the following sections have been restricted to the region where $a \ll b$. No experiments have as yet been directed towards exploiting the possibilities suggested by Fig. 2.5. Experiments of the latter type could prove of great value and are strongly recommended for future work.

2.1.4 Electrical Breakdown

The work of the previous section has dealt in some detail with field intensification, but little has been said about electrical breakdown. The latter is of interest not only to contact charging but to particle charging experiments in general, because it imposes the inherent upper limit upon the amount of charge that can be retained by a particle of given size and material and thus determines the ultimate velocity to which this particle can be accelerated by a given potential. The maximum field intensity that can be sustained at the surface of a negatively charged particle is limited by electron field emission. If the particle is positively charged, its maximum surface field intensity is limited by ion evaporation. For most metals, the latter surface field

intensity is about one order of magnitude higher than the former⁽⁶²⁾. For this reason, positive charging is preferred. One can estimate the field intensity at which field evaporation of an ion on a metal surface of its own kind takes place by the following formula⁽⁶³⁾, which is valid at temperatures below 100°K:

$$F = \frac{(\Lambda + V_I - \phi)^2}{0.144} \cdot 10^8 \quad \text{volts/meter}$$

where

Λ = heat of evaporation of the atom in ev

V_I = ionization energy of the removed atom in ev

ϕ = work function of the metal in ev.

For tungsten, which has proved to be a suitable metal for the charging electrode, the above yields approximately

$$F = 10 \cdot 10^{10} \text{ volts/meter}$$

For iron, which is readily available in the form of spherical microparticles, we obtain

$$F = 4.5 \cdot 10^{10} \text{ volts/meter}$$

The above values have never been attained in microparticle charging experiments, presumably because the idealized particle surface conditions and the environment for which the foregoing equation is valid, were not present.

The vacuum that exists during the charging process is of particular importance. Vedder⁽⁶⁴⁾ has conducted experiments during which electrostatically contained microparticles were charged positively by an ion current. He found that for a given pressure in the charging chamber an equilibrium was reached between the charging rate and the

charge loss by the particle to the surrounding gas. For a given particle, the use of liquid helium cryopumping resulted in a threefold increase in the equilibrium charge to mass ratio, over the ratio obtained with liquid nitrogen trapped pumping. Using liquid helium cryopumping, the maximum surface field intensity obtained on iron particles (after a charging time of up to 2 hours) was $1.4 \cdot 10^{10}$ volts/meter. The theoretical maximum, as indicated before, is $4.5 \cdot 10^{10}$ volts/meter.

Another factor of consequence to charging experiments, is that great mechanical stress is exerted upon a particle by a high electric field intensity at its surface. This stress is

$$S = \frac{1}{2} \epsilon_o F^2$$

If we consider $F = 4.5 \cdot 10^{10}$ volts/meter, the theoretical field evaporation field intensity of iron, S is computed to be 0.912 tons/mm^2 ($1.3 \cdot 10^6$ psi). This value of S is many times larger than the bulk tensile strength of iron, or that of other materials. Nevertheless, many microparticle materials may be able to withstand stresses of this magnitude, because, due to lack of imperfections, micron sized samples may exhibit far greater strength than the bulk material. Some materials, however, are structurally so weak, that the microparticle may fracture at a much lower surface field intensity than that quoted above.

Hollow SiO_2 microspheres⁽⁶⁴⁾, for example, are so fragile, that in spite of their low bulk densities, they can only support relatively low charge to mass ratios.

2.2 Experimental Work

2.2.1 High Vacuum System

A complete high vacuum system was constructed, and used for all of the following experiments. The system consists of a 2 inch, 3 stage oil diffusion pump with a liquid nitrogen trap. Pressure measurements were made by means of Pirani and ionization gauges. As the system often operated for long periods of time, unattended, safety devices were constructed to protect the system against power failures, pump cooling water supply failures and rises in system pressure. The experiments were conducted in a 4 inch I.D. Pyrex glass cross which was sealed with brass end plates and rubber O-rings. The usual pressures that were present ranged from $1 \cdot 10^{-6}$ to $5 \cdot 10^{-5}$ torr. A block diagram of the high vacuum system is shown in Fig. 2.6.

2.2.2 Particle Charging Mechanism

The particle charging mechanism that has been constructed is shown schematically in Fig. 2.7.* The device consists of three brass walls, A, B and C, that are separated and insulated from each other by two teflon cylinders. (The function of the corrugated insert marked E will be explained later.) A copper tray is affixed to wall A and

* The technique of contact charging of microparticles has been developed at Ramo-Wooldridge⁽⁶⁵⁾ and Space Technology Laboratories⁽⁶⁶⁾. The charging mechanism and particularly the high voltage pulsing circuit that are described above are similar to ones presently in use at Space Technology Laboratories. A complete diagram of the high voltage pulsing circuit is given in Fig. A.1 in the appendix.

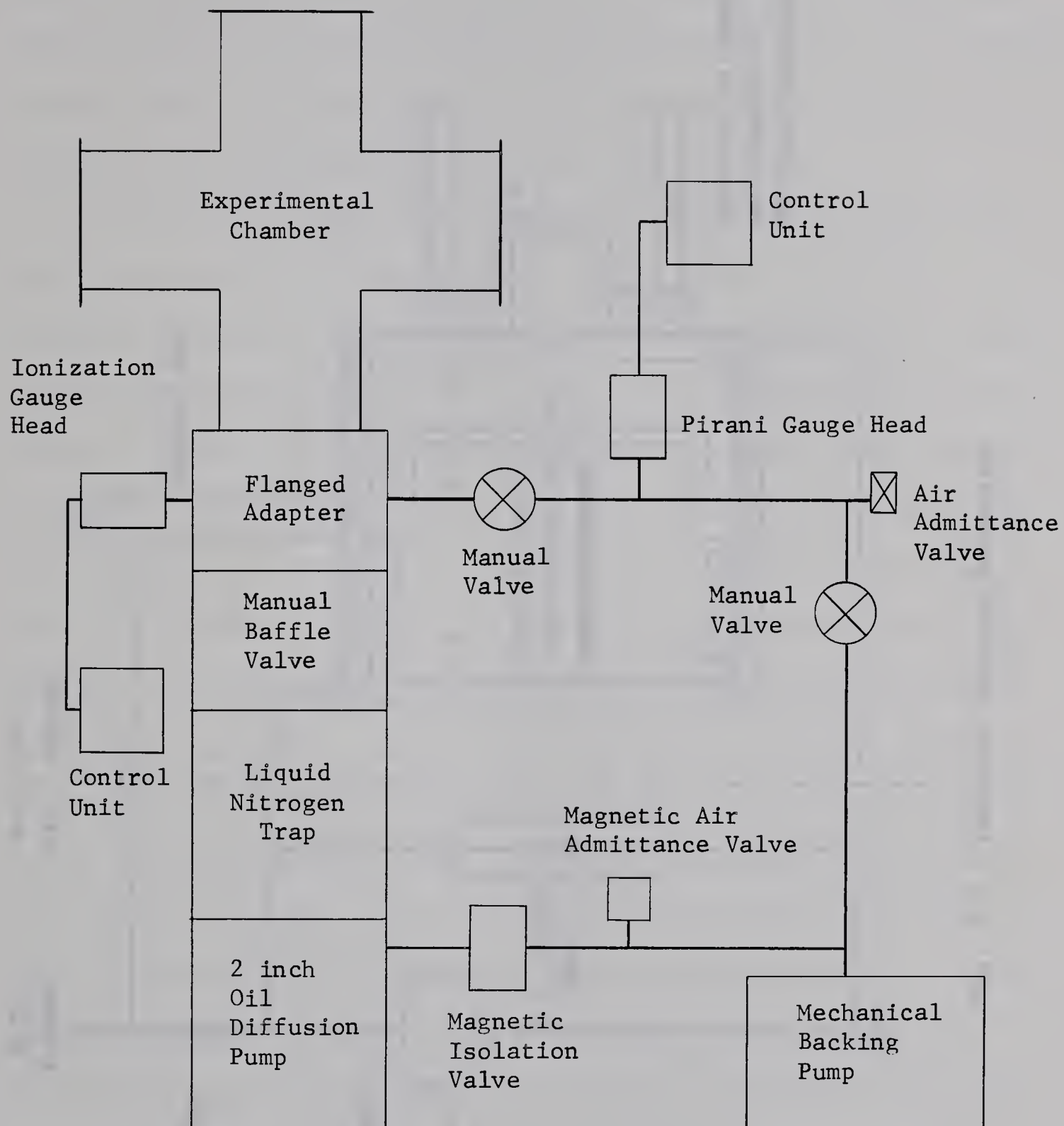


Fig. 2.6 High Vacuum System

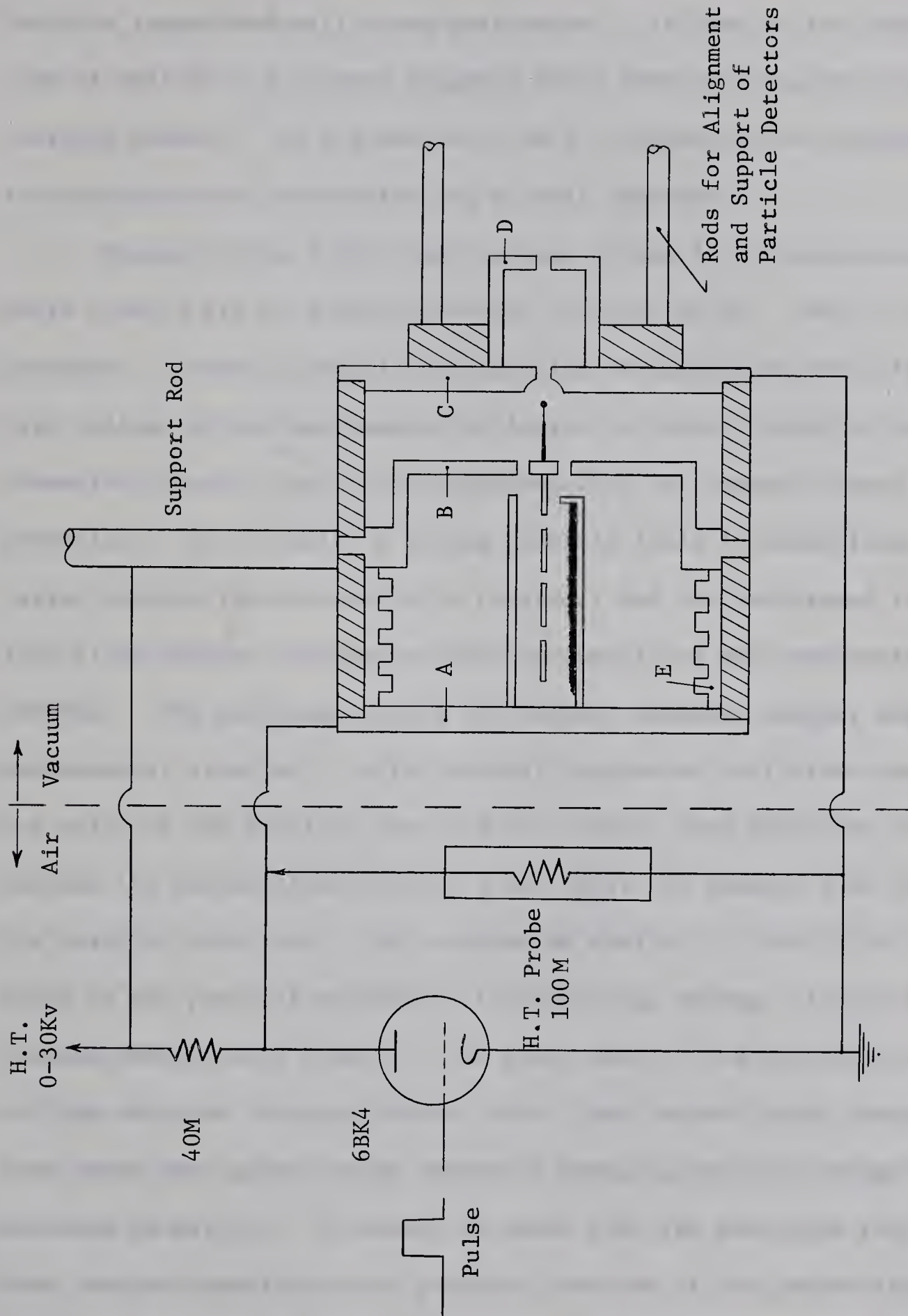


Fig. 2.7 Particle Charging Mechanism

serves as the microparticle reservoir. Protruding into this reservoir is a brass tongue that is attached to the left hand side of wall B. Both the tongue and wall B are perforated. Affixed to the right hand side of wall B is a tapered tungsten shaft whose end supports the tungsten charging sphere. In the centre of wall C, opposite the charging sphere, is a hemispherical depression and a small aperture.

Normally, the 6 BK 4 high voltage triode is non-conducting and walls A and B are at a high potential of about 20 Kv. Wall C is grounded. If now a positive going pulse is applied to the grid of the high voltage triode and causes the latter to conduct heavily, then the potential of wall A and of the charging tray is lowered to near ground potential. As a result, a strong electric field is established in the region between the microparticle reservoir and the perforated tongue. This field induces a charge on the microparticles and accelerates them upwards. The particles strike the tongue, exchange charge, and are subsequently repelled. After several successive collisions between the walls of the particle tray and the tongue, some particles escape through the perforations in wall B and enter the chamber that contains the charging electrode. By a mechanism similar to that which took place in the particle reservoir, the particles undergo alternate collisions between walls B and C. In time, some of the particles will collide with the charging sphere, where they become highly charged and from where they subsequently escape to ground potential through the aperture in wall C. It should be noted that the particles that are thus charged constitute only a minute fraction of the powder that is loaded into the particle reservoir. Most of the powder, after having left the reservoir, settles in regions where the electric field is

relatively weak, i.e., on the interior surfaces of the teflon insulating cylinders. The operation of the charging mechanism ceases when the charging reservoir has been emptied, which will usually occur after several hundred to a thousand high voltage pulses have been applied.

Exploded views, that show all the components of the charging mechanism that have been described above, are shown in Fig. 2.8. A view of the charging mechanism suspended in the experimental chamber is shown in Fig. 2.9. The high voltage leads enter the top and left hand arms of the chamber. The right hand arm of the chamber and its extension contain particle detection equipment which will be described later. Some of the high vacuum equipment is visible in the lower half of the picture.

2.2.3 Observations and Experiments

A. Particle Emission

The frequency at which particles are detected beyond the charging mechanism varies from one particle for every few high voltage pulses to several particles per pulse. The frequency of emission was found to be dependent upon a large number of factors:

1. Location of charging sphere with respect to the hemispherical depression and the aperture in wall C. The optimum location of the charging sphere along a line coincident with its supporting shaft was determined by a trial and error process. If one considers the intersection of the hemisphere and of the electrode shaft as a reference point, then the optimum location is at a distance a little less than one hemisphere radius (the radius is approximately 2.5 mm) to the left of the



Fig. 2.8 Exploded Views of the Charging Mechanism

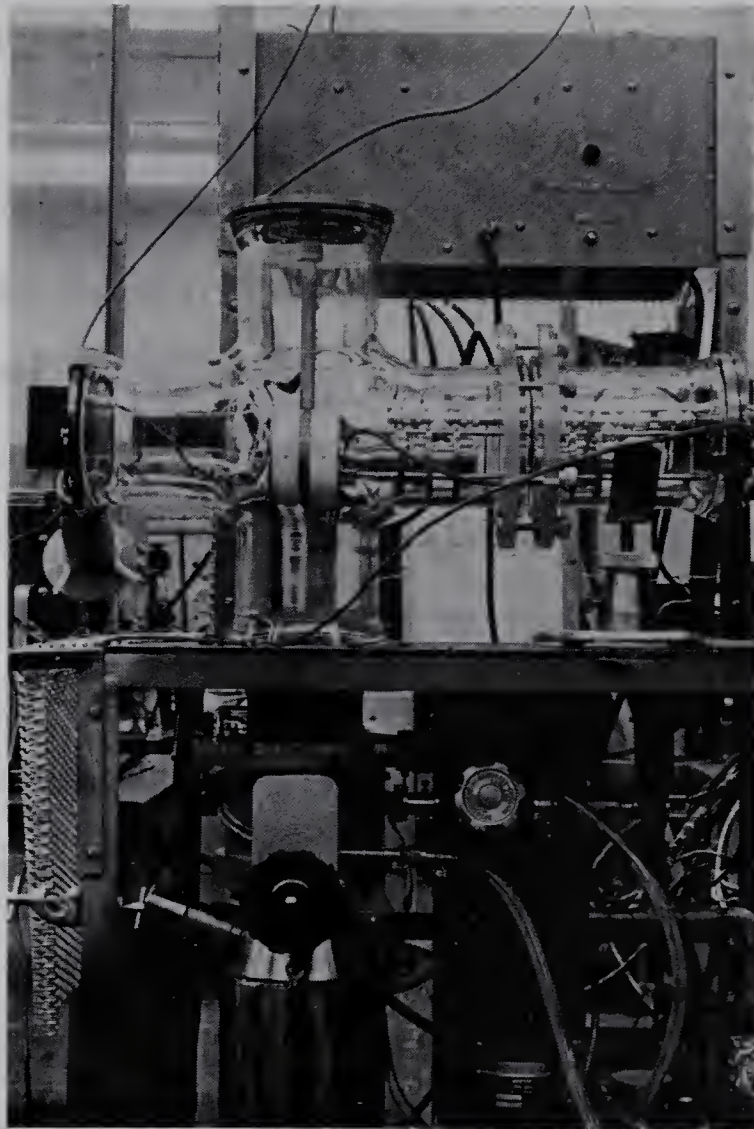


Fig. 2.9 Charging Mechanism and Associated
Experimental Equipment

reference point. (Refer to Fig. 2.7.) This coincides closely with the intersection of the interior surface of wall C and the axis of the electrode shaft.

The charging sphere was centered in a direction perpendicular to its shaft by the following method. After the right hand chamber of the charging mechanism had been assembled and aperture D removed, the charging sphere could be observed through the aperture in wall C by use of a medium power microscope. The microscope had a sufficiently long working distance and enough depth of field, so that, by a very slight change of focus, the sphere and the aperture in wall D could alternately be brought into focus. The relative position of the charging sphere could thus be determined. By removing wall C and rotating the charging electrode, which was never perfectly straight, in its socket in wall B, the charging sphere could usually, by a trial and error process, be accurately centered with respect to the aperture in wall C.

2. The size of aperture D. Since particles leave the charging sphere at various angles, it was found necessary to place a second aperture in the path of the particles to permit only those to pass that were well enough aligned for detection experiments. Although no specific experiments were conducted, it seems that the charging mechanism emits particles fairly uniformly throughout the solid angle defined by the charging sphere and the aperture in wall C. The overall frequency of emission is, therefore, approximately proportional to the area of aperture D.

3. Microparticle size. Commercially available carbonyl iron powder was the microparticle material that was used for all experiments. The powder consists of individual microspheres, and the samples used had average (weight based) diameters of 3, 8, 10 and 20 microns. It was noted that the frequency of emission increased with decreasing particle size; that is, more particles were emitted per high voltage pulse if the reservoir contained 3 micron rather than 20 micron average diameter powder. Also, for any given powder sample, the fraction of the smallest particles emitted was much larger than the fraction of these particles present in the sample. For instance, the particle size distribution for the 3 micron average diameter powder, as quoted by the manufacturer, indicates that the weight fraction of particles with diameters less than 2 microns is 30%. Yet, when particles emitted by the charging mechanism were analyzed, it was found that nearly all of these particles had diameters of less than 2 microns. (In one experiment, 13 emitted particles were analyzed. Their diameters ranged from .95 microns to 2.2 microns. 11 of these particles had diameters of less than 2 microns.)

A possible explanation for these phenomena can be proposed if we examine the behaviour of the microparticles in the particle reservoir. When a particle collides with a surface of either the particle reservoir or the perforated metal tongue, it acquires a charge to mass ratio that is inversely proportional to its radius. Thus, since all particles are acted upon by the same electric fields, a smaller particle will

* Carbonyl iron powder is available from Antara Chemicals, General Aniline and Film Corporation, 435 Hudson Street, New York 14, N.Y., U.S.A.

subsequently experience a high acceleration and thus have a higher average velocity than a larger particle; that is, the smaller particle collides more frequently with the walls by which it is surrounded. The probability of escape through the perforations in wall B, therefore increases as the size of the particle decreases. Consequently, the weight fraction of small particles in the right hand chamber of the charging mechanism will be higher than in the original powder. Also, due to their higher velocities, the flux density of these smaller particles is enhanced relative to the larger and slower particles. The sum total of the above effects is that the probability that a given particle strikes the charging sphere increases as its size decreases.

4. Voltage applied to charging electrode and the magnitude of the pulse applied to the charging reservoir. It is evident from Fig. 2.7 that these two quantities are interrelated. It was generally noted that the high voltage had to be increased to some threshold level before particles were emitted by the charging mechanism. The threshold voltage varied between approximately 12 Kv and 18 Kv, depending somewhat upon the average diameter of the microparticle powder and the quantity of powder present in the charging reservoir. (Since the electric field intensities, rather than voltages, determine how effectively the particles are agitated in the particle reservoir and between walls B and C, the physical dimensions of the charging mechanism are of importance as well. Fig. 2.7 is approximately full size.)

For some experiments, particularly those that used the larger diameter powders, it was found desirable to increase the frequency at

which particles were emitted. This was accomplished by leaving in place a high voltage probe that was usually only connected at the beginning of an experiment to monitor the plate voltage of the 6 BK 4, while the high voltage pulsing circuit was being tested. Since the input impedance of the high voltage probe was 100 M and that of the 6 BK 4 plate resistor 40 M, a DC potential of approximately 30% of that applied to the charging electrode was maintained between the particle reservoir and the perforated tongue while the experiment was being conducted. (See Fig. 2.7.) This potential, in addition to occasionally applied high voltage pulses, resulted in the desired increase in particle emission.

B. Breakdown Phenomena

The carbonyl iron powder, when in bulk form, is non-conducting. However, at times, while a charging experiment was being conducted, breakdown took place within the powder and a conducting path was formed. For the purpose of describing this phenomenon, one must imagine the charging mechanism, Fig. 2.7, in the form in which it was initially employed, that is, without the corrugated perspex insert marked E. During operation of the charging mechanism, the particle reservoir was gradually emptied and the majority of the microparticles settled on the interior surface of the left hand teflon cylinder. At this point, during several of the experiments, a conducting path formed through the powder and caused a short circuit between walls B and A. As a result, the operation of the charging mechanism ceased. After disassembly and examination of the interior surface of the left teflon cylinder

under a medium power microscope, it was found that the conducting path consisted of a chain of microparticles that had fused at their adjacent surfaces. The structure of the conducting path was similar to that of a necklace whose beads consisted of either individual or small clusters of microparticles. The conducting path and the microparticle powder that had settled on the interior surfaces of the charging mechanism were easily removed by a jet of compressed nitrogen.

The above breakdown phenomenon reoccurred during several succeeding experiments. Disassembly, cleaning and reloading of the charging mechanism, and subsequent re-evacuation of the experimental chamber was a time consuming operation. Attempts were therefore made to destroy the short circuit by passage of a high current while the charging mechanism was in the experimental chamber and under high vacuum. These attempts failed, presumably because heating of any particular section of the conducting path fused further particles to it, and thus strengthened it rather than destroyed it.

The occurrence of breakdown was finally eliminated by employing a corrugated insert in the left hand chamber, as shown in Fig. 2.7. This scheme was successful, because, during operation of the charging mechanism, microparticle powder now settled in the troughs of the inserts while the ridges were kept clean. A continuous microparticle path between walls A and B, thus no longer existed. Also, by use of the corrugations, the length of any potential breakdown path had been increased, thus making the possibility of breakdown more remote.

C. Charge to Mass Ratios

The particles emitted by the charging mechanism were analyzed as they passed through a series of detectors. The detectors are sensitive to either the charge carried by a particle, or to the light scattered by it as it passes through a well defined, intense beam of light. The methods of detection are described in detail in the next chapter. For the following discussion it is sufficient to note that the detectors are capable of measuring the amount of charge carried by a particle and the instants in time at which it passes a series of given points in space. Thus, from the detector data, the particle's charge q and its velocity v can be obtained. Also known is V , the potential of the charging electrode, i.e. the potential through which the particle has been accelerated prior to passing through the system of detectors.

Now, consider the well known relationship

$$\frac{1}{2} mv^2 = qV \quad \dots(2.24)*$$

Since v and V are known, the above relationship can be used to compute the particle's charge to mass ratio, i.e.,

$$\frac{q}{m} = \frac{v^2}{2V} \quad \dots(2.25)$$

If it is assumed that the particle is spherical, then its radius can be computed, i.e.,

$$a^3 = \frac{3m}{4\pi\rho}$$

* In applying equation (2.24) it is assumed that particles leave the charging sphere at zero velocity, i.e. their rebound velocity is neglected. This assumption may introduce significant error, since there is evidence that suggests that microparticles strike the charging sphere with considerable velocity. This is further discussed in section 2.2.3 D.

or

$$a = \left(\frac{3qV}{2\pi\rho v^2} \right)^{1/3} \quad \dots (2.26)$$

A series of charged particles have been analyzed by the detection devices mentioned above, and, by use of equations (2.25) and (2.26), their charge to mass ratios and their radii have been computed. They are plotted in Fig. 2.10 and Fig. 2.11. The accuracy of this data depends upon the validity of the physical model, i.e. spherical particles and zero rebound velocity from the charging sphere, and upon the precision of the electronic measurements. The latter will be discussed further in a later section; for the present, it is assumed to be:

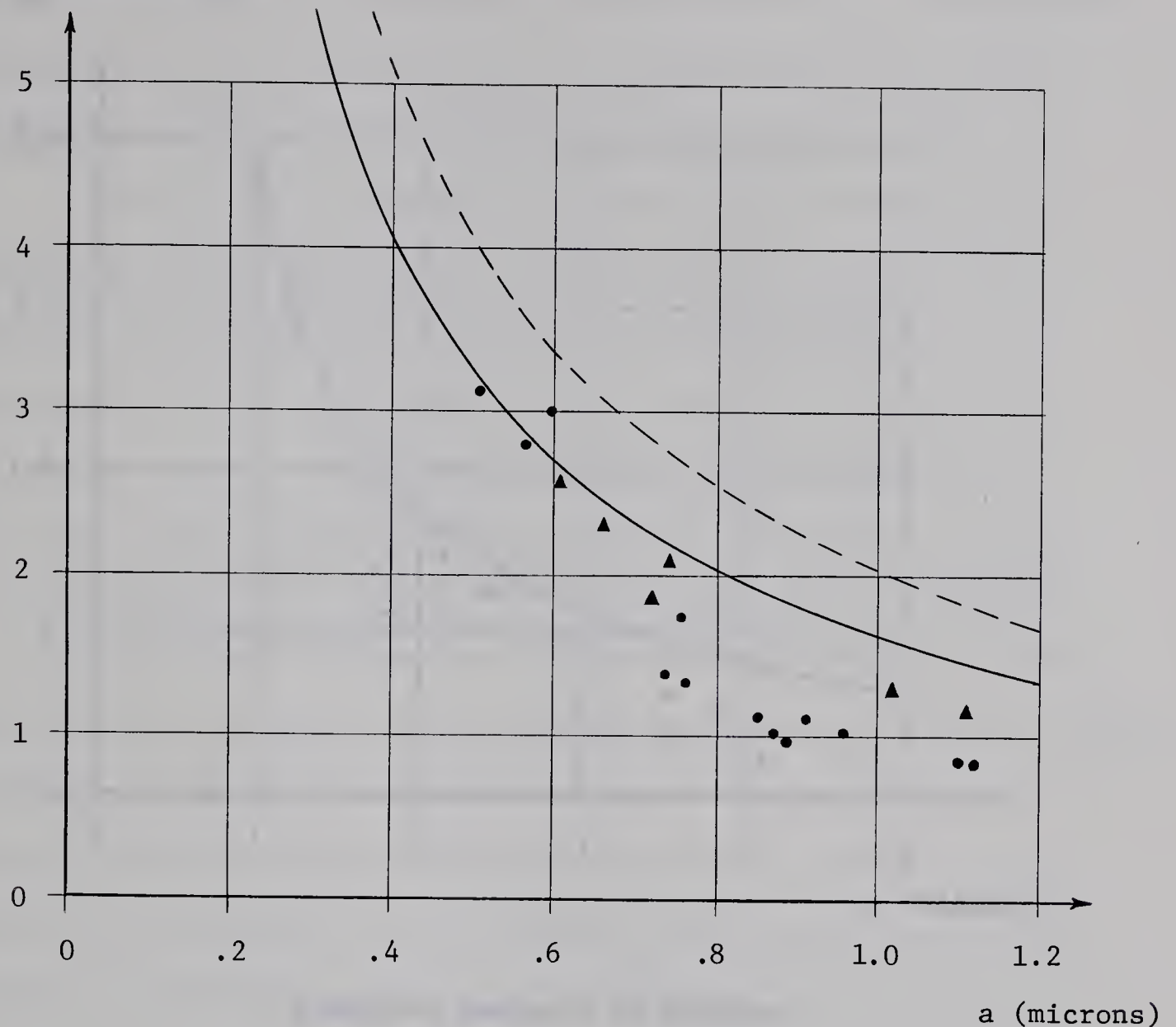
charge measurement q	$\pm 9\%$ to $\pm 16\%$
velocity measurement v	$\pm 5\%$
high voltage measurement V	$\pm 2\%$

From equation (2.25), the error in charge to mass ratio is, thus, approximately 12%. From equation (2.26), the error in radius is approximately 13%.

To compare the foregoing experimental values with those predicted by calculations based on the idealized mathematical model and the method of image charges (section 2.1), the "theoretical" relationships between particle charge to mass ratio and radius have been superimposed upon Fig. 2.10 and Fig. 2.11. This relationship is, from equations (2.8) and (2.13), for $a \ll b$, and with subscripts deleted,

$$\frac{q}{m} = \left(\frac{\pi^2 \epsilon_0 V}{2\rho b} \right) \left(\frac{1}{a} \right) \left(1 - 1.27 \frac{a}{b} \right) \quad \dots (2.27)$$

$\frac{q}{m}$ (coulombs/Kg)

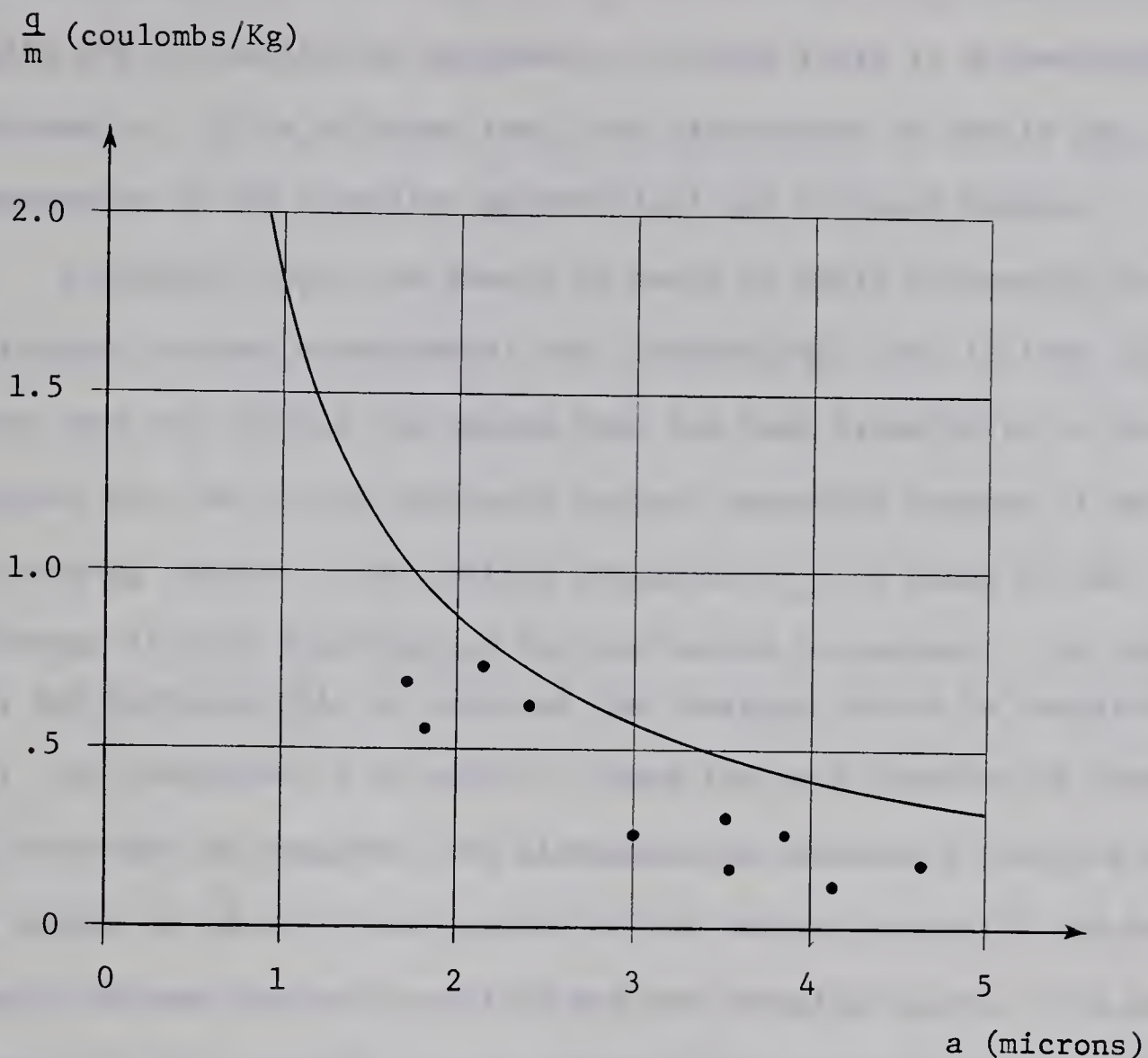


Electrode Radius = 55 microns

Electrode Potential	16 Kv	20 Kv
Experimental Values	●	▲
Theoretical Curve	—	- - -

Note: The parameters of these particles were computed from the data obtained from charge sensitive detectors. The particles are GAF carbonyl iron: type SF, physically hard, 3 micron average (weight based) diameter.

Fig. 2.10 Charge to Mass Ratio versus Radius for Carbonyl Iron Microparticles.



Electrode Radius = 55 microns

Electrode Potential 18 Kv

Experimental Values ●

Theoretical Curve —

Note: The parameters of these particles were computed from the data obtained from a combination of charge sensitive and photoelectric detectors. The particles are GAF carbonyl iron: type MR, physically soft, 20 micron average (weight based) diameter.

Fig. 2.11 Charge to Mass Ratio versus Radius for Carbonyl Iron Microparticles.

As seen from Fig. 2.10 and Fig. 2.11, experimental and "theoretical" results are in qualitative agreement, although there is a quantitative discrepancy. It is believed that this discrepancy is due to the inadequacies of the idealized mathematical and physical models.

A further factor one should be aware of while discussing the discrepancy between experimental and "theoretical" q/m , is that the latter does not include the charge that has been transferred to the microparticle due to the intrinsic contact potential between it and the charging sphere. The contact potential, V_c , is equal to the difference in work functions of the two metals in contact. In this case, the microparticle is iron and the charging sphere is tungsten, and V_c is, therefore, 0.35 volts. Since the work function of iron is less than that of tungsten, the microparticle acquires a positive charge. This charge is equal to the product of the contact potential and the capacity between the microparticle and the charging sphere. An expression for the capacity can be obtained from equation (2.1) if one considers the charging sphere to be grounded, i.e.,

$$\text{capacity} = c_{11} = \frac{q_1}{V_1}$$

The diagram relevant to the above equation is Fig. 2.1. If the radius of the microparticle is much smaller than that of the charging sphere, then, from equation (2.2), one obtains

$$c_{11} = 4\pi\epsilon_0 a \sinh \alpha \sum_{n=1}^{\infty} \text{csch } n \alpha$$

and $\alpha = \cosh^{-1} \left(\frac{D}{a} \right)$

where D = distance from the surface of the charging sphere to the centre of the microparticle.

Cho⁽⁶⁷⁾ has computed c_{11} to obtain the capacity of a sphere on a plane, when the radius of the sphere is 1 micron and the separation between the two is the intermolecular distance, i.e. 10^{-8} cm. Cho's result is $c_{11} = 6.5 \cdot 10^{-16}$ farads. Thus, for a contact potential of 0.35 volts, the charge acquired by the sphere is $2.3 \cdot 10^{-16}$ coulombs. When compared to the data of Fig. 2.10, this charge is less than 1% of the total charge carried by a typical particle whose radius is one micron.

D. Cratering Phenomena

Figs. (2.12), (2.13) and (2.14) are photomicrographs of the surface of a tungsten charging sphere that has been in operation for many hours. The photomicrographs show innumerable small indentations and several large craters. The indentations are believed to be due to the bombardment of the charging sphere by the carbonyl iron microparticles. The craters may have been similarly formed, but it is not known why they are so much larger than the indentations. Two mechanisms that might possibly be responsible for the formation of the craters are suggested:

1. An approaching microparticle causes a field intensification at the surface of the charging sphere. This, in turn, leads to breakdown and to a subsequent discharge between the charging sphere and the grounded hemispherical depression in wall C. (See Fig. 2.7) As a result, local melting occurs at the surface of the charging sphere. The approaching particle is thus able to embed itself to great depth and form an unusually large crater. Subsequently, the discharge

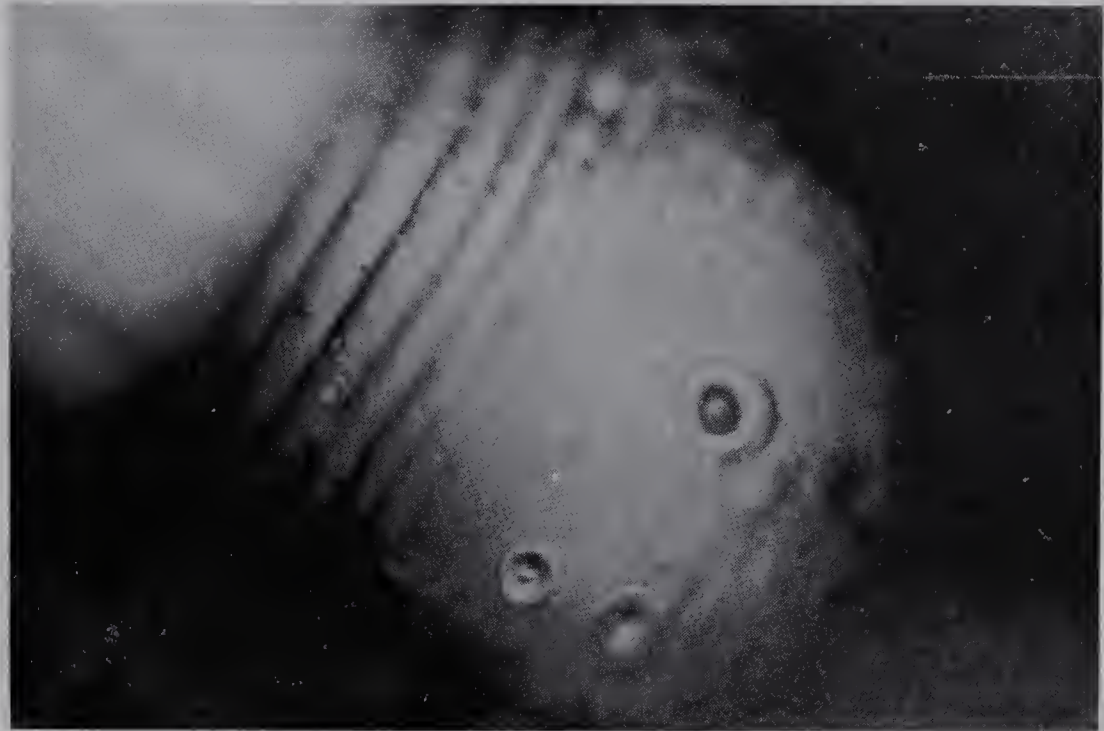


Fig. 2.12 Cratering Phenomena (Approx. 750x)

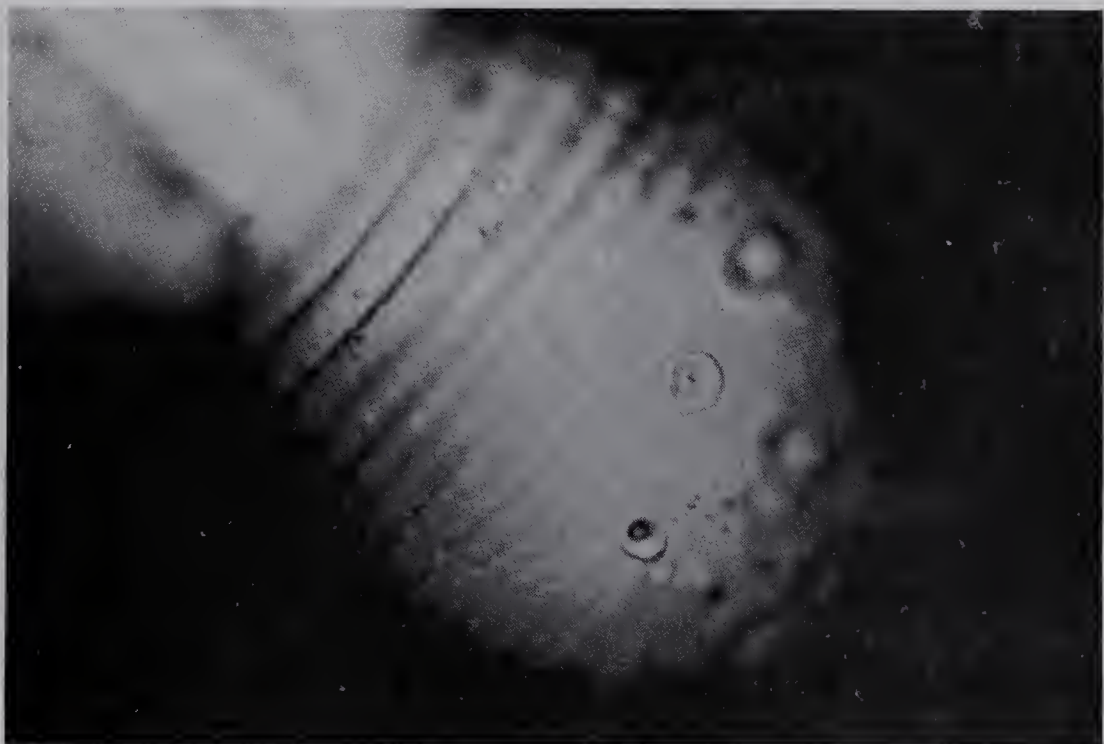


Fig. 2.13 Cratering Phenomena (Approx. 750x)

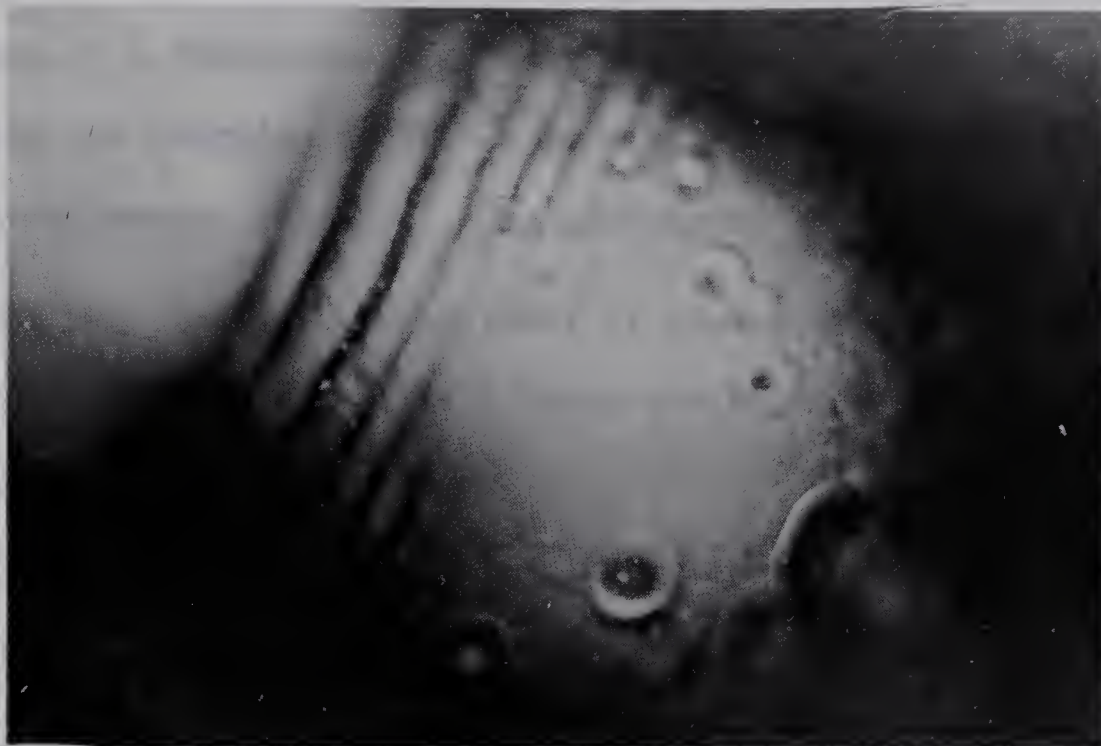


Fig. 2.14 Cratering Phenomena (Approx. 750x)

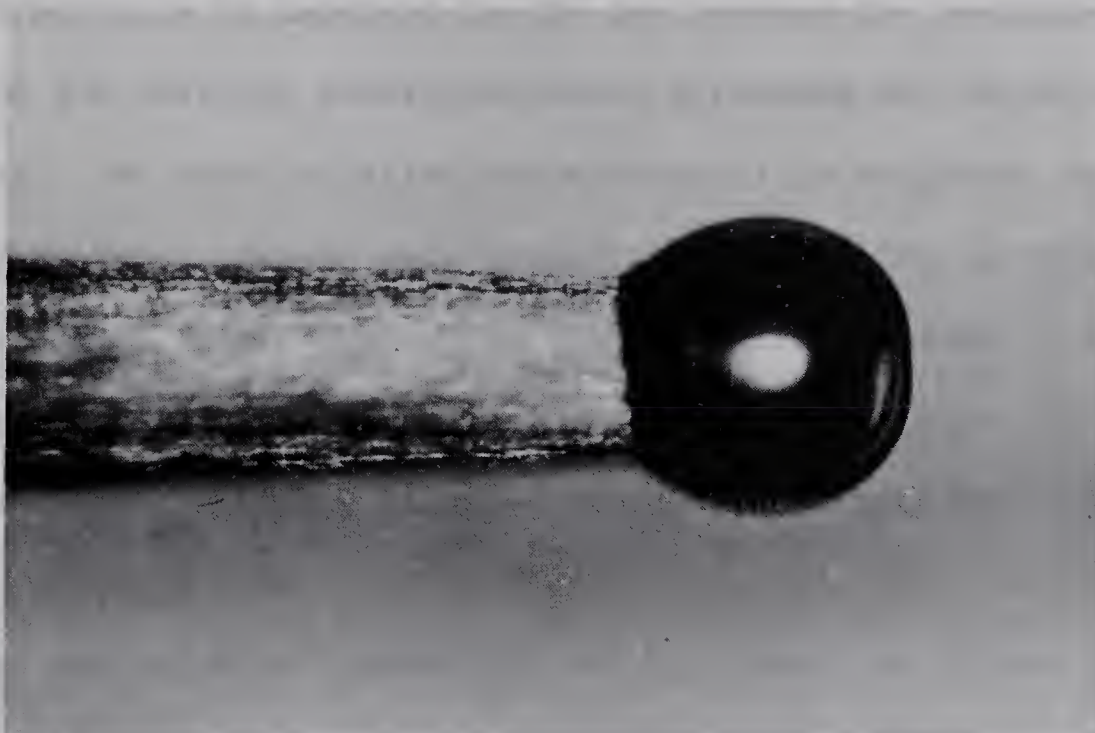


Fig. 2.15 Photomicrograph of a Charging Sphere
with a Radius of 62 Microns

ceases so that the charging sphere is not destroyed.

It should be noted that the formation of a discharge is aided by the presence of a relatively high gas pressure; that is, the pressure within the charging mechanism is significantly higher than that in the experimental chamber. The reasons for this are:

a) The sum total of the surfaces of the microparticles within the charging mechanism is exceedingly large and thus requires a long time to outgas.

b) The interior surfaces of the charging mechanism are steadily bombarded by microparticles and, therefore, continually outgas.

c) The particle exit aperture is the only opening in the walls of the charging mechanism, and therefore, the pumping speed within the latter is very small.

2. A microparticle is captured in the gap between the hemispherical depression and the charging sphere, and makes alternate collisions with either surface. At each collision the microparticle exchanges charge and is then repelled. During each transit of the gap the particle gains kinetic energy from the electric field. Although some of this energy is dissipated each time the particle makes a collision, in time it attains sufficient velocity to embed itself in the tungsten charging sphere.

If this mechanism is responsible for the formation of the craters, then these should also be found on the hemispherical depression opposite the charging sphere. Due to the concave shape of the hemispherical depression, which makes it unsuitable for observation under a high

power objective with a short working distance, and due to its machined surface, which is very rough on a microscopic scale, no conclusive microscopic examination could be conducted to either support or disprove the foregoing cratering mechanism.

In concluding this section, it must again be stressed that, until further experiments have been conducted, both cratering mechanisms that have been suggested continue to be of a speculative nature.

2.2.4 The Manufacture of Charging Electrodes

Charging spheres are formed at the ends of tapered tungsten shafts. Initially, the shafts consist of tungsten needles with a uniform diameter of 0.50 mm. Several needles at a time are fastened in a vertical position to a movable platform which is then lowered so that the ends of the needles enter a 50% - 50% mixture of nitric and hydrofluoric acid. Subsequently, the platform is raised very slowly by a lever and reduction gear arrangement which is driven by an electric motor. The needles are thus withdrawn at a uniform rate over a period of several minutes. Due to the differential etching, each needle acquires a smooth taper which terminates in a microscopic point.

One of these needles is now clamped to a specially constructed device, which, by means of a three way micrometer adjustment, makes it possible to bring the needle into alignment with another tapered tungsten needle that has a smoothly blunted tip. The alignment is performed while the needles are observed under a medium power microscope. The needles are now moved towards each other until their tips make electrical contact. Whether or not contact has been established is most accurately

determined by electrical resistance measurements, rather than through visual microscopic observation. At this point a bank of capacitors is discharged through the tips of the needles. The discharge melts the more finely tapered tip, which, upon solidification, shrinks into a microscopic sphere. The size of the sphere is controlled by the voltage and size of the bank of capacitors, which ranged from 50 to 200 volts and 20 to 200 microfarads. Often, the same needle was subjected to several discharges to successively increase the size of the sphere at its end. Initially, the discharges took place in air, with the result that the surfaces of all spheres were oxidized. This made it difficult to examine the spheres for imperfections. During subsequent trials, a small jet of nitrogen was blown past the needles while the discharge took place. This resulted in the production of very smooth spheres with mirror-like surfaces. A photomicrograph of a sphere with a radius of 55 microns is shown in Fig. 2.15. A photograph showing a discharge, the needle adjustment mechanism and the observation microscope is shown in Fig. 2.16.

Typically, the foregoing procedure yielded one or two suitable electrodes for every ten trials. Once an electrode had thus been produced, its shaft length was measured by a travelling microscope. The shaft was then ground to proper length on a high speed diamond grinding wheel.

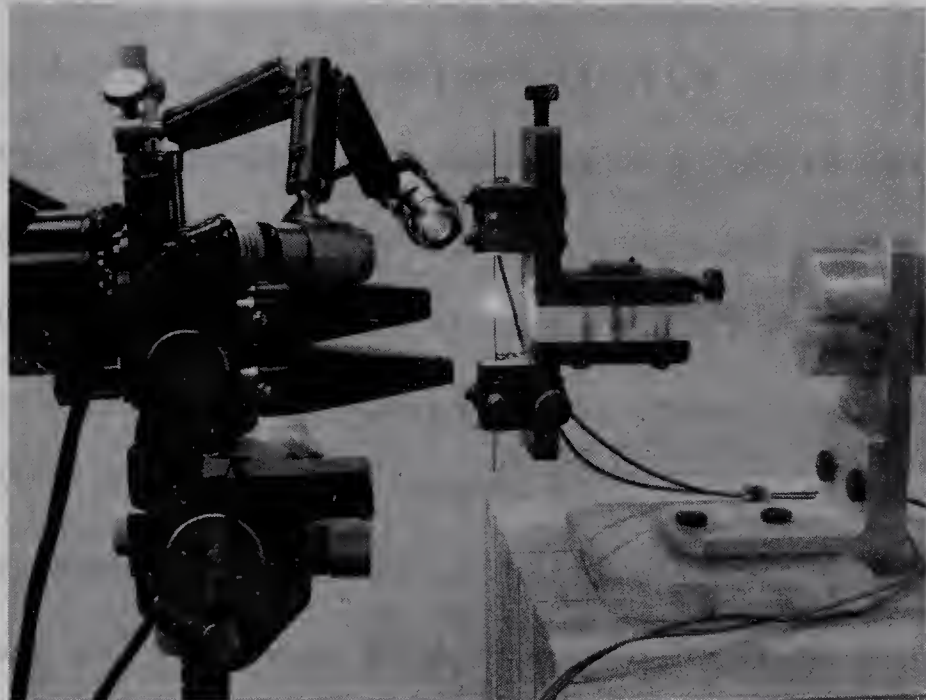


Fig. 2.16 Mechanism for Forming Charging Spheres. Shown is the Needle Adjustment Mechanism, a Discharge and the Observation Microscope.

3. DETECTION OF MICROPARTICLES

3.1 Charge Detection

Charged particles, after having been emitted by the charging mechanism, are sensed as they drift through a series of detectors which are connected to the input of a charge sensitive amplifier. A detector consists of either a drift tube or a charge collection plate that is surrounded by a grounded enclosure with screened openings to permit the passage of charged particles. Diagrams of the two types of detectors that have been constructed and used are shown in Fig. 3.1 and Fig. 3.2.

Consider a particle carrying charge $+q$ and travelling through the detector of Fig. 3.1. While the particle is well within the cylinder marked A, flux lines emanating from the particle terminate on the cylinder's interior surface and induce on it a charge $-q$, thereby generating on the remainder of the detector a charge $+q$. It is this latter charge that is sensed and measured by the charge sensitive amplifier. The growth and decay of this charge, as the particle traverses the detector, is sketched below the detector diagram.

A positive particle that has passed through the screen of the detector of Fig. 3.2, induces on the collection plate B a negative charge whose magnitude increases linearly as the distance between particle and collection plate decreases. The positive charge that is thereby generated on the detector is sketched below the detector diagram.

A schematic diagram of the charge sensitive amplifier that has been constructed and used is shown in Fig. 3.3. C_{in} and R_{in} constitute the input impedance of the amplifier. C_{fb} and R_{fb} constitute the feedback network that renders the amplifier charge sensitive.

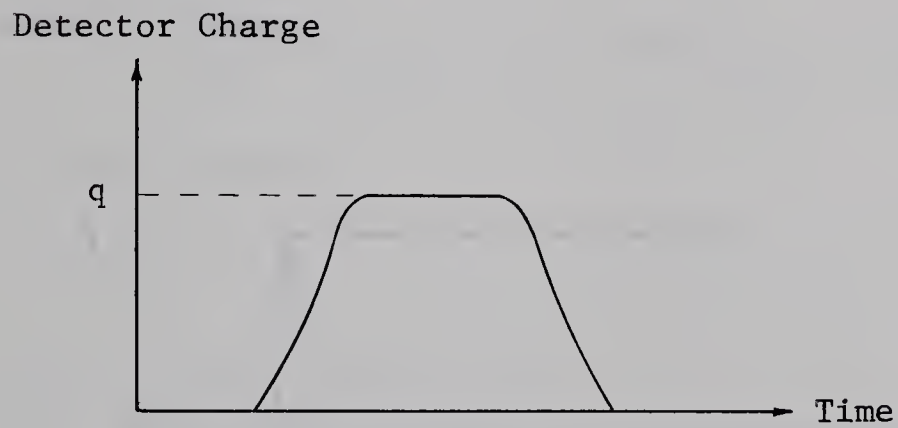
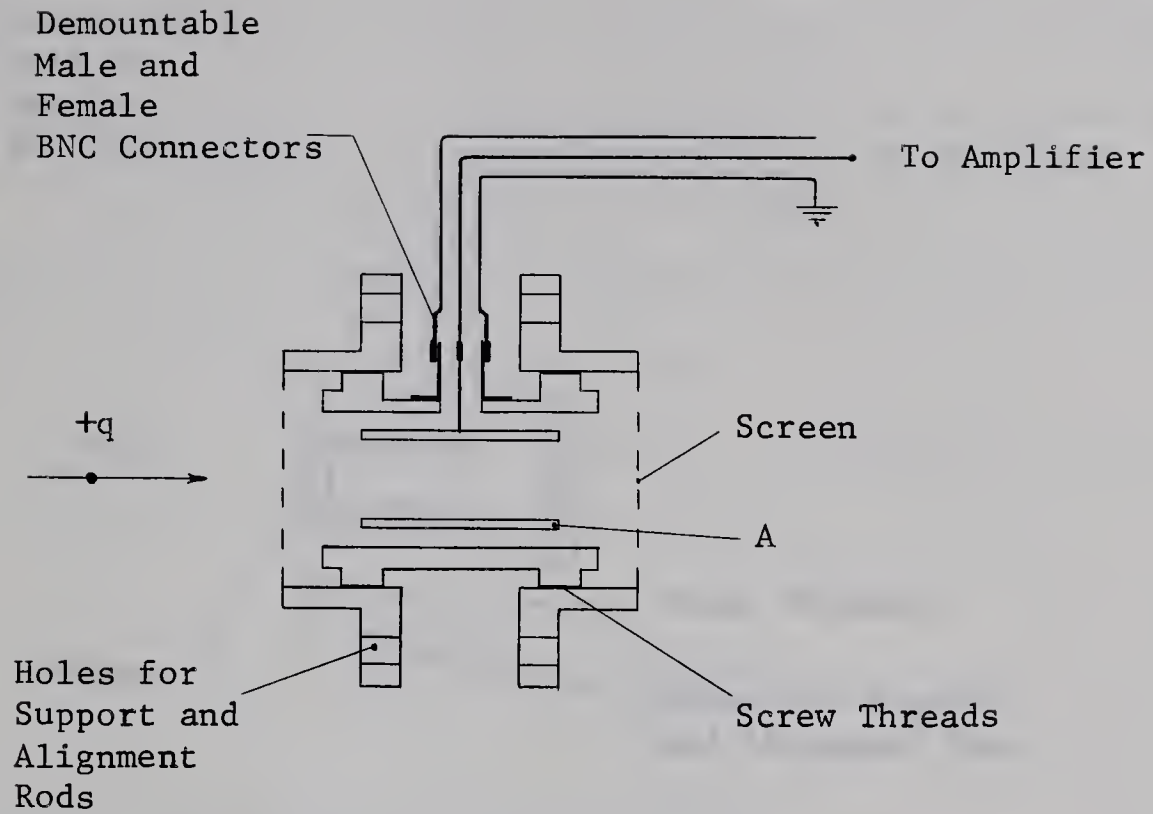


Fig. 3.1 Drift Tube Particle Detector and
Detector Charge versus Time

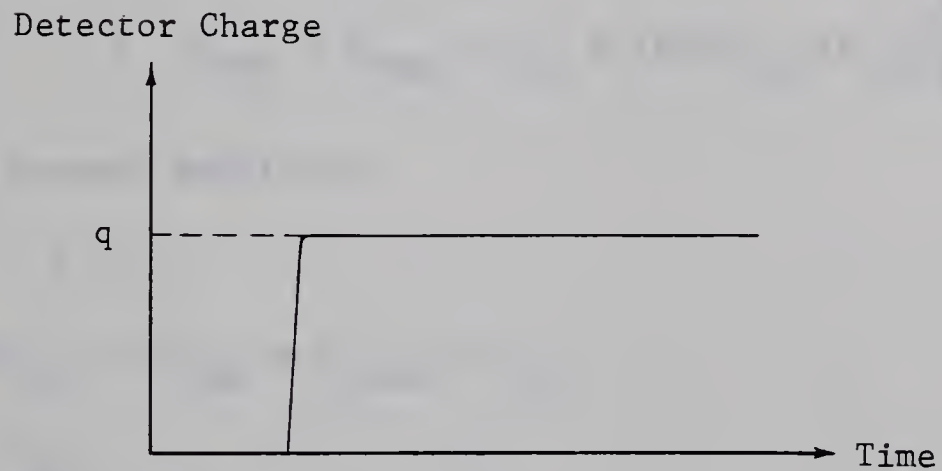
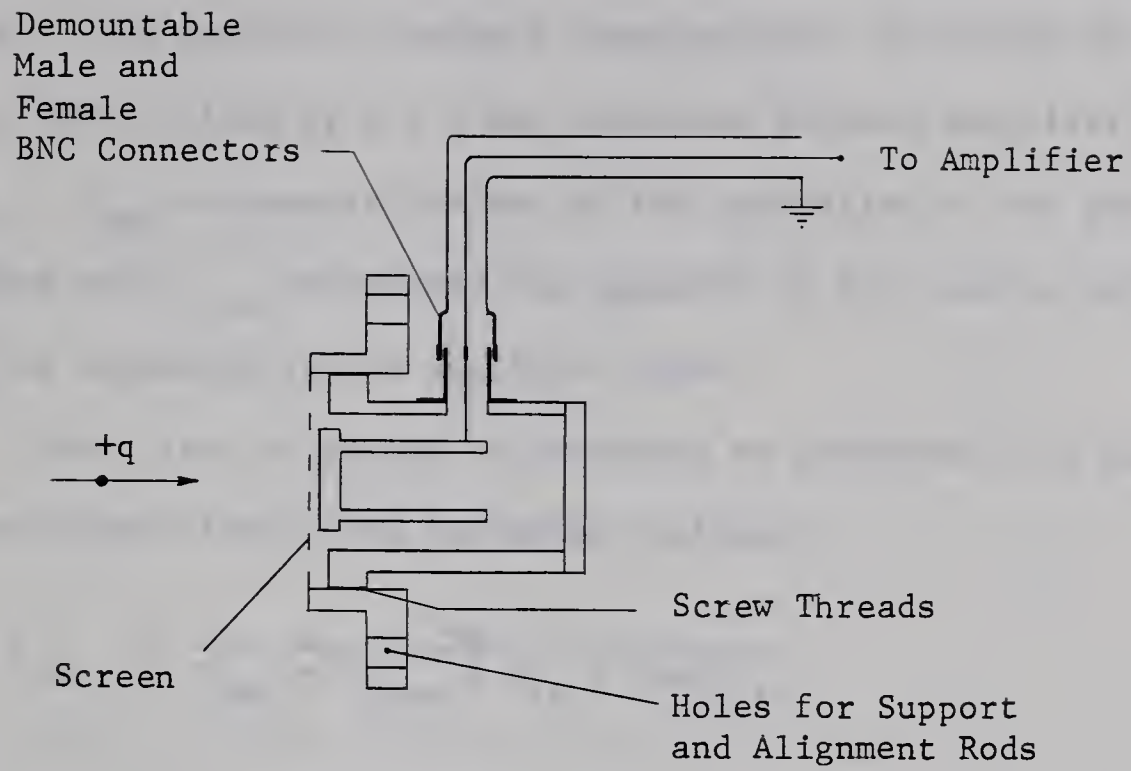


Fig. 3.2 Collection Plate Particle Detector and Detector Charge versus Time

Fig. 3.4 shows the complete equivalent circuit of the charge sensitive amplifier, particle detectors and the amplifier calibrating circuit. The amplifier feedback impedance has, by virtue of the Miller effect, been divided by $A + 1$ and connected between amplifier input and ground. C_{det} represents the sum of the capacities of the particle detectors and C_{line} represents the capacity of the coaxial cable that joins the detectors to the amplifier input.

A unit step of charge of magnitude $+q$ generated by a particle detector gives rise to the following voltages:

$$\begin{aligned} v_{in} &= \frac{+q}{C_{det} + C_{line} + C_{in} + (A+1)C_{fb}} \\ v_{out} &= \frac{-qA}{C_{det} + C_{line} + C_{in} + (A+1)C_{fb}} \end{aligned} \quad \dots(3.1)$$

Both v_{in} and v_{out} decay with a time constant

$$\tau = (C_{det} + C_{line} + C_{in} + (A+1)C_{fb}) \left(R_{in} \parallel \frac{R_{fb}}{A+1} \right) \quad \dots(3.2)$$

For the present amplifier

$$A \gg 1$$

$$(A+1)C_{fb} \gg (C_{det} + C_{line} + C_{in})$$

and $\frac{R_{fb}}{A+1} \ll R_{in}$

Consequently, equations (3.1) and (3.2) can be simplified to:

$$v_{out} = - \frac{q}{C_{fb}} \quad \dots(3.3)$$

and $\tau = C_{fb} R_{fb} \quad \dots(3.4)$

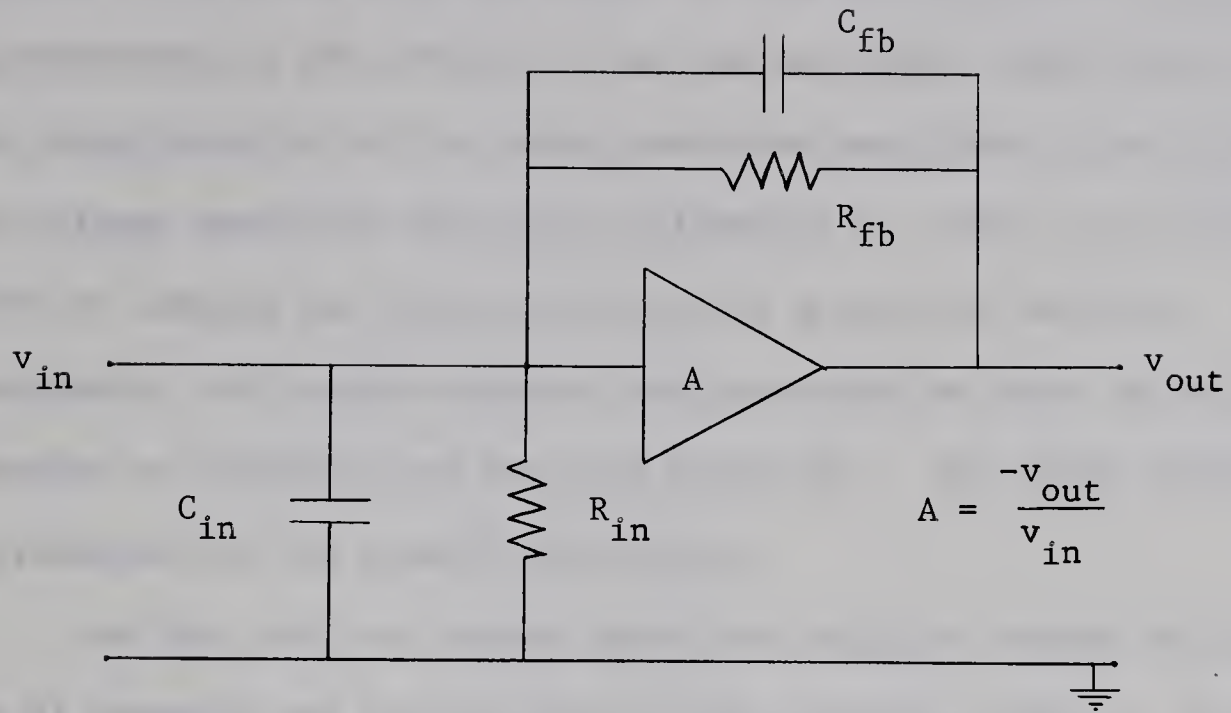


Fig. 3.3 Charge Sensitive Amplifier

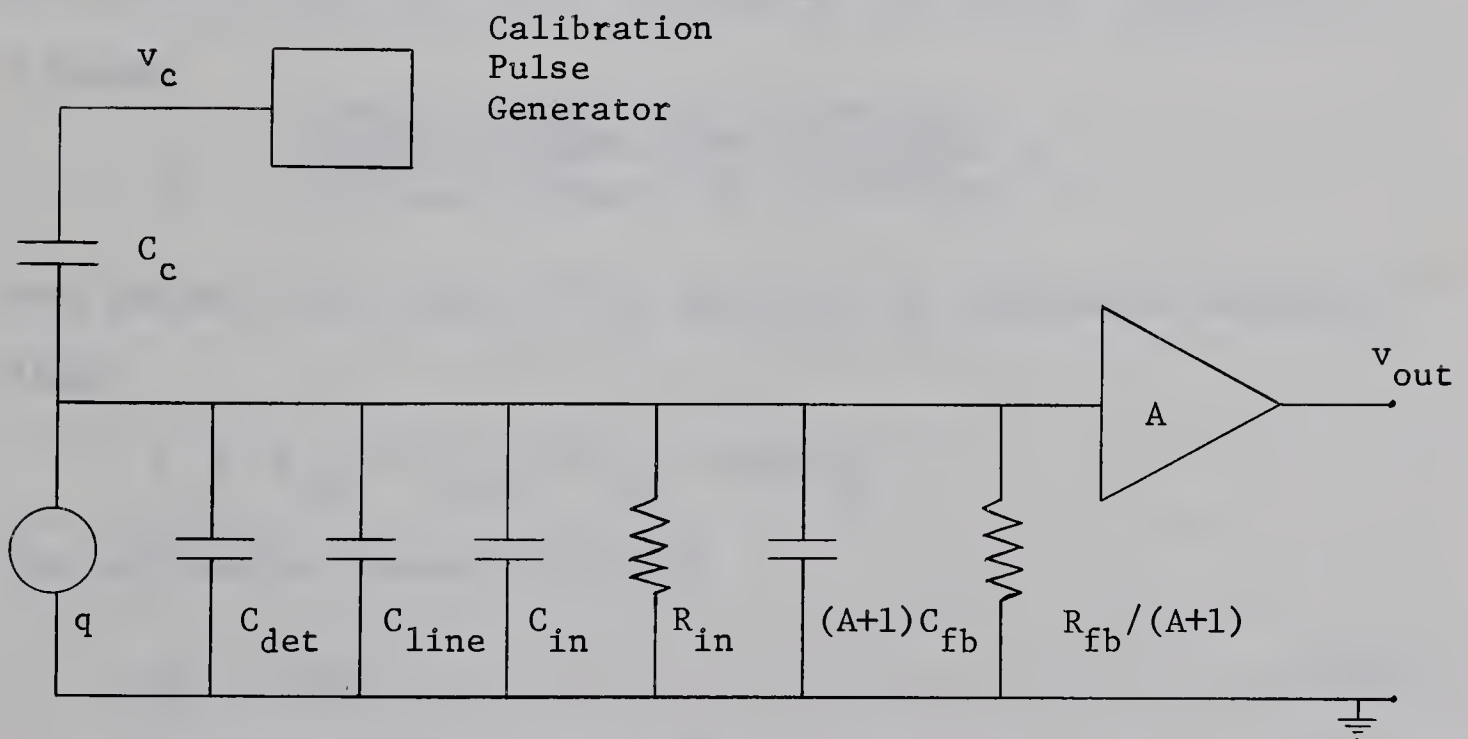


Fig. 3.4 Charge Sensitive Amplifier, Particle Detector and Calibration Circuit

Equation (3.3) shows that the output of the charge sensitive amplifier is independent of the detector, line and amplifier input capacities. This characteristic of the charge sensitive amplifier is not possessed by a voltage sensitive amplifier configuration, which is an alternative method of sensing the charge generated by a particle detector. As a consequence, the charge sensitive configuration has more versatility, is easier to calibrate and has more stability. For these reasons it is preferred for the present application.

The fact that the charge sensitive amplifier output is independent of detector and line capacity is of particular value. It means that a single amplifier can be used with different types and combinations of detectors and with various lengths of interconnecting cables, without the need for constant recalibration.

The initial calibration of the amplifier is performed by applying a known voltage step v_c to the known calibration capacitor C_c .

A charge

$$q_c = \frac{C_c (C_{det} + C_{line} + C_{in} + (A+1)C_{fb})}{C_c + (C_{det} + C_{line} + C_{in} + (A+1)C_{fb})} v_c$$

then passes to the input of the amplifier for calibration purposes.

Since

$$C_c \ll C_{det} + C_{line} + C_{in} + (A+1)C_{fb}$$

the calibration charge is given by

$$q_c = C_c v_c \quad \dots (3.5)$$

The design of the charge sensitive amplifier that has been constructed is that of a low noise nucleonic preamplifier. (A detailed description of the amplifier is found in references (68) and (69).)

A circuit diagram is given in Fig. A.2 in the appendix. The amplifier employs a cascode connected input stage with a bootstrapped plate load, and a cathode follower output stage. The following amplifier parameters are relevant to the present application:

$$A(\text{approx}) = 1700$$

$$C_{in}(\text{approx}) = 25\text{pf}$$

$$R_{fb} = 100 \text{ M}$$

$$C_{fb} = 2.79\text{pf}$$

and

$$\begin{aligned}\tau &= C_{fb} R_{fb} \\ &= 0.28\text{ms}\end{aligned}$$

Thus, from equation (3.3), the particle charge in terms of the amplifier output pulse amplitude and the value of C_{fb} is

$$q = -v_{out} \cdot 2.79\text{pf} \quad \dots(3.6)$$

The combination of detectors that was used for nearly all particle detection experiments is shown in Fig. 3.5. The detectors are joined in parallel and are connected to the input of the charge sensitive amplifier whose output is displayed on an oscilloscope. A typical sequence of amplifier output pulses, corresponding to the passage of a positively charged microparticle through all four detectors, is sketched below the detector diagram. The pulse that is generated as the particle passes through the first detector triggers the horizontal sweep of the oscilloscope. The time separation of the second and third pulses, and the known distance between the corresponding detectors, yield the particle velocity. That is, with reference to Fig. 3.5,

$$v = \frac{\Delta s}{\Delta t} \quad \dots(3.7)$$

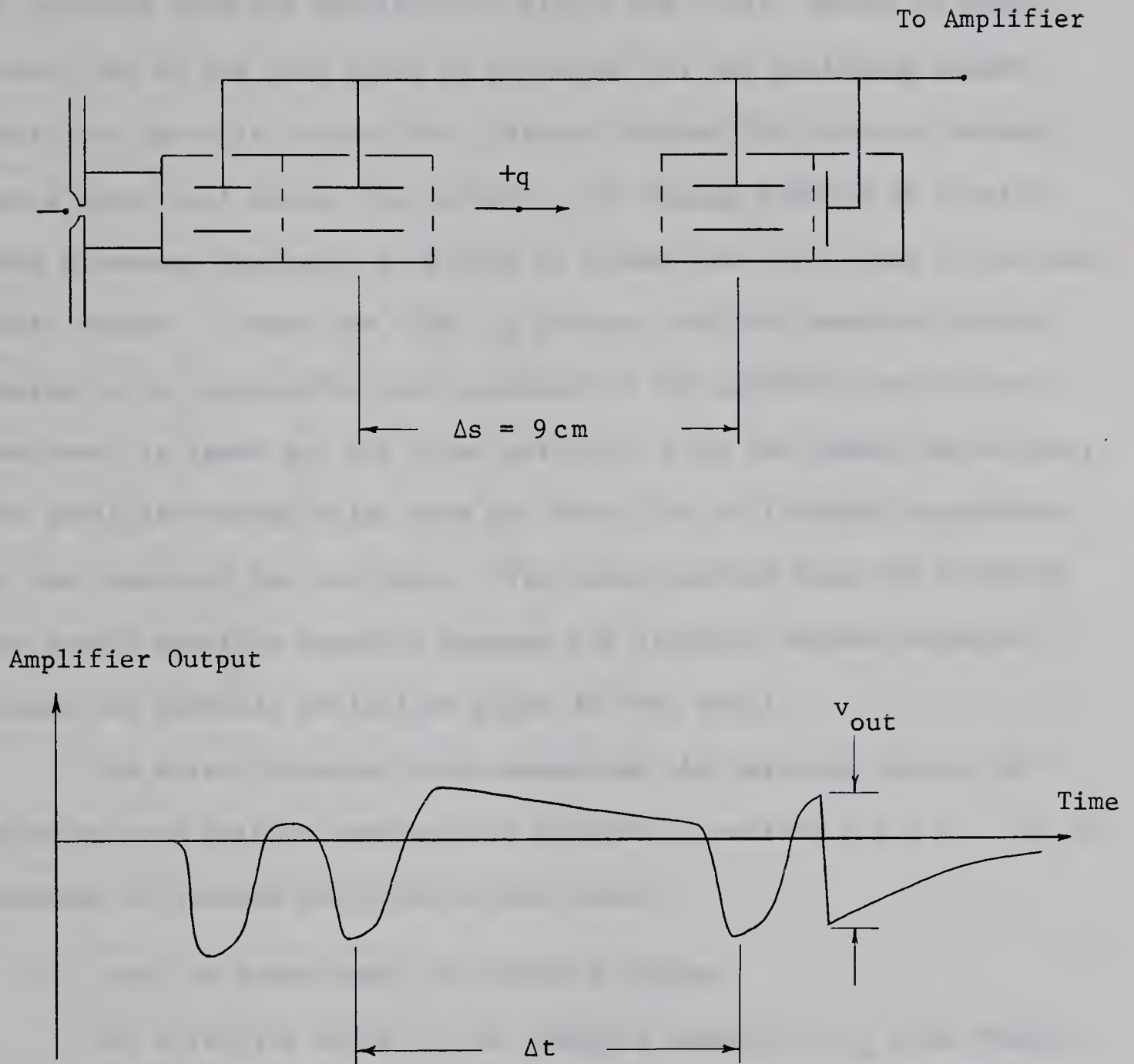


Fig. 3.5 Sketch of Detector Combination and Amplifier Output

The amplitude of the last pulse is used in equation (3.6) to compute the particle charge q . Although, in principle, the charge could also be computed from the amplitude of either the first, second or third pulse, use of the last pulse is preferred for the following reason. While the particle crosses the distance between the detector screen and a point well within the detector, the charge induced on a drift tube increases gradually from zero to almost the full value of the particle charge. Since the time lag between zero and maximum induced charge is not negligible when compared to the amplifier decay time constant, at least not for those particles with the lowest velocities, the amplifier output pulse does not reach the full height appropriate to the charge of the particle. The above problem does not arise in the fourth particle detector because the distance between detector screen and particle collection plate is very small.

The errors incurred while measuring the particle charge and velocity were briefly mentioned in chapter 2, section 2.2.3 C. It is relevant to discuss how these errors arise:

A. Error in measurement of particle charge.

The effective value of the feedback capacitor C_{fb} that renders the amplifier charge sensitive, was obtained by the calibration procedure that is outlined earlier in this chapter. From equations (3.3) and (3.5) the relevant relationship is

$$C_{fb} = - \frac{C_c v_c}{v_{out}}$$

The value of the calibration capacitor C_c was measured on an impedance bridge to within $\pm 3\%$. The sum of the errors in measuring v_c and v_{out}

is estimated to be $\pm 2\%$. The total error in C_{fb} is thus $\pm 5\%$.

The sum of the detector and line capacities varied, depending upon the particular experiment, from about 10pf to 50pf. Substitution of these values and of the amplifier parameters into equation (3.1) shows that for a given charge, use of various combinations of detectors results in output pulse amplitudes that differ by approximately 1%.

The final error in the determination of q is incurred while measuring the output pulse amplitude v_{out} . Due to the presence of amplifier noise, this error is largest for those particles that carry the least charge. For the usual surface field intensities that were established on particles during the course of the experiments, the error is approximately $\pm 10\%$ or more for particles with radii of less than 0.5 microns, and $\pm 3\%$ or less for particles with radii of one micron or larger. Thus, the overall error in the measurement of microparticle charge is dependent upon particle radius and varies from about $\pm 9\%$ for particles with radii larger than one micron, to $\pm 16\%$ or more for particles with radii of 0.5 microns or less.

b. Error in the measurement of particle velocity.

The error in v is primarily determined by the error incurred in the measurement of Δt . With reference to Fig. 3.5, it is seen that Δt is determined by measuring the time interval between two geometrically similar points on the two pulses that are generated as the particle passes through the second and third detectors. The error in this measurement, and hence in the velocity, is estimated to be $\pm 5\%$.

By use of the foregoing techniques, a certain number of charged particles were analyzed. The oscilloscope trace corresponding to

each particle was recorded photographically. Two typical photographs are shown in Figs. 3.6 and 3.7. Fig. 3.6 corresponds to a particle that has traversed the first three detectors and has then been intercepted by the screen that covers the last detector. Fig. 3.7 is the trace of a particle that has traversed all detectors. The analysis of photographs similar to the above has yielded the information that is plotted in Fig. 2.10. The radii of the particles that were detected ranged from about 0.5 to 1.1 microns. The corresponding charge to mass ratios and velocities ranged from 3.2 to 0.85 coulombs/Kg and from 0.32 to 0.16 Km/sec.

Before the contact charging mechanism that has been built can be used as an injector for a microparticle accelerator, the size of the charging sphere must be significantly decreased while the electrode voltage is held constant. As discussed in chapter 2, this is necessary so that the charging process can become more effective and provide particles with higher charge to mass ratios than those that have been attained in the foregoing experiments. For instance, the particle surface field intensities that have been established were in the neighbourhood of 1% of the theoretical field evaporation field intensity. For the foregoing experiments, the charging sphere used was adequate as the particles carried sufficient charge to be reliably detected.

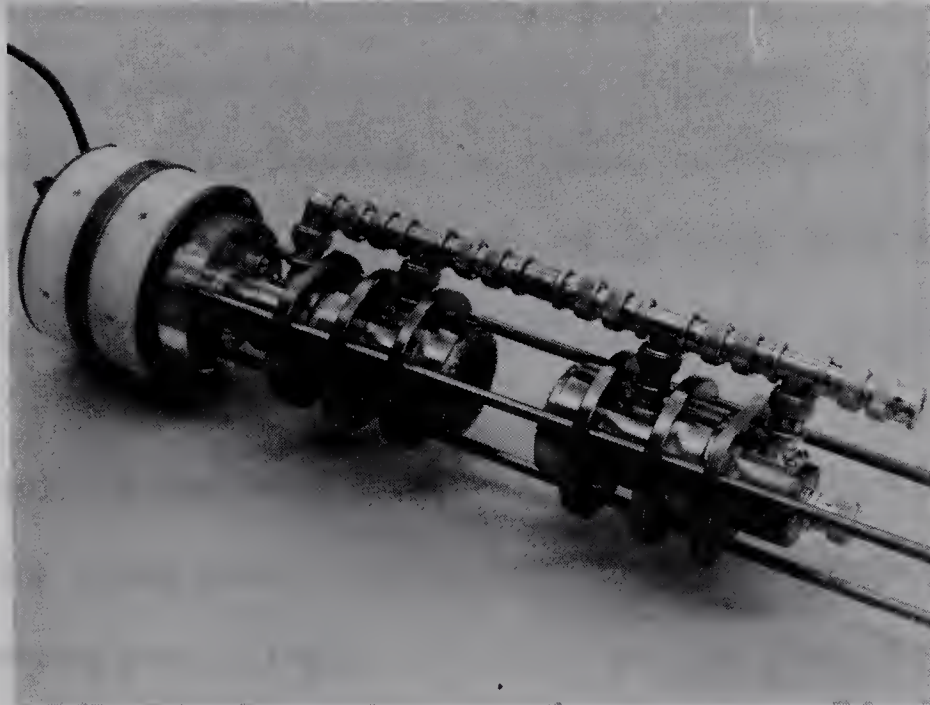


Fig. 3.8 Photographs of Particle Detectors, Alignment Rods and Charging Mechanism.

3.2 Optical Detection

3.2.1 Theoretical Considerations

The optical detection scheme is fully described in a later section. As a basis for the present theoretical considerations, it is sufficient to sketch the general principle of operation. The image of an intense light source is projected into the path of the particle. The particle, while crossing the image, scatters a minute fraction of the available light. This light is detected by a photomultiplier, which, in turn, generates an output pulse that is displayed on an oscilloscope.

It is difficult or impossible to predict the feasibility of an experiment such as the above purely on the basis of theoretical considerations. The reasons are, firstly, that some of the physical parameters of importance to the experiment, such as the reflectivity of the carbonyl iron particles, are not accurately known. Secondly, the success of the experiment ultimately depends upon how it is carried out in practice. This applies in particular to the design and construction of the optical system that images the light source and to the relative location of the photomultiplier. For instance, background flux enters the photomultiplier whether or not a particle is present. This flux must be exceedingly low, otherwise the minute flux that is scattered by the passage of a particle cannot be detected.

In spite of the shortcomings of idealized theoretical calculations, it is important to have some knowledge of the scattering properties of small particles. This can be of help in the planning and

design of the particle detection scheme and can be used to make order of magnitude calculations. For these reasons a brief review of the scattering of light by small particles now follows. The review is limited to those topics that are important to this investigation.

3.2.1.1 Scattering by Small Particles

Consider the situation depicted in Fig. 3.9, where a particle is illuminated by a plane wave that is propagating in the z direction. For the present discussion the plane wave is assumed to be scalar, although the results that are derived are later extended to include the effects of polarization. The functional form of the plane wave is

$$f_o = e^{j(\omega t - \beta z)} \quad \dots (3.8)$$

where

ω = frequency

t = time

and

$j\beta$ = propagation constant.

The power of the plane wave that is incident upon the particle is partially scattered and partially absorbed. Of primary interest to the present study is the scattered wave. In the far field it is spherical and outgoing and its amplitude is inversely proportional to the distance from the particle. Its functional form is

$$f = S(\theta, \phi) \frac{e^{j(\omega t - \beta r)}}{j\beta r} \quad \dots (3.9)$$

where

r = distance from the particle

θ = scattering angle, i.e. the angle between the direction of propagation of the incident wave and the direction of scattering,

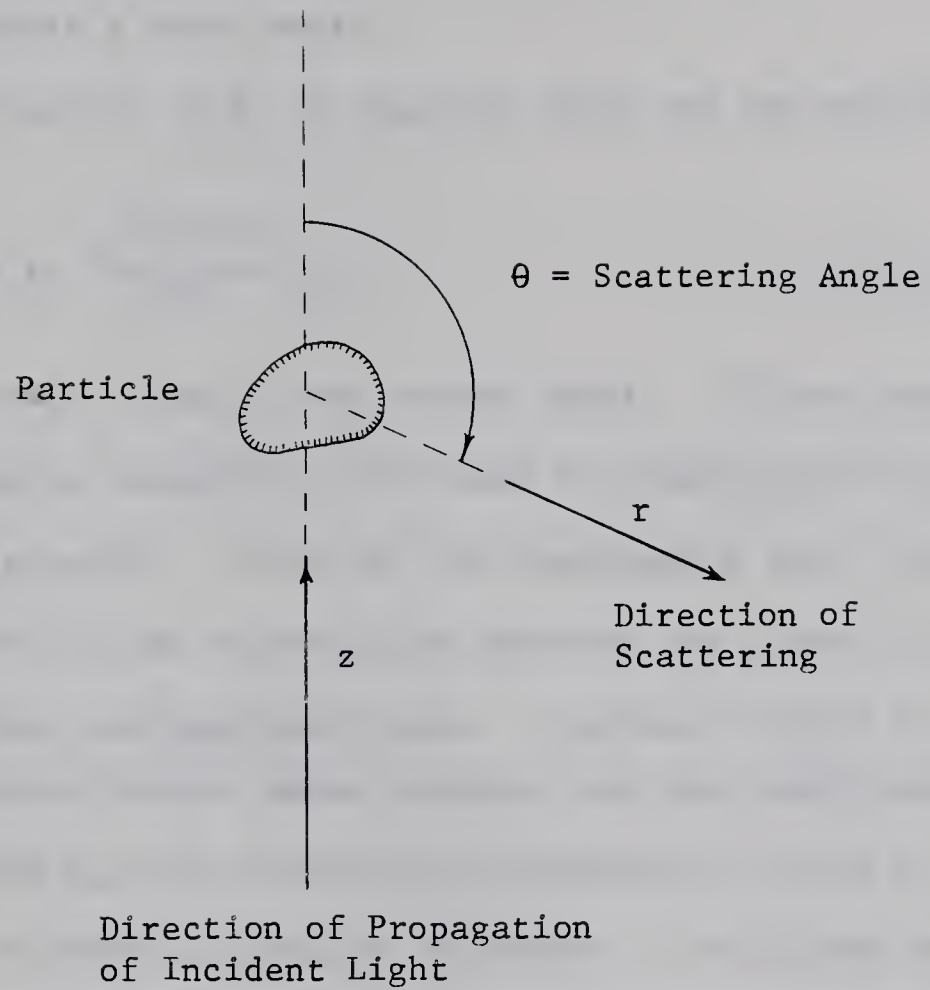


Fig. 3.9 Diagram for the Definition of the Scattering Angle

and ϕ = azimuthal angle of the direction of scattering.

The function $S(\theta, \phi)$ is designated as the amplitude function of the scattering particle. It is generally complex and is a characteristic of the particle, of its orientation with respect to the incident plane wave, and of the latter's wave length.

By use of equation (3.8) in equation (3.9) one can write f as

$$f = S(\theta, \phi) \frac{e^{j(\beta z - \beta r)}}{j\beta r} f_o \quad \dots(3.10)$$

As mentioned previously, f and f_o are scalar waves. If the incident wave is electromagnetic, equation (3.10) must be generalized to include the effects of polarization. That is, the functions f and f_o are replaced by 2-element column vectors that describe the states of polarization of the incident and scattered waves. Further, $S(\theta, \phi)$ is replaced by a scattering matrix whose elements are four amplitude functions, S_1, S_2, S_3 and S_4 , all of which are functions of θ and ϕ . It is also necessary to define a plane of reference. This plane is designated as the plane of scattering and is that plane which contains both the incident beam and the direction of propagation of that part of the scattered beam which is under observation. With these changes, equation (3.10) becomes⁽⁷⁰⁾

$$\begin{bmatrix} E_l \\ E_r \end{bmatrix} = \begin{bmatrix} S_2 & S_3 \\ S_4 & S_1 \end{bmatrix} \frac{e^{j(\beta z - \beta r)}}{j\beta r} \begin{bmatrix} E_{lo} \\ E_{ro} \end{bmatrix}$$

The quantities E refer to the electric intensities of the incident and scattered waves. The subscripts l and r refer to the unit vectors

within and perpendicular to the plane of scattering, such that $\bar{l}_r \times \bar{l}_1$ is in the direction of propagation.

Of practical interest to the present application is the scattering by a spherical homogeneous particle. The remaining discussion will be restricted to this topic. In this case $S_3 = S_4 = 0$ and S_1 and S_2 depend only on θ , i.e.,

$$\begin{aligned} E_r &= S_1(\theta) \frac{e^{j(\beta z - \beta r)}}{j\beta r} E_{ro} \\ E_1 &= S_2(\theta) \frac{e^{j(\beta z - \beta r)}}{j\beta r} E_{1o} \end{aligned}$$

If the intensities of the incident and scattered waves are designated by I_o and I , then for perpendicular polarization (E field perpendicular to plane of scattering)

$$I(\theta, r) = \frac{|S_1(\theta)|^2}{\beta^2 r^2} I_o$$

and for parallel polarization (E field parallel to the plane of scattering)

$$I(\theta, r) = \frac{|S_2(\theta)|^2}{\beta^2 r^2} I_o$$

If the incident wave is natural light, then

$$I(\theta, r) = \frac{|S_1(\theta)|^2 + |S_2(\theta)|^2}{2\beta^2 r^2} I_o \quad \dots(3.11)$$

General analytic expressions for $S_1(\theta)$ and $S_2(\theta)$ in terms of the size and complex refractive index of the sphere, and the wavelength of the incident radiation, may be found by a formal solution of Maxwell's equations in the presence of the appropriate boundary

conditions. The problem is a classical one and is treated in detail by various authors^{(71),(72)}. The solution is readily available, but it is still a major task to compute numerical values* for $S_1(\theta)$ and $S_2(\theta)$. For this reason, reference is made to existing values of amplitude functions, although these do not entirely apply to iron spheres.

Consider Fig. 3.10 which has been reproduced from reference (73) and portrays the scattering by totally reflecting spheres. The moduli of $S_1(\theta)/x$ and $S_2(\theta)/x$ have been plotted as functions of θ for various values of x . The parameter x is the ratio of the circumference of the sphere to the wavelength of the incident light, i.e.,

$$x = \frac{2\pi a}{\lambda}$$

For example, $x = 10$ corresponds to a particle that has a radius of 0.875 microns, illuminated by yellow green light with a wavelength of 550 millimicrons. The intensity of the scattered light as a function of θ can be computed from the moduli of the amplitude functions by use of equation (3.11). Each curve can qualitatively be divided into two parts, i.e. the diffracted light near the forward scattering angles, and the reflected light for the remaining scattering angles. It is relevant to note that the intensity of the reflected light is very

* With regard to the present application, a further complication arises; that is, the spheres that are of interest to this study are iron. Whereas iron can be considered to be almost perfectly reflecting at microwave and infrared frequencies, it absorbs visible light, and, within the latter range, its complex refractive index is a function of wavelength. Thus, since the light source that illuminates the particle is not monochromatic, a complete picture of the scattering by a particle of given size can only be obtained if a range of numerical values for $S_1(\theta)$ and $S_2(\theta)$ are computed for different wavelengths.

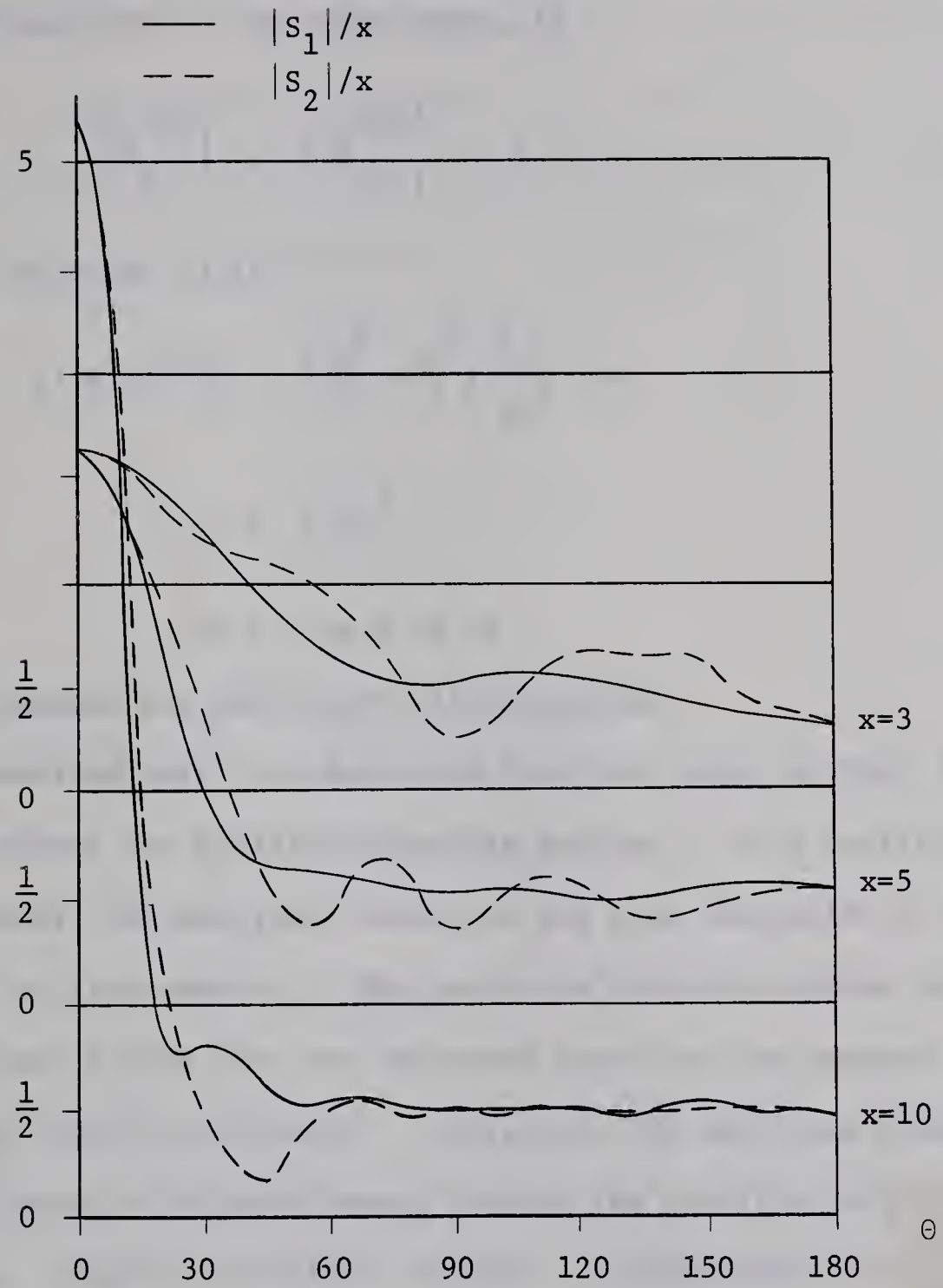


Fig. 3.10 Scattering Diagrams for Totally Reflecting Spheres

nearly equal to the intensity that would occur if the particle were to scatter isotropically the power that is incident upon its geometrical cross sectional area. In other words, if

$$\left| \frac{s_1(\theta)}{x} \right| = \left| \frac{s_2(\theta)}{x} \right| = \frac{1}{2}$$

then, from equation (3.11)

$$\begin{aligned} \int I(\theta, r) r^2 d\omega &= \int \left(\frac{x^2}{4} + \frac{x^2}{4} \right) \frac{I_0}{2\beta^2} d\omega \\ &= I_0 \pi a^2 \end{aligned}$$

where $d\omega = \sin \theta d\theta d\phi$

and the integrals are taken over all directions.

Quantitatively, the amplitude functions shown in Fig. 3.10 are only correct for totally reflecting spheres. In a qualitative sense, however, the amplitude functions are also indicative of the scattering by iron spheres. The reason is that the complex refractive index of iron is such that any refracted wave that has entered the material is rapidly attenuated. Therefore, the amplitude functions are not altered by refracted waves leaving the particle, or by internal resonances. They are modified, however, by absorption and by phase changes that take place at the surface of the metal sphere.

An alternative method of computing amplitude functions is based on geometrical optics. In general, the laws of geometrical optics are only valid for particles whose dimensions are much larger than the wavelength of the incident radiation. However, within the range of complex refractive indices of most metals, the amplitude

functions for all angles θ except near the forward and backward directions, will closely follow those for very large spheres for any x larger than about 3 or 5⁽⁷⁴⁾. This includes the range of particle sizes that are of interest to this study. Consider, thus, the following amplitude functions which have been derived⁽⁷⁵⁾ by using geometrical optics and do not include the light scattered due to diffraction:

$$\begin{aligned} S_1(\theta) &= \frac{jxr_1}{2} e^{2jx \sin \frac{\theta}{2}} \\ S_2(\theta) &= \frac{jxr_2}{2} e^{2jx \sin \frac{\theta}{2}} \end{aligned} \quad \dots(3.12)$$

where

$$\begin{aligned} r_1 &= \frac{\sin \tau - m \sin \tau'}{\sin \tau + m \sin \tau'} \\ r_2 &= \frac{m \sin \tau - \sin \tau'}{m \sin \tau + \sin \tau'} \end{aligned}$$

m = complex refractive index of the sphere

and where the angles τ and τ' are defined in Fig. 3.11.

Thus, if natural light is incident upon a sphere with reflection coefficients r_1 and r_2 , the intensity of the reflected light is, by virtue of equations (3.11) and (3.12)

$$I(\theta, r) = \frac{a^2}{8r} (|r_1|^2 + |r_2|^2) I_o \quad \dots(3.13)$$

Values of $|r_1|^2$ and $|r_2|^2$ as functions of $\cos^2 \tau$ are shown in Fig. 3.12, which is reproduced from reference (76). These values correspond to $m = 1.27 - j1.37$, which is the complex refractive index of

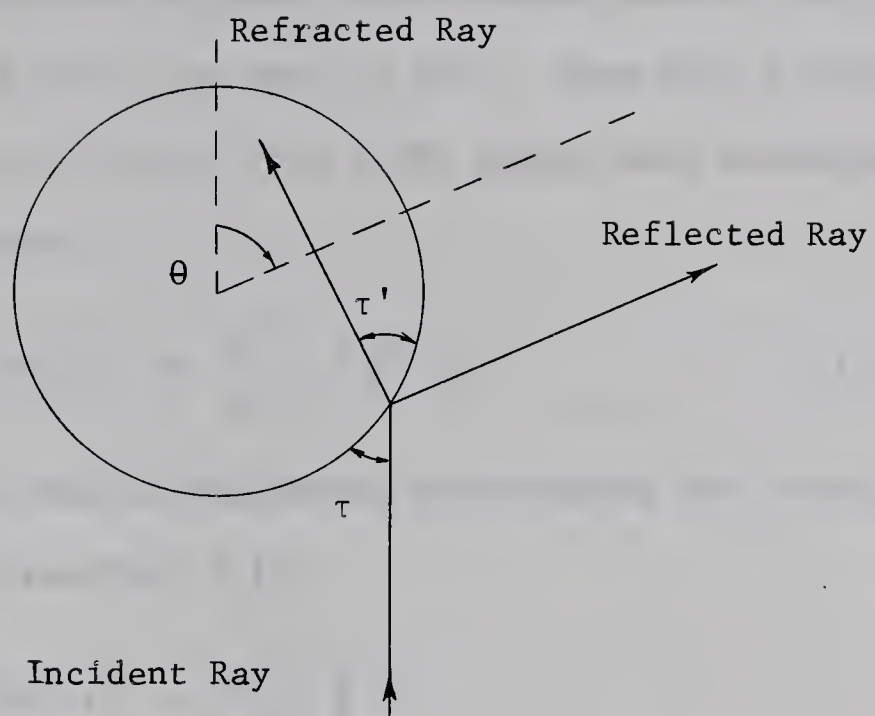


Fig. 3.11 Definition of τ and τ'

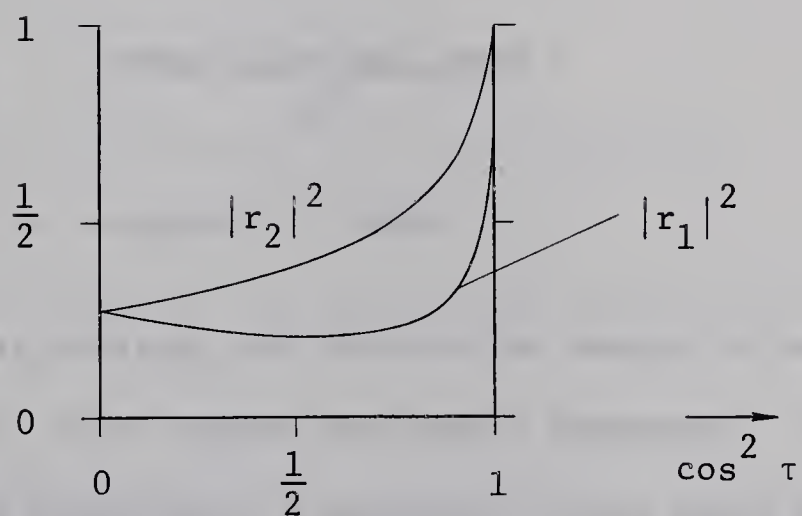


Fig. 3.12 Absolute Values of the Reflection Coefficients for $m = 1.27 - j1.37$

iron⁽⁷⁷⁾ at $\lambda = 440$ millimicrons. Of interest to the present study is the light that is scattered by small iron spheres near $\theta = 90^\circ$, which corresponds to $\tau = 45^\circ$, i.e. $\cos^2 \tau = 1/2$. From Fig. 3.12 the appropriate value of $\{|r_1|^2 + |r_2|^2\}$ is 0.59, which, when substituted into equation (3.13) yields

$$I(90^\circ, r) = \frac{a^2}{r^2} \cdot \frac{0.59}{8} I_o \quad \dots(3.14)$$

For comparison purposes, the corresponding relationship for totally reflecting spheres is, from Fig. 3.10,

$$I(90^\circ, r) = \frac{a^2}{r^2} \cdot \frac{2}{8} I_o$$

3.2.1.2 Radiation Pressure upon Small Particles

An electromagnetic wave carries momentum as well as energy.

The two are related by

$$\frac{\text{momentum}}{\text{unit volume}} = \frac{\text{energy flux/unit area}}{c^2} \quad \dots(3.15)$$

where $c =$ velocity of light

Thus, a particle that scatters and absorbs the energy of an incident electromagnetic wave, also changes the wave's momentum. As a consequence, the particle experiences a mechanical force whose magnitude and direction are equal and opposite to the time rate of change of momentum of the incident electromagnetic wave. This phenomenon is known as radiation pressure.

It is convenient to ascribe to the particle cross sections

for scattering and absorption. These are designated by C_{sca} and C_{abs} and are defined as the geometrical areas, which, when multiplied by the intensity of the incident radiation, give the total power scattered and the total power absorbed by the particle, respectively. Of the momentum removed from the incident radiation, that part corresponding to C_{abs} is not replaced, but a fraction of the part corresponding to C_{sca} is replaced by the forward momentum of the scattered radiation. In other words, the change in momentum of the incident radiation is proportional to

$$C_{abs} + C_{sca} \left(1 - \frac{1}{I_0} \int I(\theta, r) \cos \theta r^2 d\omega\right)$$

$$= C_{abs} + C_{sca} (1 - \overline{\cos \theta})$$

The above quantity is defined as the particle's cross section for radiation pressure and is designated by C_{pr} . It is convenient to introduce a further quantity, Q_{pr} , the efficiency factor for radiation pressure. This quantity is defined by

$$Q_{pr} = \frac{C_{pr}}{(\text{geometrical cross section of particle})}$$

From the definition of C_{pr} and Q_{pr} and from equation (3.15) it follows that

$$\left\{ \begin{array}{l} \text{mechanical force exerted} \\ \text{upon a spherical particle} \end{array} \right\} = \frac{I_0}{c} C_{pr}$$

$$= \frac{I_0}{c} Q_{pr} \pi a^2 \quad \dots (3.16)$$

The direction of the force is in the direction of propagation of the incident radiation.

Values of Q_{pr} for spheres with complex refractive index $m = 1.27 - j1.37$ are quoted in reference (78). As mentioned previously, the above refractive index is valid for iron when the wavelength of the incident radiation is 440 millimicrons. The values of Q_{pr} quoted, monotonically decrease from approximately 2.75 to slightly less than 1.00 for values of x ranging from 1 to infinity. For $x = 14.3$, which at 440 millimicrons corresponds to a particle radius of 1 micron, Q_{pr} is approximately 1.17.

It is of practical interest to determine an upper limit for the radiation pressure that is exerted on a typical microparticle while it traverses the light beam used for its detection. Let it be assumed that the radius of the particle is 1 micron and that the radiant light flux within the beam is 10 watts. For simplicity it is also assumed that the light beam is monochromatic at $\lambda = 440$ millimicrons. If the radiant flux of the beam is concentrated within an area of 1 mm^2 , then from equation (3.16),

mechanical force upon particle

$$\begin{aligned} &= \frac{10 \text{ watts}}{\text{mm}^2} \cdot \frac{1}{c} \cdot 1.17 \cdot \pi \cdot 10^{-12} \text{ meter}^2 \\ &= 1.23 \cdot 10^{-13} \text{ newtons} \end{aligned}$$

The mass of the particle, at a specific gravity of 7.8, is $3.26 \times 10^{-14} \text{ Kg}$. Hence, the particle's acceleration in the direction of propagation of the light beam is

$$\begin{aligned} \text{particle acceleration} &= \text{force/mass} \\ &= 3.77 \text{ meters/second}^2 \\ &= 0.385 \text{ g} \end{aligned}$$

where g is the acceleration due to gravity.

Although the acceleration due to the radiation pressure is significant, there are two reasons why it is too small to be of practical importance:

1. While a microparticle traverses an accelerator it is subjected to gravitation. Hence, any focussing system that is used must be effective enough to correct for a transverse acceleration of one g . Since the geometry of an accelerator is usually cylindrically symmetric about the accelerator axis, the focussing system is equally effective in all transverse directions. Hence, it will be capable of correcting the transverse acceleration due to the radiation pressure.

2. The total time during which a particle is subjected to radiation pressure is very much smaller than the time during which it is subjected to gravitation.

3.2.2 Experimental Work

3.2.2.1 Description of the Experimental Equipment

The optical detection system that has been constructed is shown in Fig. 3.13. Particles are emitted by the charging mechanism, and those whose trajectories are sufficiently well aligned pass through the complete system of apertures and detectors shown. While traversing the image of the light source, a particle scatters sufficient light into the photomultiplier tube to cause its activation. The outputs from the photomultiplier and from the auxiliary charge sensitive detectors are monitored and displayed on an oscilloscope.

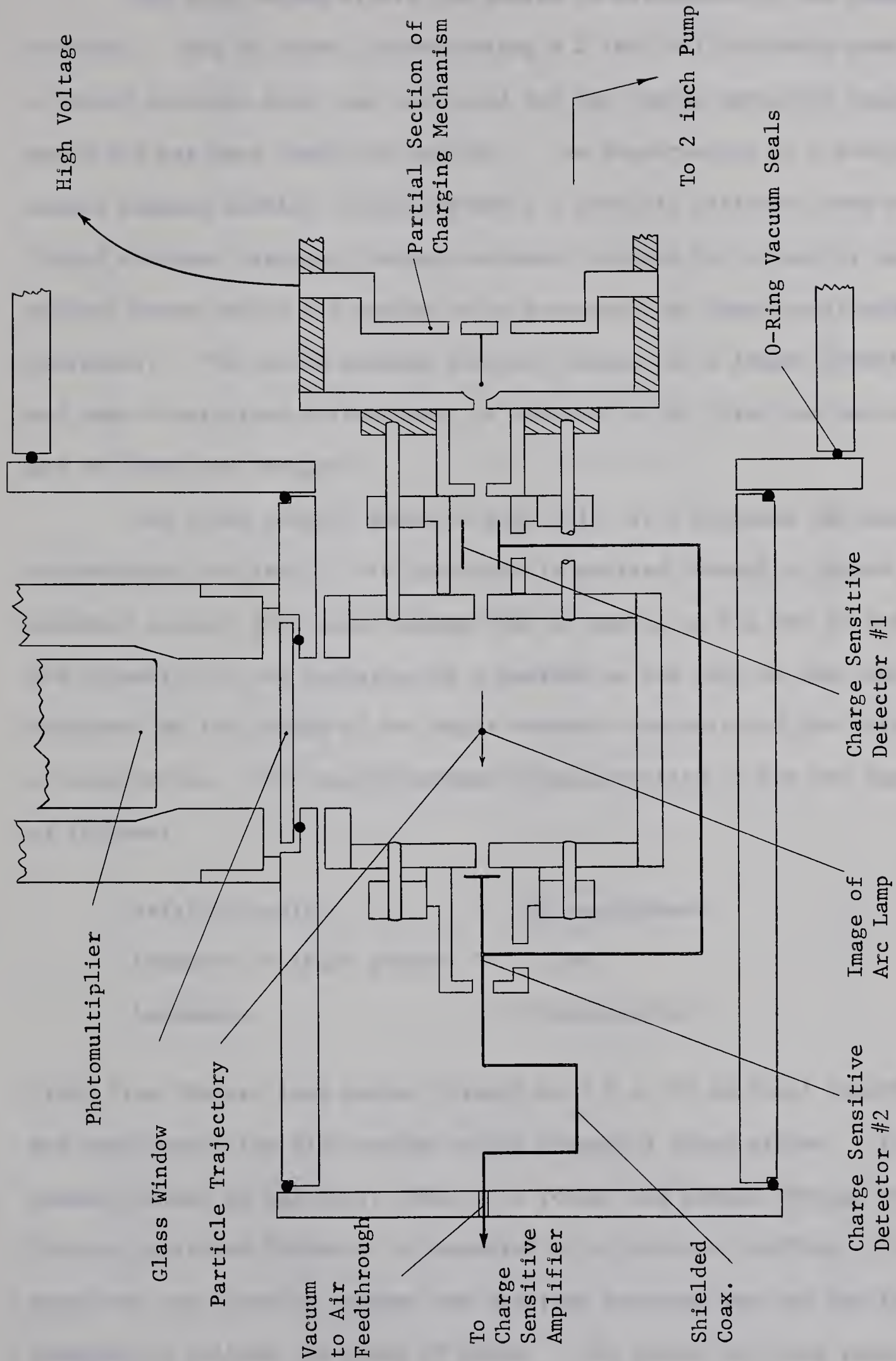


Fig. 3.13 Diagram of the Essential Components of the Optical Detection Scheme (View 1)

The high vacuum within the system is maintained by two pumping stations. One of these, incorporating a 2 inch oil diffusion pump and a liquid nitrogen trap, was also used for the charge detection experiments and has been described earlier. The construction of a complete second pumping station, incorporating a 6 inch oil diffusion pump and liquid nitrogen trapping, became necessary because the volume of and surface areas within the region to be evacuated had been considerably increased. The second pumping station, except for a larger capacity and some other minor differences, is similar to the first one and need not be described further.

The light source, shown in Fig. 3.14, is a Sylvania 100 watt concentrated arc lamp. Its radiation is emitted through a ground and polished optical flat glass window that is sealed to the end of the bulb. The intensity of the radiation is a maximum on the axis of the lamp and decreases as the cosine of the angle between this axis and the direction of observation. The quoted average characteristics of the arc lamp are as follows:

Axial intensity	= 100 candlepower
Diameter of light source	= 1.8 mm
Luminance	= 39 candles/mm ²

Light from the arc lamp passes through an f 1.4, 55 mm focal length lens and then enters the high vacuum region through a glass window. It then passes through an aperture, comes to a focus, and passes through three further apertures before it is absorbed by a system of baffles. All apertures are circular, except the one that precedes and the one that immediately follows the point of focus. The latter two have razor

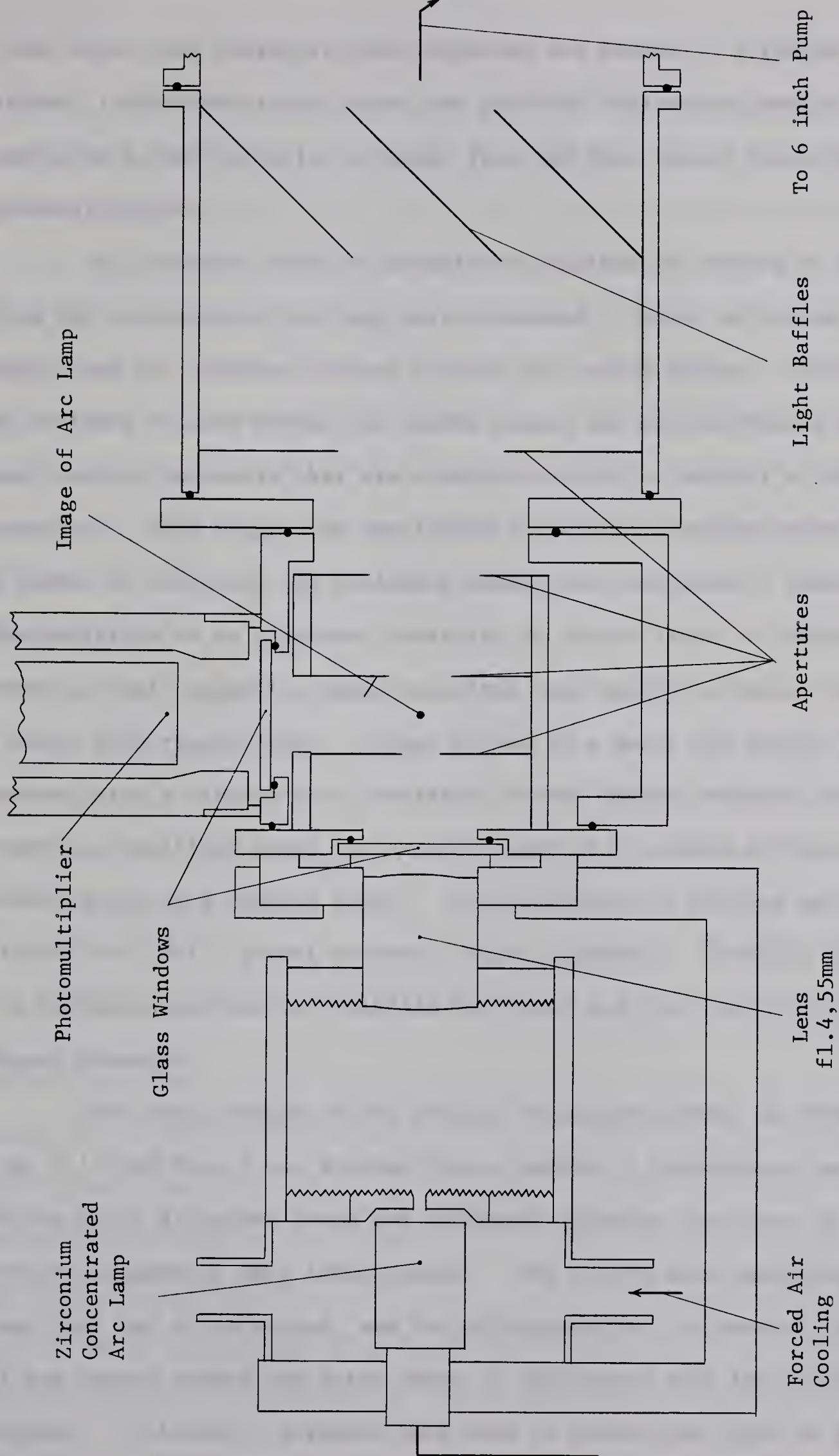


Fig. 3.14 Diagram of the Essential Components of the Optical Detection Scheme (View 2)

blade edges, and therefore their openings are square. A further glass window, located vertically above the particle trajectory, permits the light scattered by the particle to escape from the high vacuum region into the photomultiplier.

All surfaces that are directly or indirectly exposed to the light from the concentrated arc lamp were blackened. This, of course, was a minor task for surfaces located outside the vacuum region. Blackening of surfaces located within the vacuum region was more difficult because most coating materials that are otherwise suitable, exhibit a high vapour pressure. This makes them unsuitable for use in a vacuum system. After a number of failures, the following method was developed. Almost all the materials to be blackened consisted of either brass or aluminium. Prior to their assembly, these materials were etched in chromic and hydrofluoric acid respectively. Then, by use of a small air brush, they were sprayed with a mixture that consisted of very finely powdered activated charcoal, distilled water and a small quantity of sodium silicate. The latter acted as a binding agent. This technique of etching and spraying yielded very dull, almost perfectly black surfaces. Further, once dried, the surfaces contained no volatile materials and thus had a very low vapour pressure.

The final design of the optical detection system, as shown in Fig. 3.13 and Fig. 3.14, evolved from a number of preliminary experiments during which different forms and different relative locations of the various components were investigated. One of the most persistent problems that had to be solved, was the elimination of the beam of light once it had passed beyond the point where it intersects with the particle trajectory. Initially, attempts were made to absorb the light by a system

of baffles, once it had left the high vacuum region through a glass window. This scheme would not have increased the volume and surface area of the region to be evacuated, (as opposed to the scheme adopted in Fig. 3.14), and thus would have required smaller pumping facilities. It was found, however, that reflections from the glass exit window increased the background level of light sufficiently to make the scheme unsuitable for practical use. This problem persisted, even when the light from the arc lamp was polarized prior to entering the high vacuum region, and when the exit window was placed at the Brewster angle.

The photomultiplier that is used is a Philips model 150 AVP 02 with a semi-transparent photocathode and with the following pertinent characteristics:

Diameter of photocathode	= 32 mm
Wavelength at maximum response	= 420 ± 30 millimicrons
Number of stages	= 10
Gain at overall voltage of 1800 volts	= $2 \cdot 10^7$
Anode sensitivity at overall voltage of 1800 volts	= avg. 1250 amps/lumen
Anode dark current at overall voltage of 1800 volts	= avg. $0.2 \cdot 10^{-6}$ amps

The average anode sensitivity and average dark current quoted above are valid for an interdynode voltage of 160 volts and a voltage between the first dynode and photocathode of 240 volts. A circuit diagram of the photomultiplier and of the signal output circuit is shown in Fig. 3.15. The anode voltage used was 1700 volts. If it is assumed that the secondary emission coefficient of each dynode is proportional to the interdynode voltage, then the average anode sensitivity of the configuration

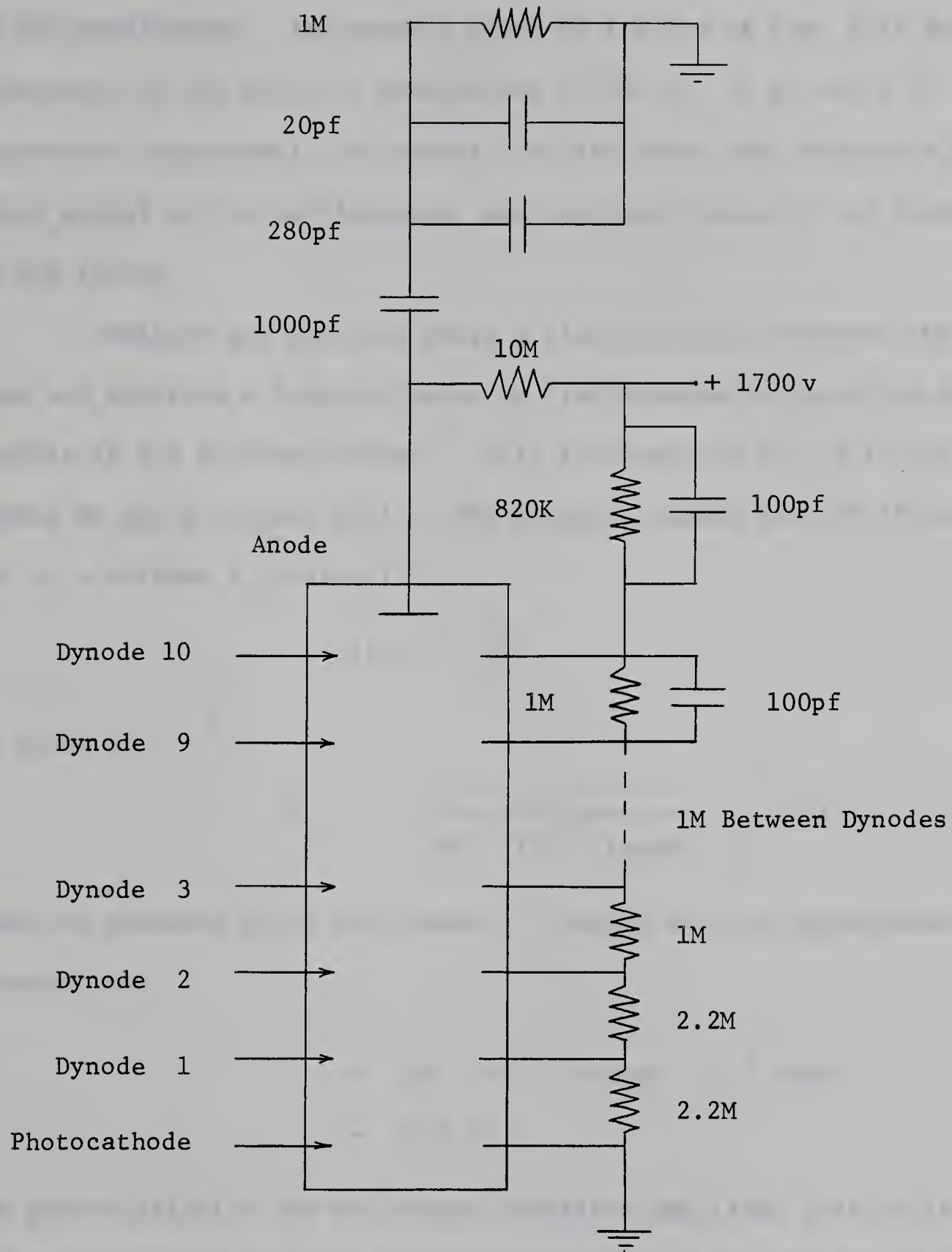


Fig. 3.15 Schematic Diagram of Photomultiplier and Output Circuit

shown in Fig. 3.15, is approximately one third of that quoted above, or 420 amps/lumen. The network shown at the top of Fig. 3.15 and consisting of the parallel combination of 280 pf, 20 pf and 1 M, represents respectively the capacity of the cable that transmits the anode signal to the oscilloscope, and the input capacity and resistance of the latter.

Consider now the case where a microparticle traverses the light beam and scatters a luminous pulse of time duration δt into the photocathode of the photomultiplier. With reference to Fig. 3.16, this causes an anode current $i(t)$. The current charges the 300 pf capacitor to a voltage V_c , which if

$$i(t) \gg \frac{V_c}{IM}$$

is given by

$$V_c = - \frac{1}{300 \cdot 10^{-12} \text{ farads}} \int_0^{\delta t} i(t) dt \quad \dots (3.17)$$

When the luminous pulse has ceased, V_c decays with an approximate time constant of

$$\begin{aligned} \tau &= 300 \cdot 10^{-12} \text{ farads} \cdot 10^6 \text{ ohms} \\ &= 0.30 \text{ ms} \end{aligned}$$

The photomultiplier and the charge sensitive amplifier that monitors the two auxiliary particle detectors (see Fig. 3.13), feed into two separate channels of a dual channel oscilloscope. Both channels have a single time base which is triggered by the first signal from the charge sensitive amplifier. The oscilloscope display that is generated by the passage of a particle thus appears as sketched in Fig. 3.17.

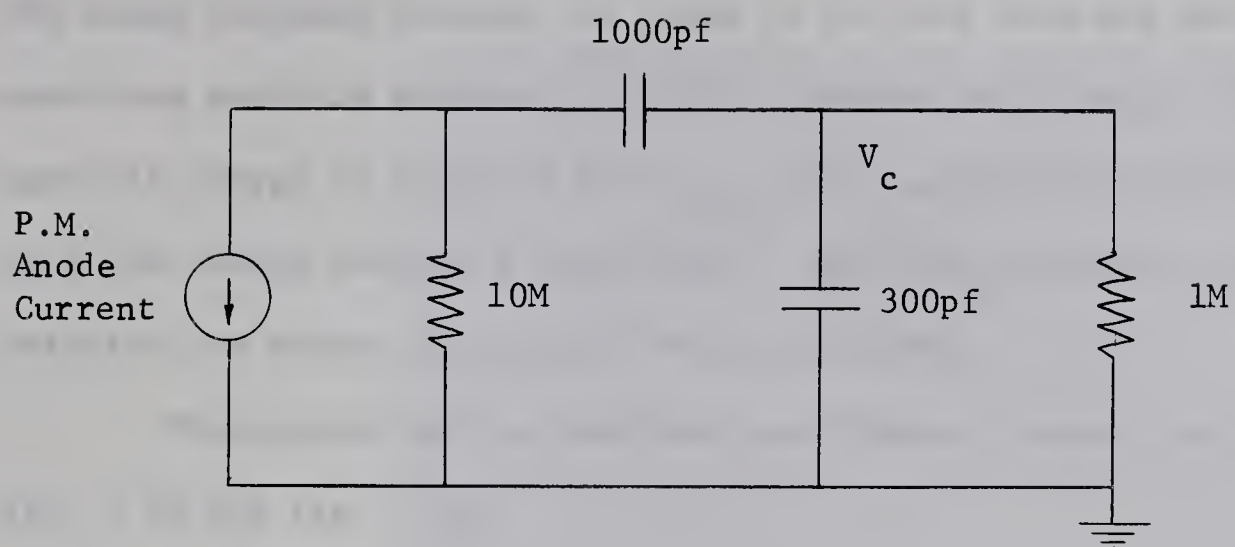


Fig. 3.16 A-C Equivalent Circuit

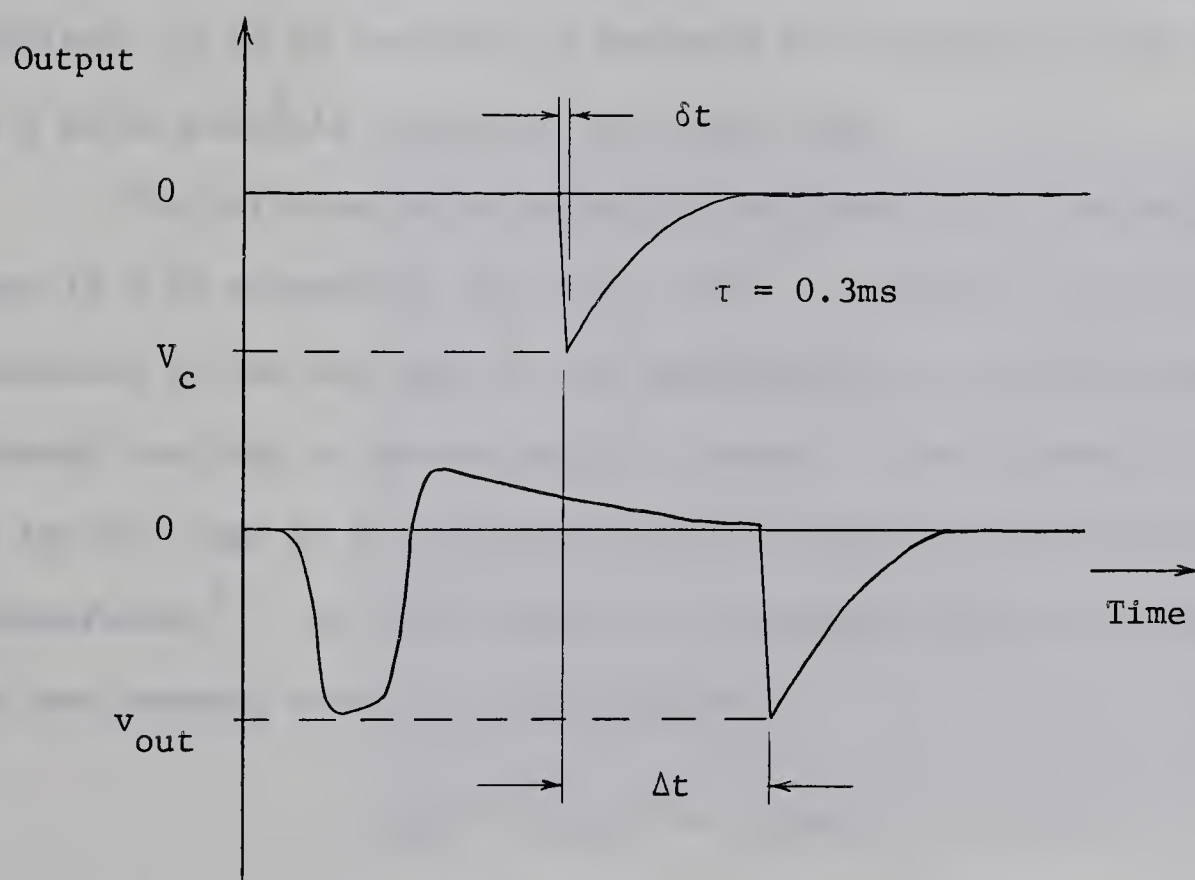


Fig. 3.17 Sketch of Output from Photomultiplier (Top Trace), and Charge Sensitive Amplifier (Bottom Trace).

The particle velocity can be computed from the time interval Δt and the known distance between the image of the arc lamp and the final auxiliary particle detector. (This distance is 4.6 cm.) The particle charge is computed from v_{out} , the amplitude of the final pulse from the charge sensitive amplifier. Once the particle's charge and velocity are known, its radius can be computed.

Photographs of the complete experimental system are shown in Fig. 3.18 and Fig. 3.19.

3.2.2.2 An Estimate of the Photomultiplier Signal

Prior to discussing the experimental results that have been obtained, it is of interest to estimate the voltage V_c that should occur as a given particle traverses the light beam.

The solid angle subtended by the lens at the concentrated arc lamp is 0.05 steradians (see Fig. 3.14). Therefore, since the axial intensity of the arc lamp is 100 candlepower, the luminous flux passing through the lens is approximately 5 lumens. The diameter of the image of the arc lamp is 1.5 mm, and thus its average illumination is $2.8 \cdot 10^6$ lumens/meter². If, with regard to the scattering by a microparticle, one now assumes that at all wavelengths

$$|r_1|^2 + |r_2|^2 = 0.59 ,$$

(which it will be recalled, is the appropriate relationship for $\lambda = 440$ millimicrons), then it follows from equation (3.14) that the illumination of the photomultiplier photocathode is

$$I(90^\circ, r) = \frac{a^2}{r^2} \left(\frac{0.59}{8} \right) (2.8 \cdot 10^6) \frac{\text{lumen}}{\text{meter}^2}$$

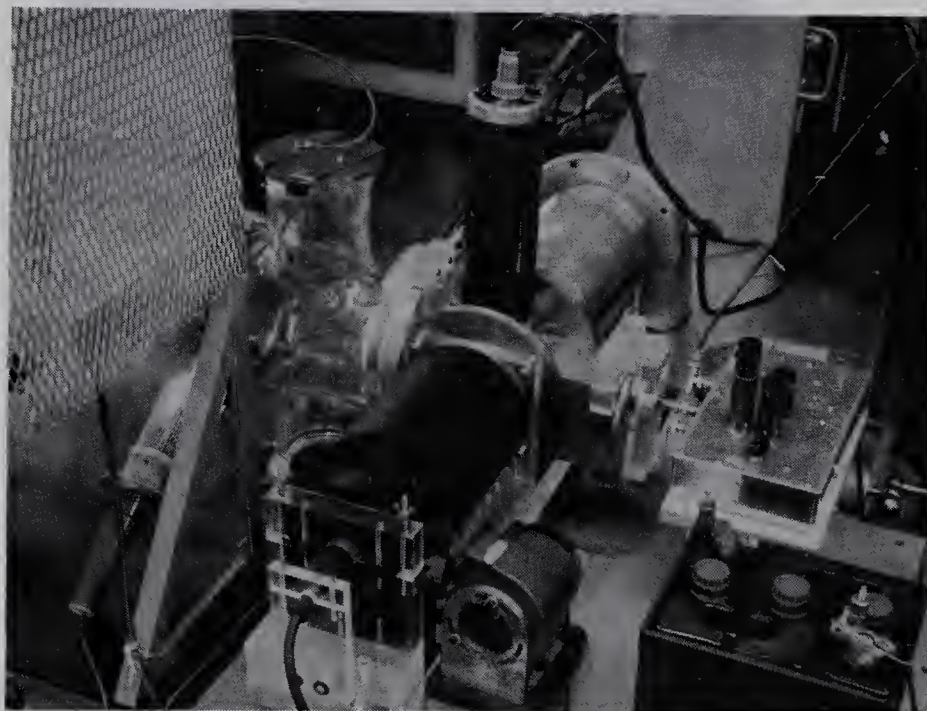
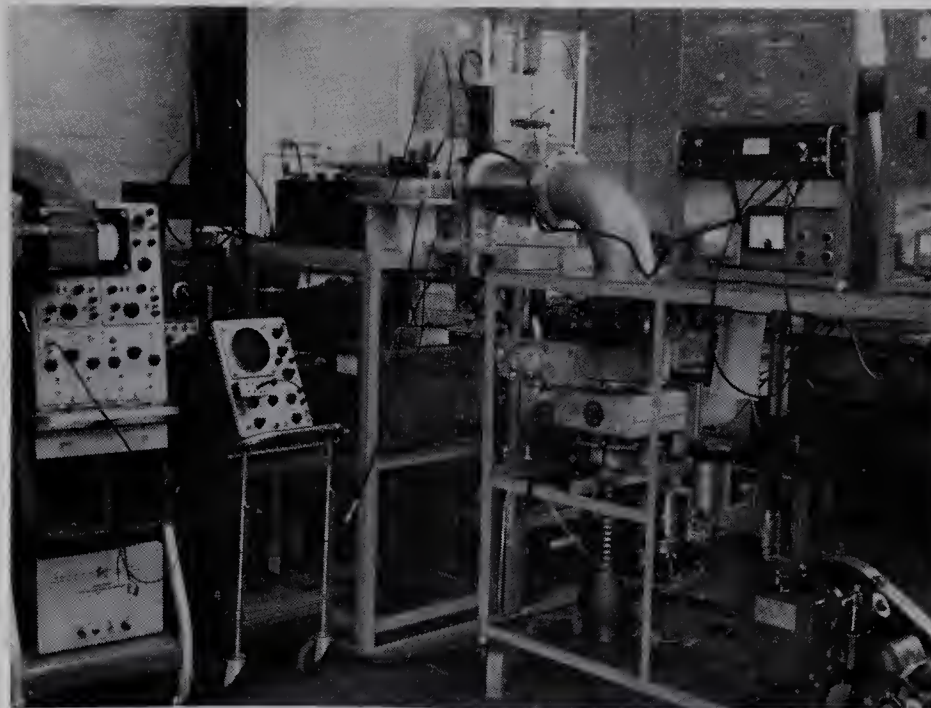


Fig. 3.18 Experimental System for Optical Detection of Microparticles.

Upper Photograph: Front View

Lower Photograph: Top View

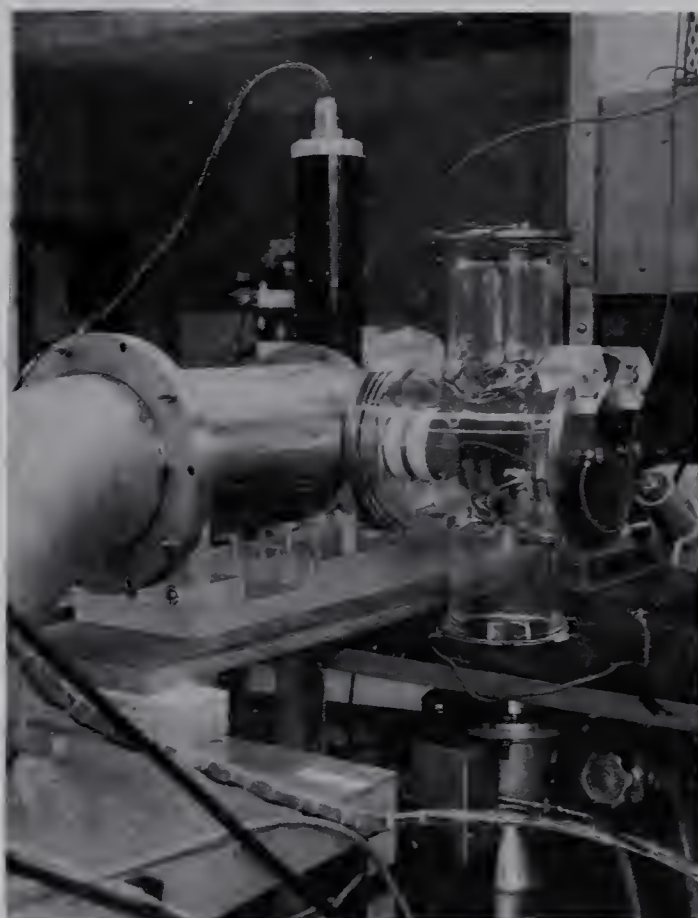


Fig. 3.19 Experimental System for Optical Detection of Microparticles (Rear View).

Since the solid angle subtended by the photocathode at the image of the arc lamp is 0.14 steradians, the luminous flux entering the photomultiplier is

$$\begin{aligned}\phi &= a^2 \left(\frac{0.59}{8} \right) (2.8 \cdot 10^6) (0.14) \text{ lumen} \\ &= 29 \cdot 10^3 a^2 \text{ lumen}\end{aligned}$$

where the units of a are meters.

If the total transmission factor of the lens and the two glass windows is taken to be 50%, then the foregoing equation becomes

$$\phi = 14.5 \cdot 10^3 a^2 \text{ lumen}$$

The anode sensitivity of the photomultiplier has been estimated previously to be 420 amps/lumen. Thus, if one neglects a possible difference in colour temperature between the light source used in this experiment and the light source with which the sensitivity of the photomultiplier has been measured, then the anode current that flows while a particle traverses the light beam is given by

$$\begin{aligned}i(t) &= \phi \cdot 420 \text{ amps} \\ &= 6.1 \cdot 10^6 a^2 \text{ amps}\end{aligned}$$

The time interval δt during which the current flows is inversely proportional to the particle's velocity. Since the diameter of the image of the arc lamp is 1.5 mm,

$$\delta t = \frac{1.5 \cdot 10^{-6}}{v} \text{ sec}$$

where the units of v are Km/sec.

Thus, from the above and from equation (3.17), V_c is given approximately by

$$V_c = - \frac{(6.1 \cdot 10^6 a^2)(1.5 \cdot 10^{-6})}{(300 \cdot 10^{-12})v} \text{ volts}$$

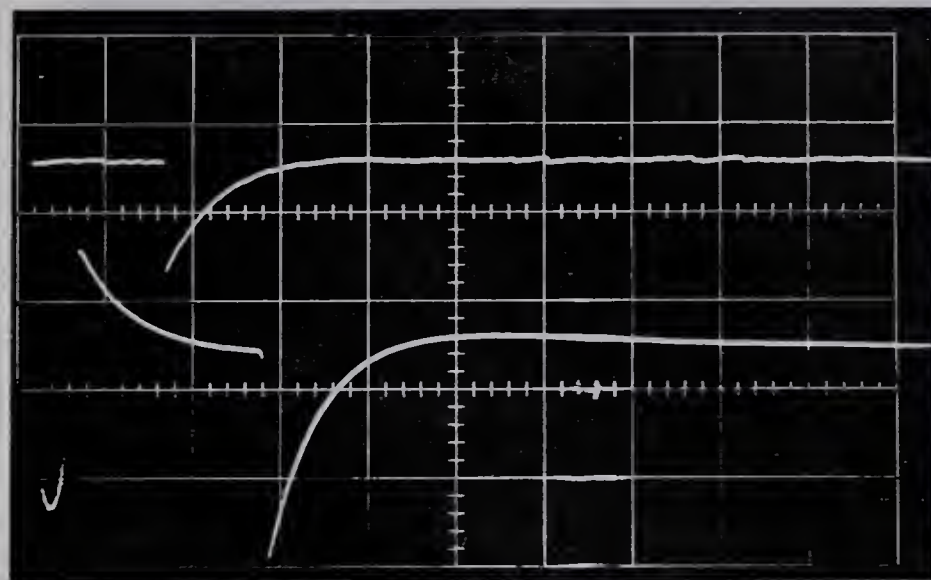
or,

$$V_c (\text{in volts}) = \frac{(-30.5 \cdot 10^{-3})(\text{particle radius in microns})^2}{(\text{particle velocity in Km/sec})} \dots (3.18)$$

3.2.2.3 Experimental Results

Figs. 3.20, 3.21, 3.22, and 3.23 show typical oscilloscope displays. The particles that were detected ranged in radius from approximately 2 microns to 5 microns. Fig. 3.23 corresponds to a particle that has traversed the first charge sensitive detector and, somewhat off centre, the image of the light source. This particle's trajectory was not well enough aligned to pass through the particle aperture which immediately precedes the second charge sensitive detector. On the average, about one in ten of the particles that traversed the first detector also passed through the image of the light source and through the last detector. This was expected, since the solid angle that is subtended at the charging sphere by the particle aperture that immediately precedes the last detector, is about one tenth of the solid angle that is subtended at the charging sphere by the aperture which immediately precedes the first detector.

Particles with similar radii generally produced photomultiplier signals of similar amplitudes V_c . An exception to this was noted during the final experiment which was conducted after the optical detection system had been temporarily modified for another purpose, and



Top Trace: 1 v/cm

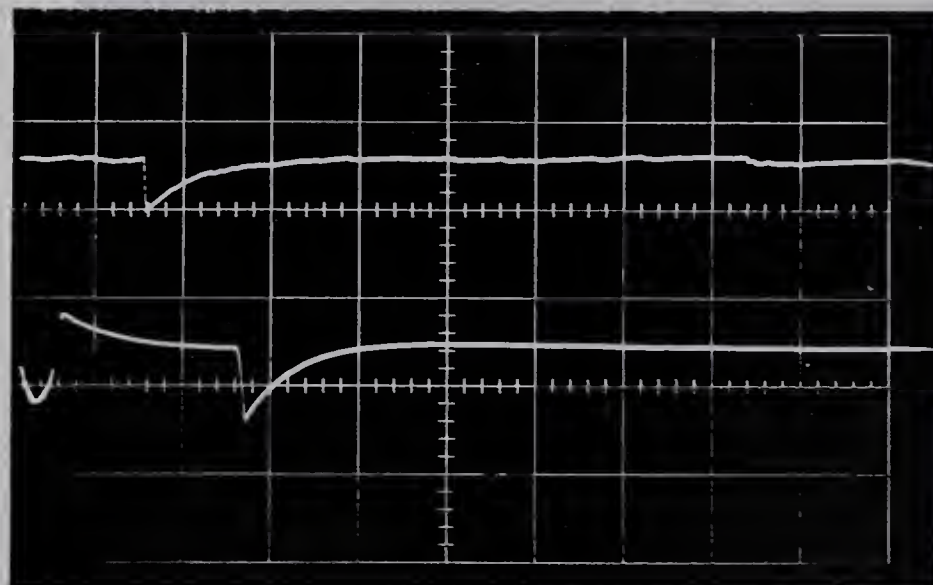
Bottom Trace: 0.1 v/cm

Time Scale: 0.5 ms/cm

$V = 20 \text{ Kv}$

$a = 5.2 \text{ microns}$

$v = 0.077 \text{ Km/sec}$



Top Trace: 1 v/cm

Bottom Trace: 0.1 v/cm

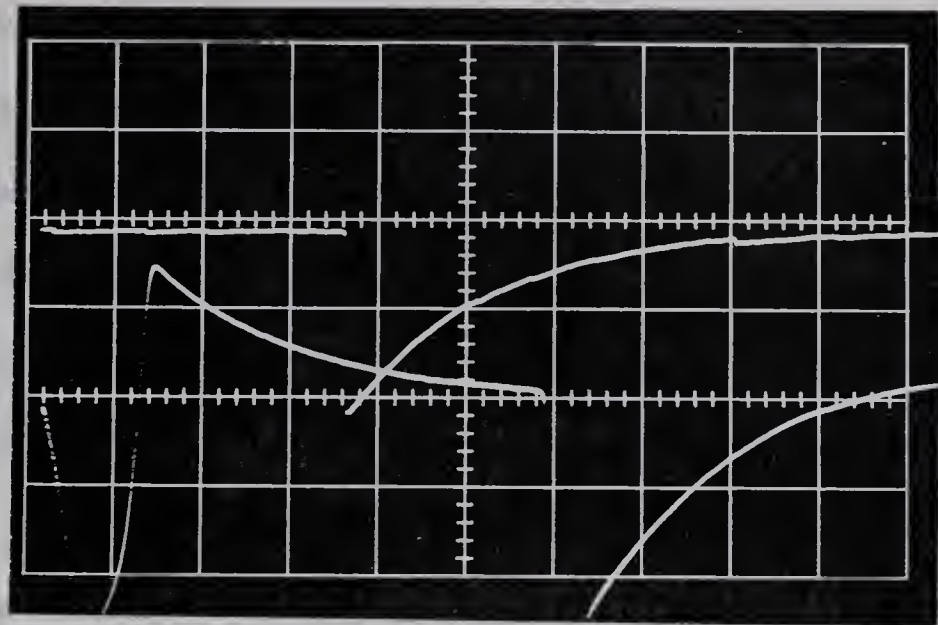
Time Scale: 0.5 ms/cm

$V = 18 \text{ Kv}$

$a = 3.6 \text{ microns}$

$v = 0.077 \text{ Km/sec}$

Figs. 3.20 and 3.21 Photomultiplier and Charge Sensitive Detector Signals.



Top Trace: 1 v/cm

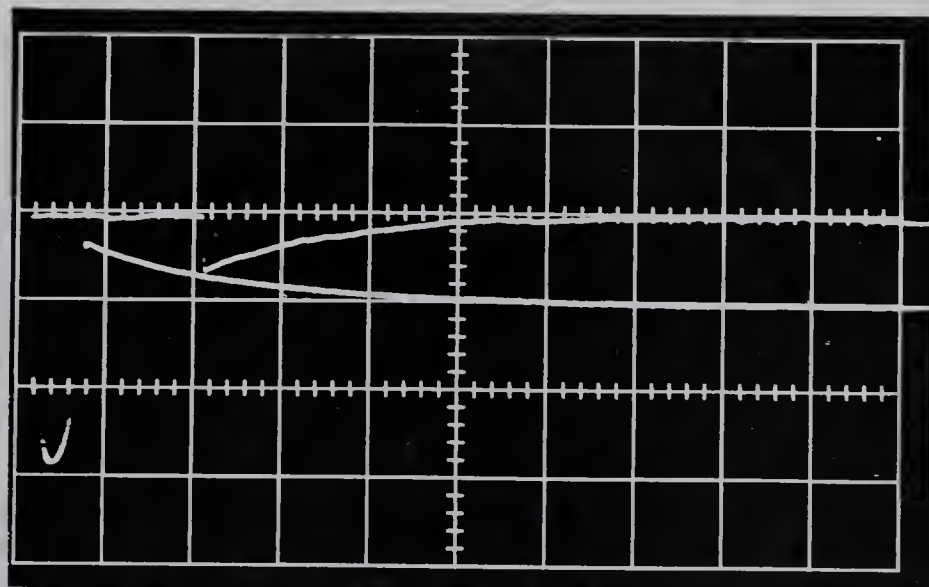
Bottom Trace: 50 mv/cm

Time Scale: 0.2 ms/cm

$V = 18 \text{ Kv}$

$a = 3.9 \text{ microns}$

$v = .096 \text{ Km/sec}$



Top Trace: 1 v/cm

Bottom Trace: 50 mv/cm

Time Scale: 0.2 ms/cm

$V = 18 \text{ Kv}$

$a = 2.4 \text{ microns (approx)}$

$v = 0.152 \text{ Km/sec (approx)}$

Figs. 3.22 and 3.23 Photomultiplier and Charge Sensitive Detector Signals.

after the arc lamp had operated for many additional hours. During this final experiment the values of V_c observed were approximately one half of the values observed earlier.

For the purpose of making a comparison between experimental values of V_c and those estimated by use of equation (3.18), the data that has been obtained during one experiment is tabulated in Fig. 3.24. The experimental and estimated values of V_c agree to within half an order of magnitude, which, in view of the nature of the estimate is an acceptable result. Inconsistencies in the values of V_c can be due to a number of factors:

1. Individual particles do not traverse the image of the light source along identical paths. This influences the value of V_c because

Particle Radius in microns	Particle Velocity in Km/sec	Experimentally Observed V_c in volts	V_c Estimated From Equation (3.18) in volts
1.7*	0.158	0.5	0.57
2.2*	0.164	0.5	0.87
2.4*	0.152	0.6	1.2
3.0*	0.095	0.7	2.9
3.5	0.105	1.8	3.6
3.9	0.096	2.0	4.7
4.7	0.079	1.8	8.3

*The first four particles traversed the first charge sensitive detector and the light beam, but did not pass through the aperture immediately preceding the last detector. Their radii and velocities were estimated from the amplitude of the first detector pulse, and the time separation between this pulse and the photomultiplier signal. The remaining particles passed through the light beam and both charge sensitive detectors.

Fig. 3.24 Comparison of Experimental and Estimated
Photomultiplier Signals

- a) the integration time δt is affected,
- b) the illumination of the image of the light source may not be uniform over the latter's whole cross section and thus, $i(t)$ is affected.

2. The intensity of the light source may fluctuate.

3. Particles traversing the light beam may be deformed and thus scatter more or less light into the photomultiplier than a spherical particle.

4. The anode current $i(t)$ that flows in response to the largest particles listed in Fig. 3.24, is significant when compared to the current that biases the individual dynodes of the photomultiplier. Thus, in spite of the bypass capacitor between the 9th and 10th dynode, the relative voltage distribution between the dynodes may change and thus alter the gain of the photomultiplier. Although linearity between light flux and anode current is generally desirable, it must be borne in mind that the purpose of the present experiment is primarily to generate an anode pulse with a useful signal to noise ratio. In principle, the dynode bias current can be increased by decreasing the values of the bias resistors. This, however, increases the load on the high voltage power supply. Secondly, in the event that an unexpectedly large light flux suddenly enters the photomultiplier, the anode current is no longer as effectively limited as it is with larger bias resistors.

A small anode current flows at all times. It is the sum of the dark current and the current that is due to a background light level that is present whether or not a particle is traversing the light beam. This sum must be less than a few microamps, otherwise it will cause an

excessively large voltage drop across the 10 M load resistor, and thereby decrease the voltage between the anode and the last dynode below the saturation voltage. Direct measurement of this anode current is difficult because the anode is at a relatively high voltage. However, the current can be estimated as follows:

1. As stated earlier in the description of the photomultiplier, the average dark current at an overall voltage of 1800 volts is 0.2 microamps. Since the dark current varies approximately as the anode sensitivity, at 420 amps/lumen, it will be of the order of 0.1 microamps.

2. The approximate anode current due to the background light level was measured indirectly by switching off the light source. In practice, when the light source is extinguished, its intensity does not vanish instantaneously, but decreases to a negligible value during a fraction of a second. During this time the voltage at the anode rises by an amount that is equal to the product of the decrease in anode current and the 10 M load resistor. This rise in anode current can only be measured if the discharge time constant of the 1000 pf high voltage coupling capacitor (see Fig. 3.15), is much larger than the time during which the intensity of the light source vanishes. For this reason the network beyond the 1000 pf high voltage coupling capacitor was removed and replaced by a 100 M input impedance VTVM. A further 15000 pf was connected in parallel with the 1000 pf coupling capacitor. The a - c equivalent circuit of Fig. 3.16 was thus changed to that of Fig. 3.25. If the light source is suddenly extinguished, an anode current step I is generated as shown in Fig. 3.25. As a result, the voltage at the

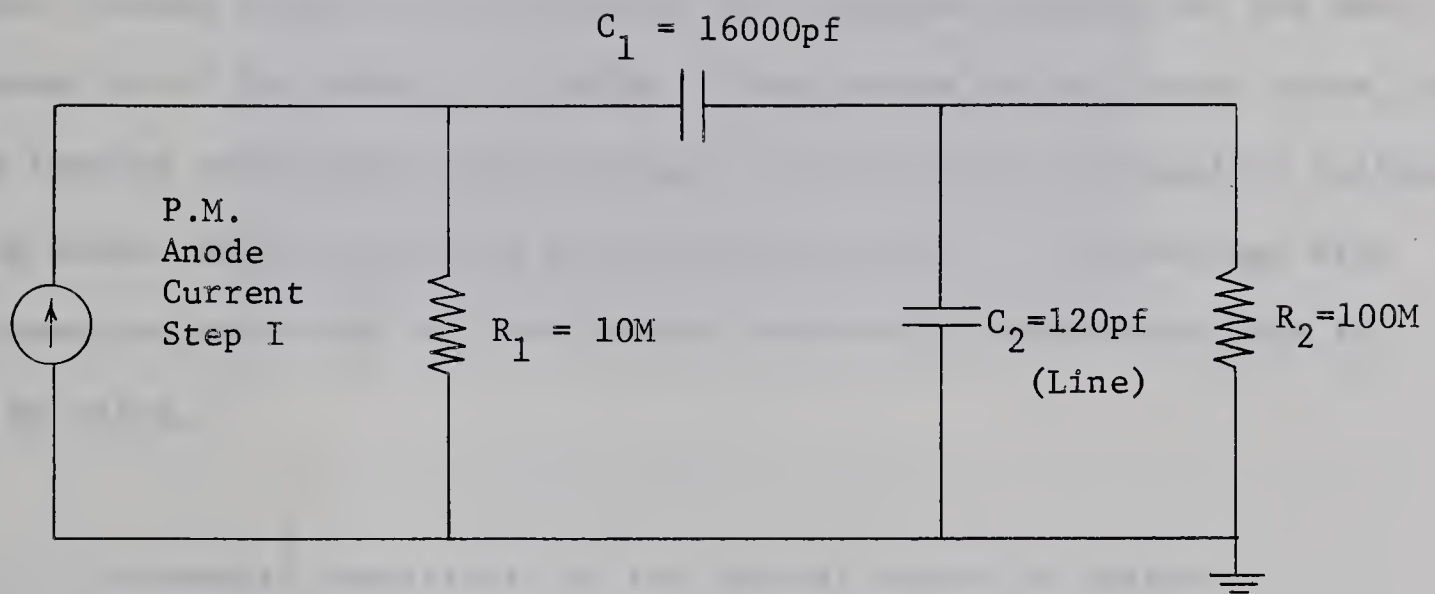


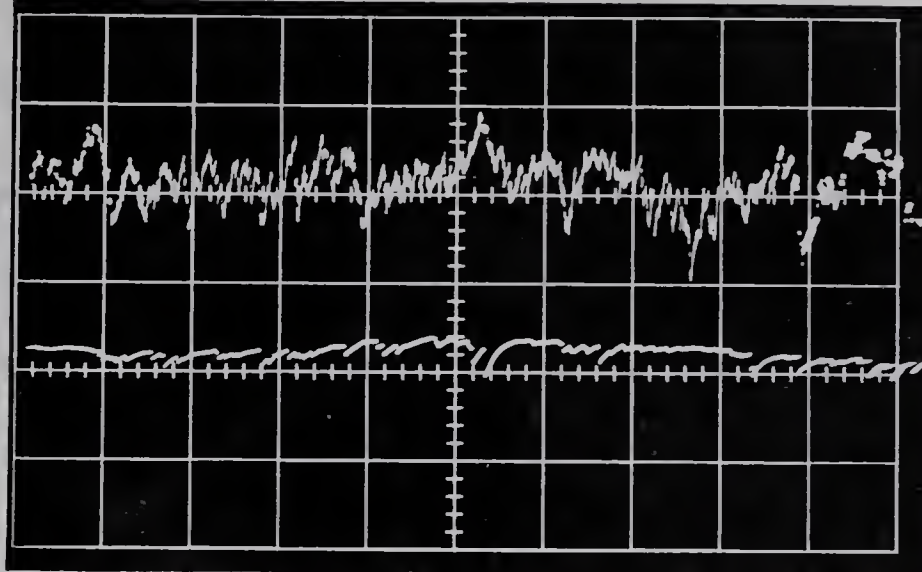
Fig. 3.25 A-C Equivalent Circuit for Measuring Photomultiplier Anode Current Due to Mean Background Light Intensity.

VTVM input rises to slightly less than $I \cdot 10\text{ M}$ with a time constant of approximately $R_1 C_2$, and then decays with a time constant of approximately $(R_1 + R_2) C_1$ (about 1.76 sec). The observed voltage rise at the VTVM was 0.8 volts. This indicates that the corresponding voltage drop across the 10 M load resistor is less than 1 volt. Hence, the corresponding anode current is approximately 0.1 microamps. It is concluded that the total voltage drop due to the sum of the foregoing current and the dark current is of the order of 2 volts. This causes no difficulty since, with the biasing arrangement shown in Fig. 3.15, the total permissible voltage drop before anode saturation sets in, is 25 volts. (The voltage drop between the anode and the last dynode, below which saturation sets in, is 80 volts.)

3.2.2.4 Threshold Sensitivity of the Optical Detection System

The optical detection system reaches its threshold sensitivity for microparticle radii between 1.5 and 2 microns. If the particles are smaller than this, the photomultiplier signal can no longer be reliably distinguished from dark current pulses, and from fluctuations in the level of the background light intensity. The photograph shown in Fig. 3.26 indicates the relative magnitudes of the latter two effects. Both traces have the same voltage scales. Note that the time scale is different from that of all the preceding oscilloscope display photographs.

As discussed previously, the amplitude of the photomultiplier anode signal in response to a microparticle of given radius is inversely proportional to the velocity of the particle. The present system is just able to detect particles with radii of 1.5 to 2 microns and with



Voltage Scale = 0.1 v/cm

Time Scale = 2.0 ms/cm

The upper trace shows the photomultiplier signal due to the presence of dark current and fluctuations in the level of the background light intensity. The lower trace shows the photomultiplier signal due to the presence of dark current only.

Fig. 3.26 The Effects of Dark Current and of Fluctuations in the level of the Background Light Intensity.

velocities of .15 Km/sec. It must therefore be extensively modified to detect particles with similar radii, and velocities in the micro-meteoroid range. The following major modifications could be adopted:

1. A zirconium concentrated arc lamp with a higher intensity than that of the present lamp could be used.
2. At present, the photomultiplier intercepts about 1/100 of the light scattered by a microparticle. This fraction can be increased in a number of ways. For instance, the system could incorporate a number of reflecting surfaces that direct more scattered light into the photomultiplier. Secondly, the distance between photocathode and particle trajectory could be decreased. Both these schemes would probably increase the intensity of the fluctuations of the background light level as seen by the photocathode. However, a lens could be positioned between particle trajectory and photocathode to enhance, relative to the background light level, the sensitivity of the system for light that originates from the point of intersection of the particle's trajectory and the light beam.

The question arises as to whether a better method can be found to differentiate between current pulses at the anode that are due to microparticles and current pulses that are due to dark current photoelectrons. For instance, rather than integrating the anode current, as in this thesis, it is possible to measure the voltage drop that is developed as the anode current flows through a large resistor. (This scheme would require a high input impedance cathode follower beyond the 1000 pf high voltage coupling capacitor that is next to the photomultiplier anode.) It is shown below by a simple argument, that integration of the anode current is a more favourable method.

a. Integration. Let it be assumed that N photoelectrons are detached from the photocathode as a particle of given size and velocity traverses the light beam. If the gain of the photomultiplier is K , then a train of KN electrons arrives at the anode. This must be distinguishable from a train of K electrons which may arrive at the anode at any time due to a dark current photoelectron. If the anode current is integrated, then the ratio of the voltage pulses due to a microparticle and a dark current photoelectron is $KN/K = N$.

b. Resistive anode load. If the anode current due to a microparticle or a dark current photoelectron flows through a resistor, then the ratio of the resulting voltage pulses is the ratio of the two anode currents. If the time intervals at which each of the N photoelectrons are detached from the photocathode, are longer than the transit time spread of the photomultiplier, then the anode current due to a microparticle will be no larger than the anode current due to a dark current photoelectron. In this case, the ratio of the voltages due to a microparticle and a dark current photoelectron is 1. In practice, a capacity of a few pf is always present in the anode circuit. Hence the duration of an anode voltage pulse due to a single photoelectron is very much larger than the transit time spread of the photomultiplier. As a result, the anode current due to the N photoelectrons is at least partially integrated and thus, for a resistive anode load, the ratio of the voltage pulses due to a microparticle and a dark current photoelectron is larger than 1, but less than N .

4. CONSIDERATIONS WITH REGARD TO THE ACCELERATION OF MICROPARTICLES

4.1 The Relationship between Accelerating Voltage and Particle Velocity

The velocity that is attained by a charged microparticle, initially at rest, as it moves in an electric field, is given by

$$\frac{1}{2} mv^2 = qW \quad \dots(4.1)$$

where W = the electric potential
through which the particle
has fallen.

If the particle is a sphere, then

$$m = \frac{4}{3} \pi a^3 \rho \quad \dots(4.2)$$

Further,

$$q = 4\pi a^2 \epsilon_o F \quad \dots(4.3)$$

where F = field intensity at the surface
of the particle due to the
charge that it carries.

When equations (4.1), (4.2) and (4.3) are combined, one obtains

$$W = \frac{\rho a v^2}{6\epsilon_o F} \quad \dots(4.4)$$

Equation (4.4) states that the potential which is required to accelerate a particle to a given velocity is proportional to the particle's mass density and radius and inversely proportional to the field intensity at its surface.

It may be helpful to consider a particular example. Let us assume that we wish to accelerate a spherical iron particle whose radius

is 1 micron and which is positively charged to a surface field intensity of $2 \cdot 10^9$ volts/meter. Of interest are the parameters of the particle and the respective potentials that are required to accelerate this particle to the lower and upper micrometeoroid velocities of 11 Km/sec and 72 Km/sec.

From equation (4.2), using the specific gravity of 7.8 for iron, the mass of the particle is computed to be

$$m = 3.26 \cdot 10^{-14} \text{ Kg.}$$

From equation (4.3) the charge on the particle is

$$q = 2.22 \cdot 10^{-13} \text{ coulombs}$$

Consequently, the charge to mass ratio is

$$\frac{q}{m} = 6.81 \text{ coulombs/Kg.}$$

For the sake of comparison, it may be noted that the foregoing charge corresponds to $1.385 \cdot 10^6$ electronic charges, and that the foregoing charge to mass ratio is $3.87 \cdot 10^{-11}$ times that of the electron.

Finally, from equation (4.1) the necessary potential to accelerate the particle to 11 Km/sec is

$$W = 8.89 \cdot 10^6 \text{ volts}$$

and the potential to accelerate the particle to 72 Km/sec is

$$W = 381 \cdot 10^6 \text{ volts.}$$

By using equation (4.4) we can construct a graph, Fig. (4.1), which shows the potential W that is required to accelerate a particle of radius a to velocity v . The graph is valid for iron particles that have been positively charged to a surface field intensity of $2 \cdot 10^9$ volts/meter.

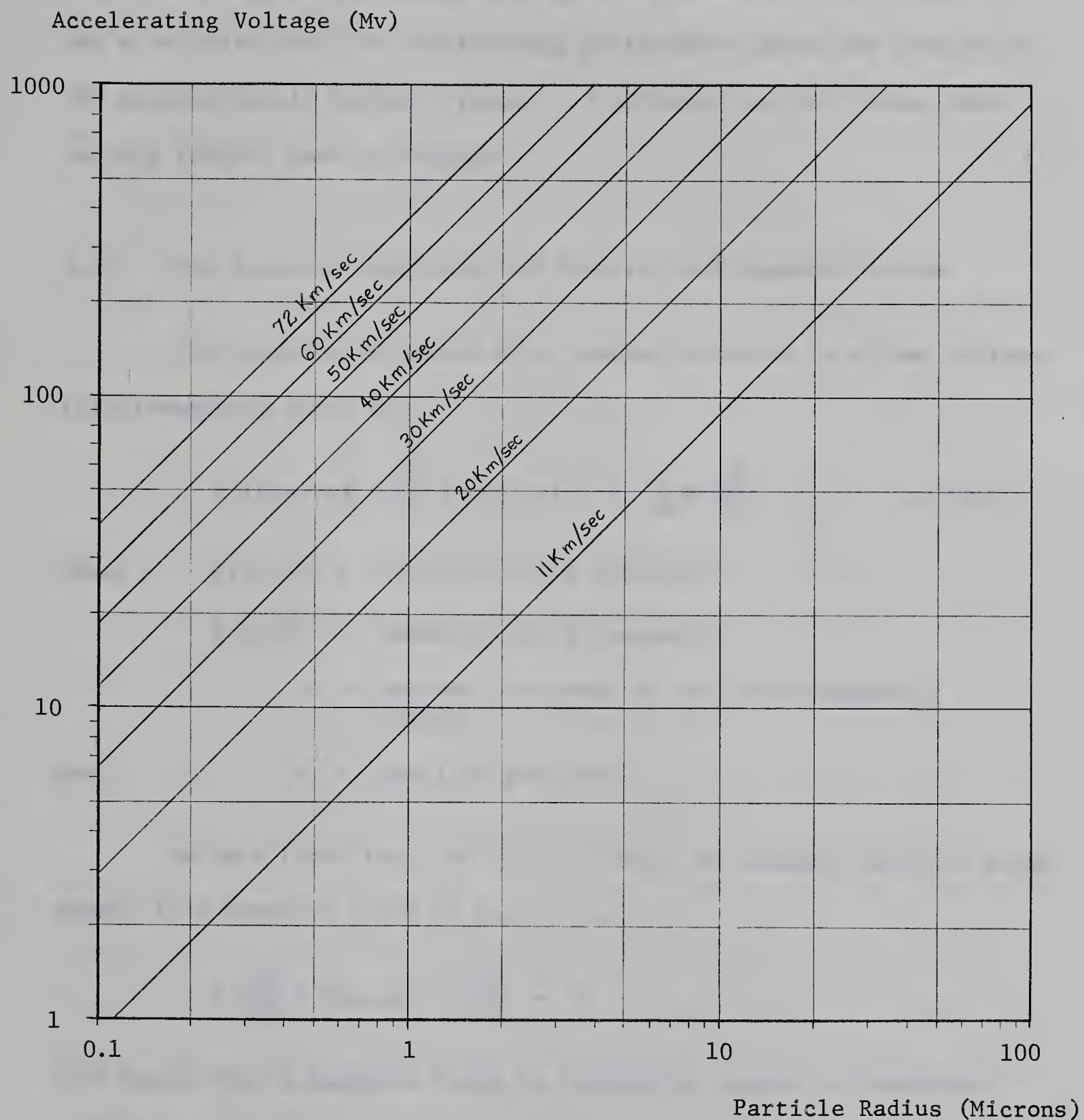


Fig. 4.1 Relationship Between Accelerating Voltage, Particle Radius and Particle Velocity for Iron Spheres with a Surface Field Intensity of $2 \cdot 10^9$ Volts/Meter.

From Fig. (4.1) it is evident that a Van de Graaff generator, being unable to supply voltages larger than about $10 \cdot 10^6$ volts, is not a suitable tool for accelerating micron sized particles throughout the micrometeoroid velocity range. A different method, using time varying fields, must be employed.

4.2 The Relative Magnitudes of Electric and Magnetic Forces

The equation of motion of a charged particle in a time varying electromagnetic field is

$$q \{ \bar{E}(s, \omega t) + \frac{d\bar{s}}{dt} \times \bar{B}(s, \omega t) \} = \frac{d}{dt} (m \frac{d\bar{s}}{dt}) \quad \dots (4.5)$$

where $\bar{E}(s, \omega t)$ = electric field intensity

$\bar{B}(s, \omega t)$ = magnetic field intensity

ω = angular frequency of the electromagnetic fields

and s = particle position

We note first that the rate at which the charged particle gains energy in a magnetic field is zero, i.e.,

$$q \{ \frac{d\bar{s}}{dt} \times \bar{B}(s, \omega t) \} \cdot \frac{d\bar{s}}{dt} = 0$$

This means that a magnetic field is inherently unable to accelerate charged particles.

Although a magnetic field cannot change the magnitude of a particle's velocity, it can change its direction. Therefore, in principle, it can be used to focus a particle's trajectory. In practice, however, one finds that the force of interaction between a charged

microparticle and a magnetic field is so weak that even for the purpose of focussing, it is unsuitable. We will briefly illustrate this through the following example.

Consider a magnetic field with an intensity of about 10^3 gauss or 0.1 weber/meter². This is the maximum magnetic field intensity that can be produced with sufficient ease for the present application. A particle that has a charge to mass ratio of 6.81 coulombs/Kg and travels through this field at 10 Km/sec would execute a path with a minimum radius of curvature of

$$\frac{mv}{qB} = 14.7 \text{ Km} .$$

Since this distance is several orders of magnitude larger than the length of any microparticle accelerator that is presently envisaged, it is evident that magnetic fields are unsuitable for focussing microparticle trajectories.

It is noted from equation (4.5) that the force which the foregoing magnetic field exerts on the particle is equivalent in magnitude to the force that would be exerted by an electric field that has an intensity of 1000 volts/meter. The fact that electric fields with intensities that are 3 or 4 orders of magnitude larger than this can easily be produced suggests that electric fields can be used more effectively than magnetic fields for the focussing of microparticle trajectories. Uses of the electric field will be discussed in the following sections. Magnetic fields will not be considered.

4.3 Some Useful Properties of the Electrostatic Field

It is important that the trajectories of particles are focussed

and aligned. Also, if the charging mechanism is inclined to and off the axis of the accelerator, the trajectories of particles must be bent before they enter the accelerating structure. Electrostatic fields are well suited to perform these functions since the trajectories of charged particles in them can be independent of the particles' charge to mass ratios. We will briefly examine this property of electrostatic fields. For this purpose equation (4.5) is simplified to

$$\frac{q}{m} \bar{E}(s) = \frac{d^2 s}{dt^2} \quad \dots(4.6)$$

We now consider the motion of two different particles having charge to mass ratios of $(q/m)_1$ and $(q/m)_2$ respectively, where

$$\left(\frac{q}{m}\right)_2 = a \left(\frac{q}{m}\right)_1 \quad \dots(4.7)$$

Now, the trajectory of the first particle, $s(t-t_o, s_o, s'_o)$, is the solution to

$$\left(\frac{q}{m}\right)_1 \bar{E}(s) = \frac{d^2 s}{dt^2} \quad \dots(4.8)$$

The trajectory of the second particle, $u(T-T_o, u_o, u'_o)$, is the solution to

$$\left(\frac{q}{m}\right)_1 \bar{E}(u) = \frac{d^2 u}{dT^2} \quad \dots(4.9)$$

where $T-T_o = a^{1/2}(t-t_o)$

From inspection of equations (4.8) and (4.9), it is evident that

$$\begin{aligned} u(T-T_o, u_o, u'_o) &= s(T-T_o, u_o, u'_o) \\ &= s(a^{1/2}(t-t_o), u_o, u'_o) \end{aligned}$$

provided the following conditions with regard to the initial velocities and initial positions are satisfied:

$$\begin{aligned} u'_0 &= s'_0 \\ \text{i.e., } \dot{u}_0 &= a^{1/2} \dot{s}_0 \end{aligned} \quad \dots(4.10)$$

$$\text{and, } u_0 = s_0 \quad \dots(4.11)$$

Thus, the two particles follow the same path in space. The second particle takes $a^{-1/2}$ of the first particle's time to cover the same section of path, and, at any point in space has $a^{1/2}$ times the first particle's velocity.

It is concluded that if an electrostatic field is designed to correct errors in or otherwise modify the trajectory of particles with a particular charge to mass ratio, then, provided the relationships (4.10) and (4.11) are satisfied, this field will be equally effective in performing the same function for other particles, irrespective of their charge to mass ratios.

In chapter 3 it was seen that the charging mechanism which has been built emits charged particles whose trajectories satisfy, to first order accuracy, the relationship (4.11). Also, if the particle rebound velocity at the surface of the charging sphere can be neglected, then relationship (4.10) is satisfied. Consequently, if the trajectories of the charged particles have to be modified prior to entering the accelerating structure, this can be accomplished at once, for all charge to mass ratios, by the same electrostatic field.

4.4 Particle Motion in a Time Varying Field

In the foregoing section an important observation has been made with regard to the focussing of particles with variable charge to mass ratios by electrostatic fields. An equally important observation will

now be made with regard to the acceleration of the above particles by time varying electric fields.

It will be recalled from the introduction, that a time varying field is selective in that synchronism can occur only for a particle with the appropriate charge to mass ratio. Since we are dealing with particles whose charge to mass ratios are different, it is relevant to investigate, if, by changing one of the parameters of a given time varying field, synchronism can occur for more than one charge to mass ratio. Since the charge to mass ratio of a particle is not known in advance, it is important that the appropriate field parameter can be changed to its new value almost instantaneously, on the basis of a signal that is generated by the particle as it passes through a detector prior to entering the accelerator.

For the present purpose, equation (4.5) is written as

$$\frac{q}{m} \bar{E}(s, \omega t) = \frac{d^2 s}{dt^2} \quad \dots(4.12)$$

Equation (4.12) suggests that, at least in principle, particles with different charge to mass ratios might be accommodated if one were to change the accelerating field's intensity, its spatial dependence or its time dependence. From a practical point of view it is desirable not to change the field's intensity but to keep it as high as breakdown considerations within the accelerating structure permit, so that the maximum velocity is imparted to each particle. The spatial dependence of the field cannot be changed, at least not in a continuous manner, since it is a function of the geometry of the drift tubes and high voltage gaps. It is possible, however, to change the time dependence of the field, that is its frequency and its phase at the instant of

particle entry. It will be shown that this is sufficient to enable a single structure to accelerate particles with a wide range in charge to mass ratios.

Let $\bar{E}(s, \omega_1 t)$ be the correct field to accelerate a particle with a given set of parameters. Let the trajectory that the particle follows be

$$s = s(\omega_1(t-t_{o1}), s_o, s'_o) \quad \dots(4.13)$$

and designate the particle parameters by:

$$\text{charge to mass ratio} = \left(\frac{q}{m}\right)_1$$

$$\text{entry phase} = \omega_1 t_{o1}$$

$$\text{position at entry} = s_o$$

$$\text{and initial velocity} = \dot{s}_o$$

From equation (4.12) the equation of motion of this particle is

$$\frac{1}{\omega_1^2} \left(\frac{q}{m}\right)_1 \bar{E}(s, \omega_1 t) = \frac{d^2 s}{d(\omega_1 t)^2} \quad \dots(4.14)$$

Now, consider a particle with charge to mass ratio $(q/m)_2$, moving in the field $\bar{E}(s, \omega_2 t)$. Again let

$$\left(\frac{q}{m}\right)_2 = a \left(\frac{q}{m}\right)_1$$

The equation of motion of this particle can be written as

$$\frac{1}{\omega_2^2} \left(\frac{q}{m}\right)_2 \bar{E}(u, \omega_2 t) = \frac{d^2 u}{d(\omega_2 t)^2} \quad \dots(4.15)$$

From equations (4.14) and (4.15) it is evident that

$$\begin{aligned} u &= u(\omega_2(t-t_{o2}), u_o, u'_o) \\ &= s(\omega_2(t-t_{o2}), u_o, u'_o) \end{aligned} \quad \dots(4.16)$$

provided that the following relationships hold:

$$\frac{1}{\omega_2} \left(\frac{q}{m} \right)_2 = \frac{1}{\omega_1} \left(\frac{q}{m} \right)_1$$

i.e., frequency $\omega_2 = a^{1/2} \omega_1$, ... (4.17)

entry phase $\omega_2 t_{o2} = \omega_1 t_{o1} + 2n\pi$... (4.18)

where $n = 0, \pm 1, \pm 2,$

position of entry $u_o = s_o$... (4.19)

and $u'_o = s'_o$

i.e., initial velocity $\dot{u}_o = a^{1/2} \dot{s}_o$... (4.20)

From the preceding discussion, particularly from equation (4.16), it is evident, that if a particle of given charge to mass ratio can move in synchronism with, and thus continuously gain energy from a given accelerating field at a given frequency, then a particle with a different charge to mass ratio can do the same if it has suitable initial conditions and if the frequency of the accelerating field is changed to the appropriate new value.

At this point it may be relevant to list the implications of the foregoing findings:

1. Particles with different charge to mass ratios but correctly related initial conditions maintain the initial ratios between their velocities while traversing an electrostatic field. It follows from equations (4.10) and (4.20) that, upon emerging from the electrostatic field, the ratios between the velocities of the particles are such that each of them can achieve synchronism with a time varying field; it is only necessary that the frequency and initial phase of the time varying

field be preset according to equations (4.17) and (4.18).

2. The above particles maintain the ratio between their initial velocities while moving through the time varying field, and, thus, upon leaving it, could enter a further field and again achieve synchronism. This is true whether the region separating the two time varying fields is field free or contains an electrostatic field.

3. The above particles, having different charge to mass ratios, will have different velocities, and, thus, will take different lengths of time to cover the distance separating the two time varying fields. It is relevant to express the time taken by each particle in terms of number of cycles of either the time varying field the particle has just left or the one it is about to enter. Let us consider two particles with charge to mass ratios $(q/m)_1$ and $(q/m)_2$ for which the appropriate frequencies of, say, the field they have just left, are $\omega_{1,n}$ and $\omega_{2,n}$ respectively. (We could equally well present the following argument by referring to the frequencies of the field the particles are about to enter. Let us, for later use, designate these frequencies by $\omega_{1,n+1}$ and $\omega_{2,n+1}$.) If the distance separating the two time varying fields is z_1 , then

$$\Delta(\omega_1 t_1) = \omega_1 \int_0^{z_1} \frac{dz}{v_1}$$

and

$$\Delta(\omega_2 t_2) = \omega_2 \int_0^{z_1} \frac{dz}{v_2}$$

where t_1 and t_2 denote the times taken by the particles, and v_1 and v_2 denote their respective velocities. From the above equations, from equation (4.20) and from the fact that the ratio of velocities of different particles is conserved, we obtain

$$\begin{aligned}\Delta(\omega_2 t_2) &= \omega_2 \int_0^{z_1} \frac{dz}{a^{1/2} v_1} \\ &= \frac{\omega_2}{a^{1/2}} \frac{\Delta(\omega_1 t_1)}{\omega_1}\end{aligned}$$

By use of equation (4.17) the above becomes

$$\Delta(\omega_2 t_2) = \Delta(\omega_1 t_1)$$

We conclude that if the fields at frequencies $\omega_{2,n}$ and $\omega_{2,n+1}$ have the same phase relationship with respect to each other as the fields at frequencies $\omega_{1,n}$ and $\omega_{1,n+1}$, then z_1 can be chosen so that both of the foregoing particles maintain synchronism as they move from one time varying field into the next one. Again, this is true whether the region separating the time varying fields is field free or contains an electrostatic field.

4.5 A Brief Proposal for Accelerating Particles with Differing Charge to Mass Ratios

In the foregoing pages some general properties of the motion of particles with variable q/m in electromagnetic fields were discussed. Now, use is made of these properties to propose a principle of operation for a microparticle accelerator.

The basic building block of the accelerator is a section which consists of a number of drift tubes and high voltage gaps, as shown in Fig. 4.2. Alternate drift tubes are connected in parallel. One series of drift tubes thus formed is joined to one terminal of an oscillatory high voltage source, the other series of drift tubes is joined to the

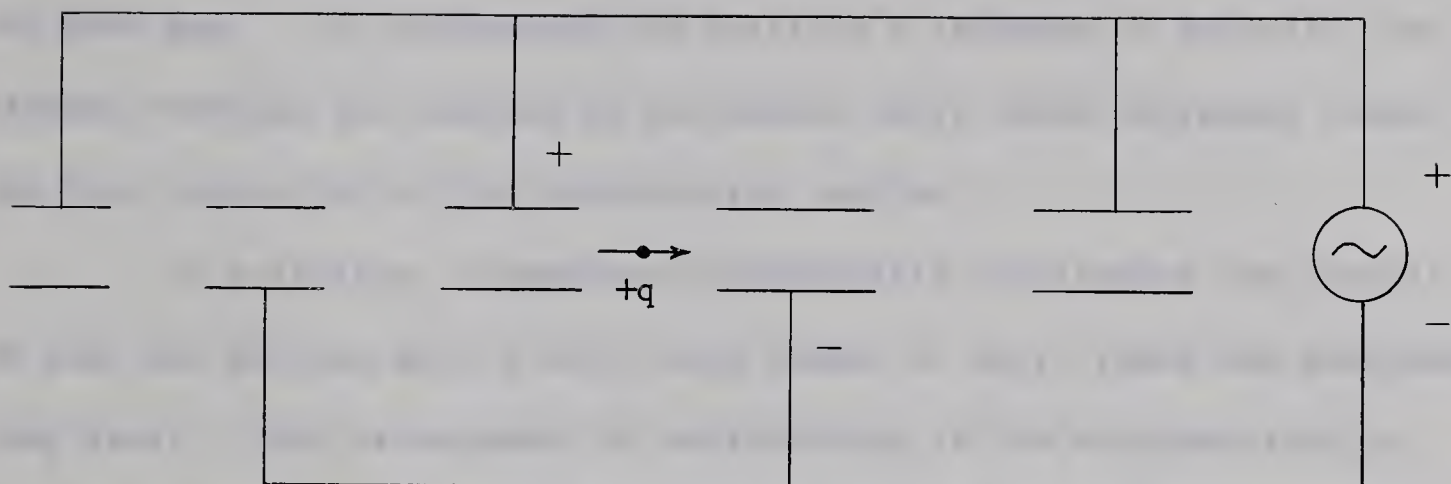


Fig. 4.2 A Sequence of Drift Tubes and Accelerating Gaps

other terminal. If a microparticle has the appropriate initial velocity, entry phase and q/m , it can achieve synchronism. In other words, while the particle traverses a gap, the polarity of the voltage source is such that the particle is accelerated. While the particle travels through and is shielded within a drift tube, the polarity of the voltage source reverses, so that the particle is again accelerated upon emerging into the next gap. To accommodate the particle's increase in velocity, the distance between the centres of successive drift tubes increases toward the high energy end of the accelerating section.

In principle, a complete microparticle accelerator can consist of just one section with a very large number of drift tubes and accelerating gaps. This arrangement is satisfactory if the microparticle is injected with a high initial velocity so that, for a given voltage gain, its subsequent change in velocity is small. An accelerator design utilizing this method, is proposed in reference (79) and (80), where a 2 million volt Van de Graaff generator is used to accelerate microparticles prior to injection. The foregoing references also suggest a method which makes use of the initial velocity of the microparticle in order to compute and pre-set the frequency of the accelerator section so that synchronism can occur. This method, in more generalized form, is also applied below.

The design of an accelerator is somewhat more difficult if microparticles are injected at low velocities. In this case the microparticle undergoes a large change in velocity as it gains energy, and consequently the spacing between the centres of successive drift tubes has to progressively increase to an excessively large value. To circumvent this problem, and also to provide a method to accelerate particles to the highest micrometeoroid velocities, the following accelerator design is

suggested.

Consider Fig. 4.3. The accelerator shown consists of n sections. The distances between the centres of successive drift tubes are chosen so that, for the accelerating voltage waveform and frequency present in each section, a particle with a particular q/m can achieve synchronism. Further, the voltage wave forms of all sections have a definite phase relationship (which is time dependent), and the distances and electrostatic focussing fields between individual sections are such, that the above particle maintains synchronism as it moves from one section into the next one. Now, as shown at the beginning of this chapter, if the phase relationship of the voltage wave forms in each section is maintained, but all frequencies are changed by the same appropriate factor, then particles with arbitrary q/m can achieve synchronism and be accelerated. The work which follows, sketches a practical method whereby the foregoing accelerator design can be realized.

The voltage gain of each section shown in Fig. 4.3 is such that the energy of a synchronous particle as it enters the i^{th} section, is qW_i . The corresponding velocity is

$$v_i = \left(\frac{2qW_i}{m} \right)^{1/2}$$

The distance between the centres of the first two drift tubes of each section is h_i , and thus the time required by a synchronous particle to traverse this distance is

$$\Delta t_i = \frac{h_i}{v_i} = h_i \left(\frac{2qW_i}{m} \right)^{-1/2}$$

For reasons that become apparent shortly, the values of h_i and W_i are chosen so that

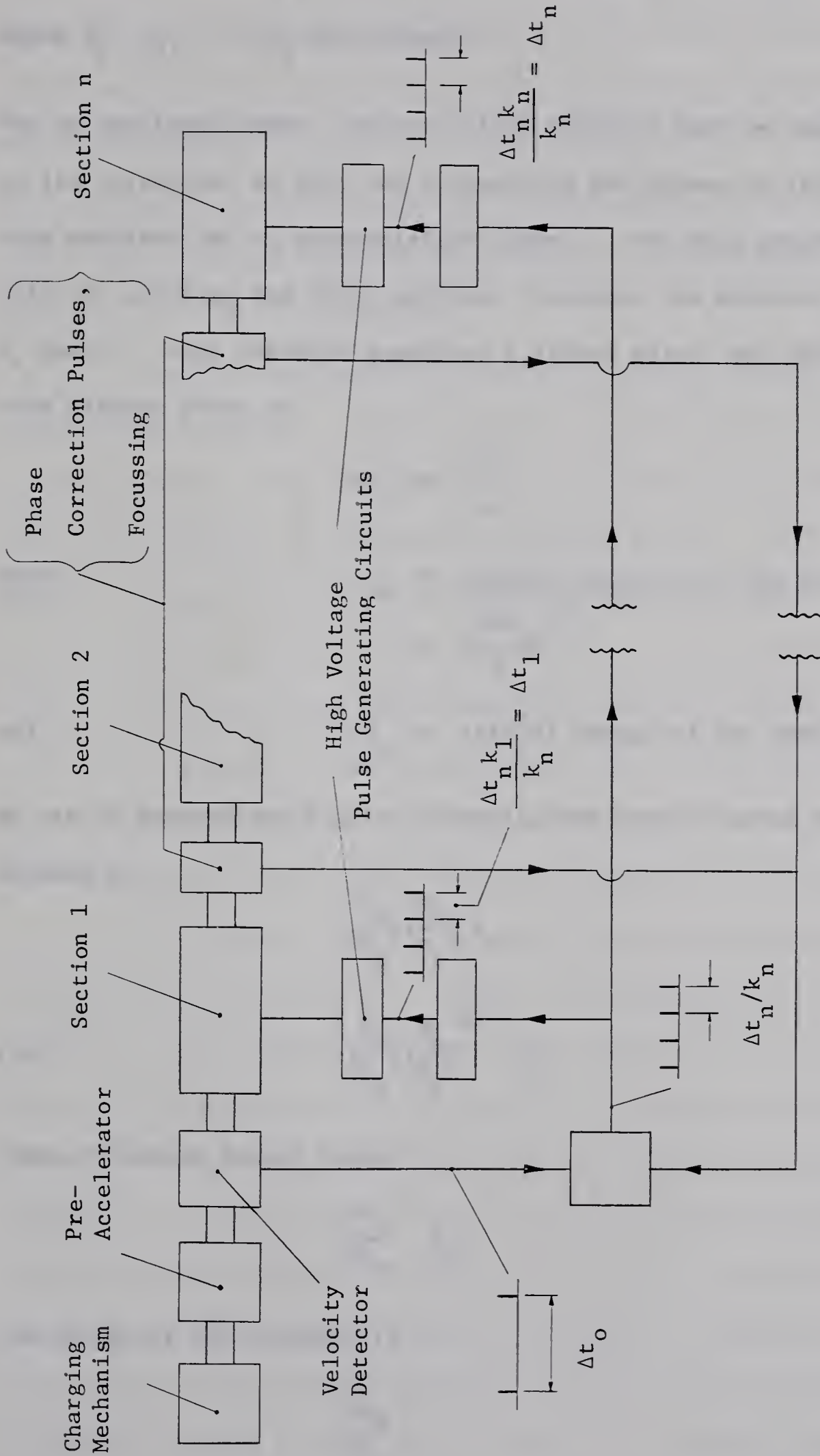


Fig. 4.3 Sketch of Microparticle Accelerator Proposal

$$\Delta t_1 : \Delta t_2 \cdots : \Delta t_n = k_1 : k_2 \cdots : k_n$$

where $k_1, k_2, \cdots k_n$ are integers.

Now as mentioned above, the particle's velocity must be measured prior to its injection, so that the frequencies and phases of the n accelerating sections can be appropriately preset. For this reason, the particle, prior to entering the first section, traverses two detectors a distance h_o apart. Each detector generates a signal pulse, and the time separation between these is

$$\Delta t_o = \frac{h_o}{v_o}$$

where

$$\begin{aligned} v_o &= \text{initial velocity of the particle} \\ &= \left(\frac{2qW_o}{m} \right)^{1/2} \end{aligned}$$

and

$$qW_o = \text{initial energy of the particle.}$$

By use of appropriate digital circuits, the time interval Δt_o is divided by

$$\left(\frac{h_o}{h_n} \right) \left(\frac{v_n}{v_o} \right) k_n$$

i.e.

$$\left(\frac{h_o}{h_n} \right) \left(\frac{W_n}{W_o} \right)^{1/2} k_n$$

Since the above factor equals

$$\frac{\Delta t_o}{\Delta t_n} \cdot k_n$$

the result of the division is

$$\frac{\Delta t_n}{k_n}$$

Voltage pulses are now generated at intervals of $\Delta t_n / k_n$ seconds. These pulses are sensed by the circuits shown in Fig. 4.3, which, depending upon the accelerating section they serve, generate an output pulse for every k_n^{th} , k_{n-1}^{th} , \dots k_1^{th} pulse received. The output pulses trigger the appropriate high voltage pulse generating circuits, which then provide the high voltage pulses of the required time durations Δt_n , Δt_{n-1} , \dots Δt_1 , respectively.

An additional particle detector is located between each of the accelerating sections. These detectors provide signals that are used to correct small errors in phase, i.e., they delay or advance the pulse train that consists of pulses $\Delta t_n / k_n$ seconds apart. Note that this does not change the phase relationship between the voltage wave forms in the various sections. To minimize phase errors, the wave form produced by the high voltage pulse generating circuit is such that the accelerator operates in the phase stable mode. Since phase stability introduces radial instability, a particle's trajectory is refocussed each time it traverses the region between two accelerating sections.

The foregoing proposal has dealt with one particular method of accelerating microparticles. Other, less sophisticated methods may be possible. For instance, in view of the success of the optical detection scheme, the following method is suggested. Consider a structure which, similar to the previous one, consists of alternate drift tubes and gaps. Initially, all drift tubes are held at a high negative potential. As a positively charged particle enters a drift tube, it is detected and a signal is generated. This signal is then used to ground the drift tube while the particle is shielded within. The process is repeated each time the particle enters a drift tube, so that it is always accelerated as it

traverses the following gap. Evidently, as mentioned above, optical detection is ideally suited for this method of acceleration. A particularly simple method of optical detection could consist of directing a laser beam along the axis of the accelerator. The light scattered by a particle as it travels inside the beam could be detected by appropriately positioned photomultipliers. Utilization of this method may have to await the development of suitable lasers in the blue spectrum, since it is in this range that photomultipliers are most sensitive and exhibit the least dark current.

In conclusion it should be mentioned that variations in either of the two foregoing accelerating methods are possible. Much detailed study has yet to be done in evaluating their relative merits.

5. OPTICAL DETECTION OF UNCHARGED PARTICLES

It has been pointed out in the introduction to this thesis, that an optical detection technique can be of value when experiments are conducted with microparticles that carry no charge. This was borne out during the developmental work of the optical detection technique described in this thesis.

While experiments were conducted with the combination of the optical and charge detection systems shown in Figs. 3.13 and 3.14, photomultiplier signals were occasionally observed in the absence of corresponding charge sensitive detector signals. On the basis of the two following experiments, it was concluded that these photomultiplier signals were due to the light scattered by microparticles, which, although emitted by the charging mechanism, were essentially uncharged.

During the first experiment a thin sheet of metal foil was used to cover the charging mechanism aperture which immediately precedes the first charge sensitive detector. The metal foil intercepted all particles emitted by the charging mechanism. No signal was recorded from the charge sensitive detectors or from the photomultiplier. This experiment conclusively demonstrated that the photomultiplier signals, which previously appeared without any corresponding signal from the charge sensitive detector, were associated with the particle charging mechanism and were not due to stray electromagnetic pick-up. The results of the experiment thus did not deny the possibility that the anomalous photomultiplier signals could be due to uncharged particles.

A second possibility existed. Within the charging mechanism, high electric fields exist and there is a motion of particles. As a result

it is easily possible for occasional electrical discharges to take place with the emission of visible light. In the apparatus used in this University the walls of the charging mechanism were opaque and no attempt was made to observe any such light flashes. The existence of flashes was privately reported by other workers in this field. They have also been referred to earlier in this thesis as a possible explanation of the cratering which took place on the surface of the charging sphere. Whether or not such light flashes were of sufficient intensity to be seen by the human eye, they might be detected by the photomultiplier and so give rise to the anomalous photomultiplier signals. To investigate the latter possibility, the sheet of metal foil which had previously been used to prevent the passage of microparticles, was replaced by a small sheet of transparent plastic. Again, the sheet of plastic prevented the passage of all microparticles. Once again, no photomultiplier signals were observed. On the basis of this and the preceding experiment it was thus concluded that the contact charging mechanism may occasionally emit uncharged particles, or particles which have not undergone the normal contact charging process, and therefore carry an amount of charge which is below the threshold sensitivity of the charge sensitive detection system.

The typical shape of one of the anomalous photomultiplier voltage pulses is sketched in Fig. 5.1. (No photographs were obtained.) The amplitudes of the pulses were of the order of one volt. An estimate of the velocity of the microparticle assumed to be responsible for this pulse, may be obtained from the magnitude of the time increment δt . The observed values of δt were of the order of 0.1 milliseconds. It

will be recalled from the discussion of chapter 3 (p.95), that

$$\delta t = \frac{\text{diameter of image of arc lamp}}{\text{particle velocity}}$$

From this relationship, using 1.5 mm as the diameter of the image of the arc lamp, the velocities of the foregoing particles were estimated to be of the order of 15 meters/second, which is about one order of magnitude less than the velocity of the normally charged particles.

With reference to Fig. 2.7, p.35, a possible explanation for the emission of uncharged particles is that some particles may be escaping through the aperture in wall C, without having come in contact with the charging sphere. Another possibility is that some particles, being initially misaligned, may glance off the inside of the surface of one of the two apertures in front of the charging electrode. While in contact with the aperture, some particles could be discharged and re-directed so as to subsequently traverse the light beam.

While conducting the latter of the two foregoing experiments, another curious phenomena was observed. As mentioned previously, a small sheet of plastic was positioned in front of the aperture immediately preceding the first charge sensitive detector. A diagram illustrating this is sketched in Fig. 5.2. Although the sheet of plastic prevented particles from traversing the charge sensitive detectors, a signal was sometimes noted in the detector nearest the charging mechanism. Two distinct types of signals were observed. These are sketched in Fig. 5.3. It is believed that these signals were generated each time a charged microparticle impinged upon the right hand surface of the plastic barrier. That is, the presence of the particle charge would polarize the left hand surface of the plastic, which in turn would lead

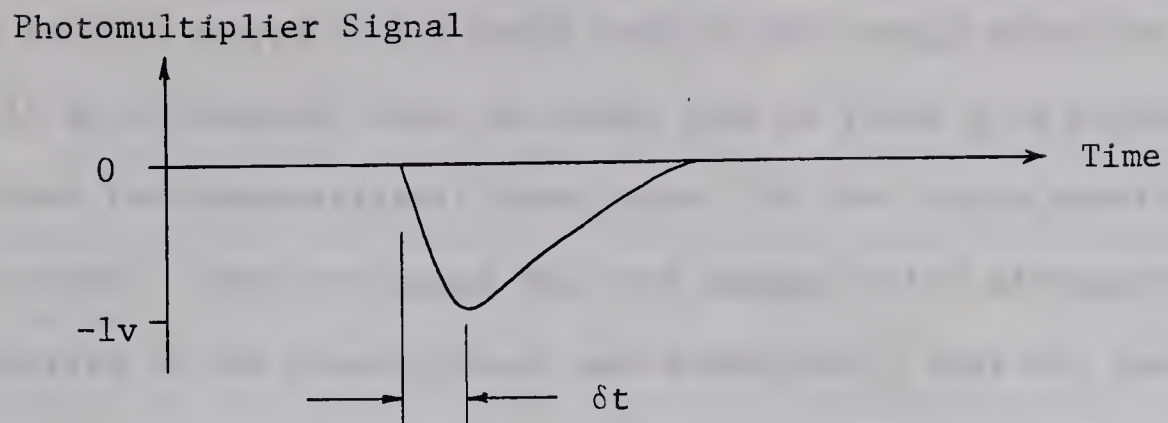


Fig. 5.1 Anomalous Photomultiplier Signal

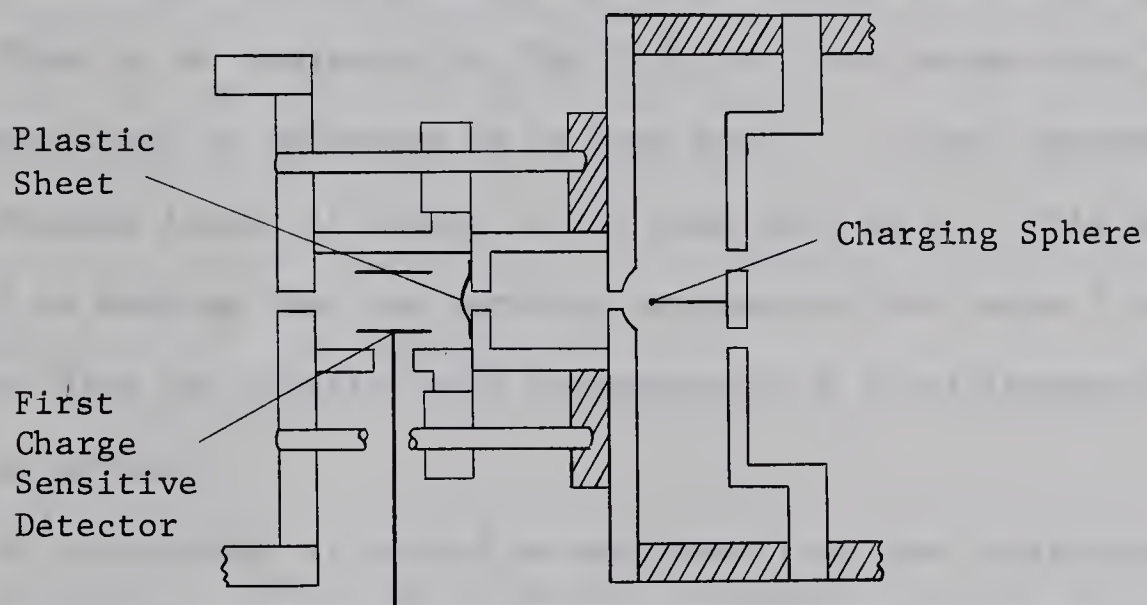


Fig. 5.2 Blocking of Particle Aperture by Small Plastic Sheet

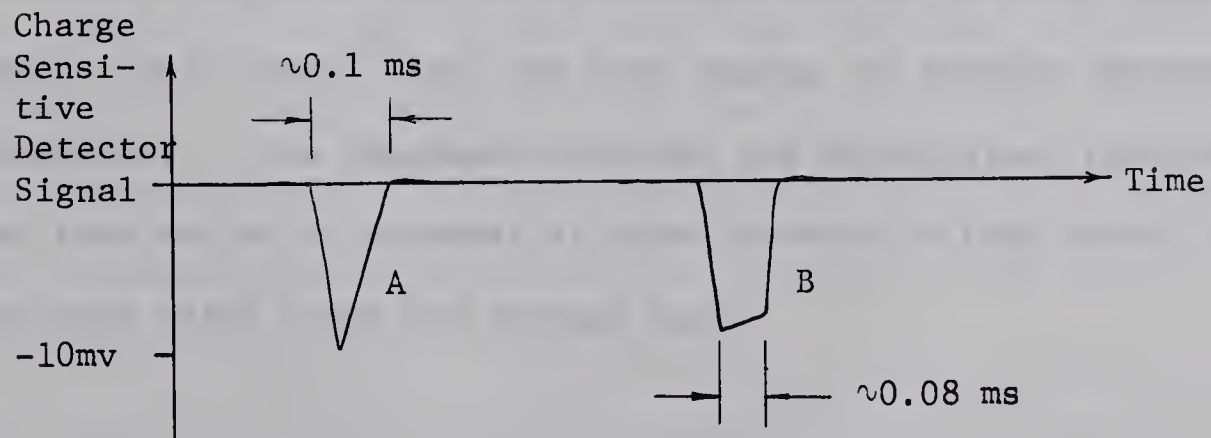


Fig. 5.3 Charge Sensitive Detector Response to Induced Polarization on Small Plastic Sheet

to an induced charge on the drift tube of the charge sensitive detector.

It is of interest that the decay time of pulse A is significantly less than the characteristic decay time τ of the charge sensitive detection system. This indicates that the charge of the microparticle is not transferred to the plastic sheet and subsequently does not leak off by the usual conduction process. The latter process would require a time several orders of magnitude larger than τ , and in that case the decay time of pulse A would also be τ . Rather, it is suspected that the microparticle rebounds from the plastic sheet, with little or no loss of charge.

Pulse B, as indicated in Fig. 5.3, at first decays with a time constant which is estimated to be very near τ . Then, approximately 0.1 milliseconds later, it decays at the same rate as A. This may be interpreted as meaning that the particle responsible for pulse B does not rebound from the plastic until approximately 0.1 milliseconds after its time of arrival.

In concluding, it should be mentioned that the interpretation of the foregoing phenomena is of a very speculative nature, and that further experiments would be in order. At the time at which these observations were made, they were somewhat outside the main sphere of interest of this thesis, and, for this reason, no further experiments were conducted. The phenomena observed are nevertheless reported, because they may be of interest to other workers in this field, and because they offer scope for further work.

6. CONCLUSION

Since micrometeoroids are of great interest to the space sciences, it is important that methods are developed for accelerating micron sized particles to meteoroid velocities in the laboratory. A promising method consists of electrically charging suitable microparticles and introducing them into a strong electric field. The charging is reliably accomplished by bringing microparticles in contact with a spherical electrode which is kept at a high voltage. The effectiveness of this method is limited by field intensification during the charging process and ensuing electrical breakdown, at the surface of the microparticle. It is shown that field intensification is minimized and that the effectiveness of the charging process can increase, as the size of the charging sphere decreases and approaches that of the microparticle.

The analysis of charged particles, that is measurement of their charge and velocity, is carried out by use of a charge sensitive detection technique. The latter, being independent of particle detector, line and amplifier input capacities, is simpler to use and more versatile than a voltage sensitive detection technique.

An optical detection method has been developed, whereby particles are sensed by a photomultiplier as they traverse an intense light beam. Unlike charge detection, this method does not require detector screening. It thus places no physical obstacle into the path of particles, and is therefore ideally suited for repeated use in a long accelerating structure. Further, since the optical detection method can be used for the analysis of particles that carry no charge, it may be indispensable for certain experiments.

All known methods of acceleration, except those employing d.c. fields, require a particle to have a fixed charge to mass ratio. Some variation in charge to mass ratio is unavoidable with microparticles, and therefore existing methods of acceleration have to be modified. The optical detection techniques developed in this thesis are particularly helpful.

APPENDIX



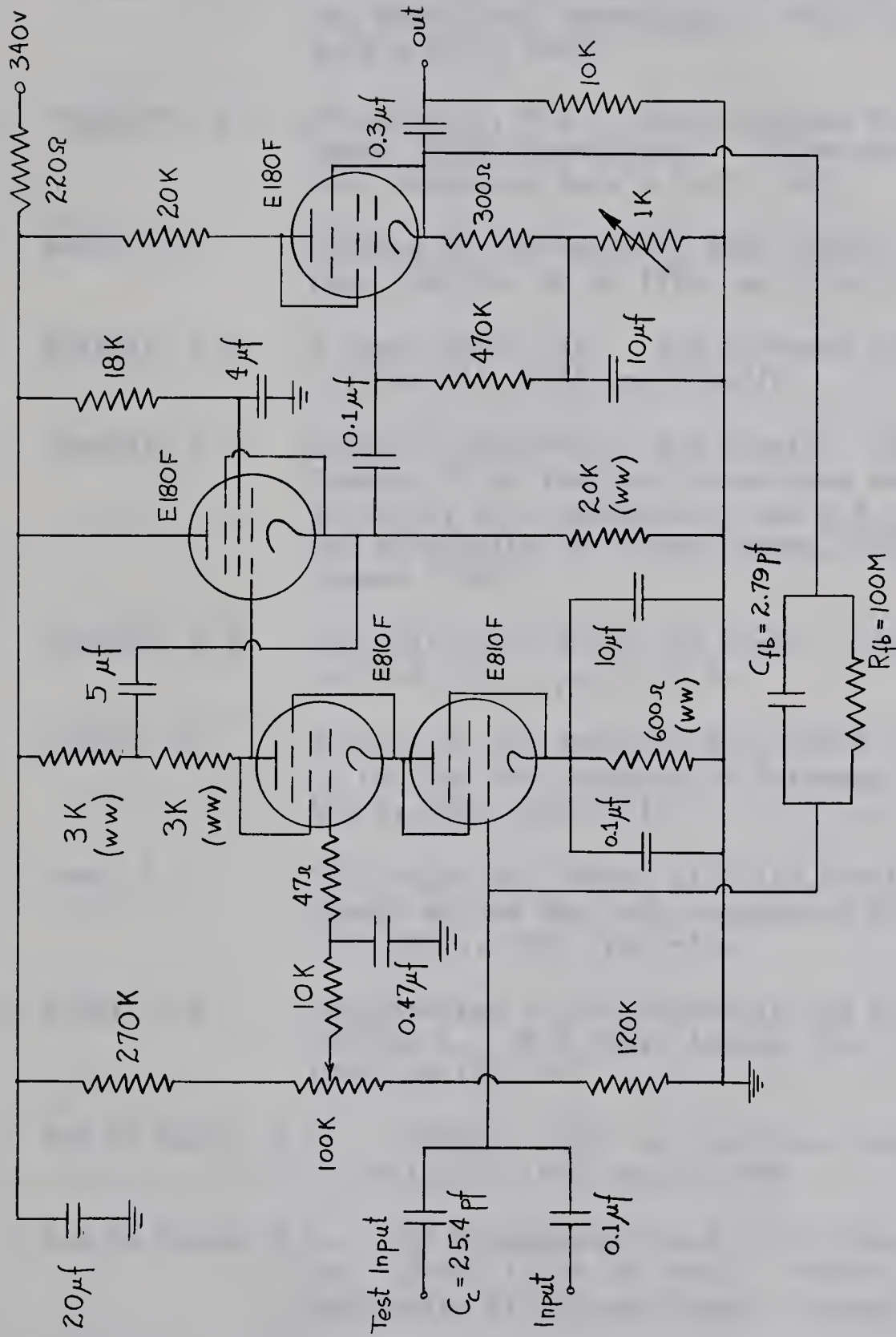


Fig. A.2 Circuit Diagram of Charge Sensitive Amplifier (From Ref. 68)

BIBLIOGRAPHY AND REFERENCES

1. Burbank, P.B. Meteoroid Environment for Near Earth, Cislunar and Near-Lunar Operations. NASA Technical Note D-2747, 1965.
2. Davidson, J.R. and Sandorff, P.E. Environmental Problems of Space Flight Structures. II Meteoroid Hazard. NASA Technical Note D-1493, 1963.
3. Harwit, M. Origins of the Zodiacal Dust Cloud. J. Geophys. Res., Vol.68, No.8, 1963, pp.2171-2179.
4. Whipple, F.L. A Comet Model III. The Zodiacal Light. Astrophys. J., Vol.121, 1955, pp.750-770.
5. Jacchia, L.G. Meteors, Meteorites, and Comets: Interrelations. Chapter 22 in The Moon Meteorites and Comets. Edited by B.M. Middlehurst and G.P. Kuiper, The University of Chicago Press, Chicago and London (1963).
6. Whipple, F.L. The Dust Cloud About the Earth. Nature, Vol.189, No.4759, 1961, pp.127-128.
7. Harwit, M. Origins of the Zodiacal Dust Cloud II. Annals of the New York Academy of Sciences, Vol.119, Art.1, 1964, pp.68-71.
8. Donn, B. The Origin and Nature of Solid Particles in Space. Annals of the New York Academy of Sciences, Vol. 119, Art.1, 1964, pp.5-16.
9. Allen, C.W. The Spectrum of the Corona at the Eclipse of 1940 October 1. M.N. Roy. Astron. Soc., Vol. 106, 1946, pp.137-150.
10. Van de Hulst, H.C. Zodiacal Light in the Solar Corona. Astrophys. J., Vol.105, 1947, pp.471-488.
11. Van de Hulst, H.C. The Chromosphere and the Corona. Chapter 5, Sec. 12 and 13 in The Sun. Edited by G.P. Kuiper, University of Chicago Press, Chicago, Illinois (1953).
12. Schmidt, R.A. A Survey of Data on Microscopic Extraterrestrial Particles (Revised June 1964) NASA Technical Note D-2719, 1965.
13. Ingham, M.F. Observation of the Zodiacal Light From a Very High Altitude Station. IV. The Nature and Distribution of Interplanetary Dust. M.N. Roy. Astron. Soc., Vol. 122, 1961, pp.157-176.

14. Kaiser, T.R. Meteors and the Abundance of Interplanetary Matter. Space Science Reviews 1 (1962-1963) pp.554-575, D. Reidel Publishing Co., Dordrecht, Holland.
15. Giese, R.H. Light Scattering by Small Particles and Models of Interplanetary Matter Derived from the Zodiacal Light. Space Science Reviews 1 (1962-1963) pp.589-611.
16. Ingham, M.F. Interplanetary Matter. Space Science Reviews 1 (1962-1963) pp.576-588.
17. McKinley, D.W.R. Meteor Science and Engineering. Sec.2-4. McGraw-Hill Book Co., Inc. New York, Toronto, London. (1961).
18. Millman, P.M. and McKinley, D.W.R. Meteors. Chapter 21 in The Moon Meteorites and Comets. Edited by B.M. Middlehurst and G.P. Kuiper, The University of Chicago Press, Chicago and London (1963).
19. Wlochowics, R. Interplanetary Space. III. Meteoroids. Can. Aeron. and Space J., Vol.10, No.5, 1964.
20. Whipple, F.L. The Theory of Micrometeorites. Science, Vol.110, 1949, p.438.
21. Loc. Cit. (12).
22. Crozier, W.D. Five Years of Continuous Collection of Black, Magnetic Sperules from the Atmosphere. J. Geophys. Res., Vol.67, No.6, 1962, pp.2543-2548.
23. Thiel, E. and Schmidt, R.A. Spherules From the Antarctic Ice Cap. J. Geophys. Res., Vol.66, No.1, 1961, pp.307-310.
24. Hodge, P.W. and Wright, F.W. Study of Particles for Extraterrestrial Origin. 3. Analyses of Dust Particles From Polar Ice Deposits. J. Geophys. Res., Vol.69, No.14, 1964, pp.2919-2931.
25. Laevastu, T. and Mellis, O. Extraterrestrial Matter in Deep-Sea Deposits. Trans. Am. Geophys. Union, Vol.36, No.3, 1955, pp.385-387.
26. Bruun, A.F., Langer, E. and Pauly, H. Magnetic Particles Found by Raking the Deep Sea Bottom. Deep Sea Res., Vol.2, 1955, pp.230-246.
27. Pettersson, H. Cosmic Spherules and Meteoric Dust. Sci. Am., Vol. 202, No.2, pp.123-132.

28. Crozier, W.D. Black, Magnetic Spherules in Sediments. J. Geophys. Res., Vol. 65, No.9, 1960, pp.2971-2977.
29. Castaing, R. and Fredriksson, K. Analyses of Cosmic Spherules with an X-Ray Microanalyzer. Geochim. et Cosmochim. Acta, Vol. 14, 1958, pp.114-117.
30. D'Aiutolo, C.T. The Micrometeoroid Satellite Explorer XIII (1961 CHI). Collected Papers on Design and Performance NASA Technical Note D-2468, 1964.
31. O'Neal, R.L. The Explorer XXIII Micrometeoroid Satellite. Description of Preliminary Results for the Period November 6, 1964 Through February 15, 1965. NASA Technical Memorandum X-1123, 1965.
32. Berg, O.E. and Meredith, L.H. Meteorite Impacts to an Altitude of 103 Kilometers. J. Geophys. Res., Vol.61, 1956, pp.751-754.
33. Loc. cit. (30), (31).
34. Loc. cit. (30), (31).
35. Loc. cit. (30), (31).
36. Naumann, R.J. Pegasus Satellite Measurement of Meteoroid Penetration. (Feb 16 - July 20, 1965). NASA Technical Memorandum X-1192, 1965.
37. Hemenway, C.L. and Soberman, R.K. Studies of Micrometeorites Obtained From a Recoverable Sounding Rocket. Astron. J. Vol.67, No.5, pp.256-266, 1962.
38. Hemenway, C.L., Soberman, R.K. and Witt, G. Particle Sampling from Noctilucent Clouds. Nature, Vol.199, No. 4890, 1963, pp.269-270.
39. Dubin, M. and McCracken, C.W. Measurements of Distribution of Interplanetary Dust. Astron. J. Vol. 67, No.5, pp.248-256, 1962.
40. Alexander, W.M., McCracken, C.W., Secretan, L. and Berg, O.E. Rocket, Satellite and Space-Probe Measurements of Interplanetary Dust. Trans. Am. Geophys. Union, Vol.43, 1962, pp.351-360.
41. Alexander, W.M. Interplanetary Dust. Trans. Am. Geophys. Union, Vol.44, 1963, pp.464-469.
42. Loc. cit. (12).

43. Wlochowics, R. Detecting Micrometeoroids Acoustically From Rockets. Can. J. Phys., Vol.44, No.1, 1966, pp.1-25.
44. Loc. cit. (39).
45. Alexander, W.M. The Mission of Mariner II: Preliminary Observations. Cosmic Dust. Science, Vol.138, 1962, pp.1098-1099.
46. Loc. cit. (43).
47. Curtis, J.S. An Accelerated Reservoir Light Gas Gun. NASA Technical Note D-1144, 1962.
48. Humes, D.H. Influence of the Bumper and Main Wall Material on the Effectiveness of Single Meteoroid Bumpers. NASA Technical Note D-3104, 1965.
49. Shelton, H., Hendricks, C.D. Jr. and Wuerker, R.F. Electrostatic Acceleration of Microparticles to Hypervelocities. J. App. Phys., Vol.31, No.7, pp.1243-1246, 1960.
50. Friichtenicht, J.F. Two-Million-Volt Electrostatic Accelerator for Hypervelocity Research. Rev. Sci. Inst., Vol.33, No.2, pp.209-212, 1962.
51. Vedder, J.F. Charging and Acceleration of Microparticles. Rev. Sci. Inst., Vol.34, No.11, pp.1175-1183, 1963.
52. Hamermesh, B. and Becker, D.G. The Drooping Square Wave Linear Accelerator For Artificial Micrometeoroids. TRW Space Technology Laboratories, Thompson Ramo Wooldridge Inc. Redondo Beach, California.
53. Dingman, E.H. A Hypervelocity Microparticle Linear Accelerator for Use in Micrometeoritic Simulation. IEEE Trans. Nuc. Sci. Vol.12, No.3, pp.544-549, 1965.
54. Smythe, W.R. Static and Dynamic Electricity. Sec. 2.16. McGraw-Hill Book Co., Inc. New York and London (1939).
55. Loc. cit. (54) Sec. 5.081.
56. Loc. cit. (49).
57. Jolley, L.B.W. Summation of Series. Series No. 1133. Second Revised Edition. Dover Publications, Inc. New York (1961).
58. Loc. cit. (57) Series No. 336.
59. Loc. cit. (57) Series No. 71.

60. Loc. cit. (54) Sec. 5.081.
61. Loc. cit. (57) Series No. 308.
62. Müller, E.W. Field Desorption. Phys. Rev. Vol. 102, No.3, pp.618-624, 1956.
63. Müller, E.W. Direct Observation of Crystal Imperfections by Field Ion Microscopy. pp.77-99 in Direct Observation of Imperfections in Crystals. Edited by J.B. Newkirk and J.H. Wernick. Interscience Publishers. New York, London (1962).
64. Loc. cit. (51).
65. Shelton, H. and Wuerker, R.F. Final Technical Report on Artificial Meteor Studies. Part I. Research Laboratory of Thompson Ramo Wooldridge Inc., Canoga Park, California, U.S.A.
66. Loc. cit. (49).
67. Cho, A.Y.H. Contact Charging of Micron-Sized Particles in Intense Electric Fields. J. App. Phys. Vol.35, No.9, 1964, pp.2561-2564.
68. Heywood, D.R. A Survey of Low Noise Nucleonic Amplifiers. M.A.Sc. Thesis, Department of Electrical Engineering, University of British Columbia, 1963.
69. Heywood, D.R. and White, B.L. Low Noise Nucleonic Preamplifier. Rev. Sci. Inst. Vol.34, No.9, pp.1050-1051, 1963.
70. Van de Hulst, H.C. Light Scattering by Small Particles. John Wiley and Sons, Inc., New York (1957), p.34.
71. Stratton, J.A. Electromagnetic Theory. McGraw-Hill Book Co., Inc. New York and London (1941), p.563, Sec.9.25.
72. Loc. cit. (70) p.114, Chapter 9.
73. Loc. cit. (70) p.163.
74. Loc. cit. (70) pp.280-281.
75. Loc. cit. (70) pp.203-207, 223 and 279.
76. Loc. cit. (70) p.280.
77. Loc. cit. (70) p.273.
78. Loc. cit. (70) p.276.

79. Loc. cit. (52).

80. Becker, D.G. A Linear Accelerator For Micrometeoroids - Analysis.
Space Technology Laboratories Inc., Redondo Beach,
California, (1962).

B29861